GUI DRIVEN SIGMA-DELTA MODULATOR DESIGN AND MEASUREMENT TOOL WITH A VIEW OF MEDICAL ULTRASOUND IMAGING IMPLEMENTATION

by

Güneş Damla Altınok

BS, Electronics Engineering, Isik University, 2006

Submitted to the Institute of Biomedical Engineering
in partial fulfillment of the requirements
for the degree of
Master of Science
in
Biomedical Engineering

Boğaziçi University
June 2009

ACKNOWLEDGMENTS

I would highly like to thank Professor Mehmed Özkan for making this Master's Thesis available as my supervisor and for providing comments and useful suggestions on this study.

I would also like to thank Dr Mohammed Al-Janabi for his invaluable guidance and help on issues related to the simulation and analysis of sigma-delta modulators. I am grateful to him for sharing his experiences and for his support as my co-advisor throughout my MSc study.

I would particularly like to acknowledge Professor Izzet Kale for the opportunity I have had to work in his research laboratory throughout this project and for his advice on my MSc study with his detailed knowledge and experiences about sigma-delta modulators.

I would like to express my gratitude to Professor Mustafa Karaman for providing the real ultrasound wire phantom data set, his suggestions on my study and for his invaluable instructive comments.

I am also grateful to TUBITAK-BIDEB for the graduate scholarship I have had throughout my MSc study.

I am especially indebted to my parents Muammer Altınok, Nurten Altınok, and my sister Başak Altınok, and my friend Ufuk Mat for their love and support and help during my study.

ABSTRACT

GUI DRIVEN SIGMA-DELTA MODULATOR DESIGN AND MEASUREMENT TOOL WITH A VIEW OF MEDICAL ULTRASOUND IMAGING IMPLEMENTATION

The widespread use of mixed-signal based systems in conjunction with the various benefits provided by digital techniques have significantly increased the need for high resolution analog-to-digital (A/D) and digital-to-analog (D/A) converters. The (A/D) converter based on the sigma-delta modulation $\Sigma - \Delta$ is capable of providing a very high resolution for low-to-medium signal bandwidth applications. It utilizes oversampling and noise-shaping to trade-off operation speed for amplitude resolution.

In this study the theory and advantages of sigma-delta converters are introduced. Low-pass and narrow-band band-pass $\Sigma - \Delta$ modulators are designed, examined and analyzed. A variety of $\Sigma - \Delta$ converter topologies are modeled in Simulink and MATLAB routines are written. Various Butterworth and inverse Chebyshev based $(\Sigma - \Delta)$ modulators are designed and implemented at the behavioral-level to enhance SNRs. The system performance analysis and tradeoffs are analyzed via various single-loop and multi-stage low-pass and resonator-based band-pass sigma-delta modulator simulations. A user-friendly software tool is developed to speed up the design, analysis, evaluation and measurement of single-loop and multistage $\Sigma - \Delta$ modulators at the system-level. Using second-order low-pass $\Sigma - \Delta$ modulator built in the design tool is used in the medical ultrasound beamforming implementation. For this aim, a comparison of ultrasound images constructed by beamformer architectures that use 10-bit ADC's and single-bit $\Sigma - \Delta$ modulators are performed. The benefits and trade-offs of using 1-bit $\Sigma - \Delta$ modulators are examined.

Keywords: Sigma-delta modulator, A/D converter, low-pass and band-pass $\Sigma - \Delta$ modulators design tool.

ÖZET

MEDİKAL ULTRASON GÖRÜNTÜLEME UYGULAMASI AMACIYLA GUI İLE YÜRÜTÜLEN SIGMA-DELTA MODÜLATÖR TASARIM VE ÖLÇÜM ARACI

Karma işaret tabanlı sistemlerin yaygın kullanılması, dijital teknolojinin sağladığı yararlarla birleşince, analog-dijital ve dijital-analog yüksek çözünürlü çeviricilere olan ihtiyaç dikkati çeker bir şekilde artmıştır. Sigma-delta modülasyon ($\Sigma - \Delta$) tabanlı analog-dijital çeviriciler düşük-orta sinyal bant genişliği uygulamaları için çok yüksek çözünürlük sağlama kapasitesine sahiptirler. Bu çeviriciler yüksek hızda örnekleme ve gürültü ayarlama tekniklerini kullanarak genlik çözünürlüğünü arttırırlar.

Bu çalışmada $\Sigma - \Delta$ modülatörlerin kuramı ve avantajları sunulmaktadır. Bu doğrultuda, alçak ve dar bantlı bant-geçiren çeviriciler tasarlandı, incelendi ve analiz edildi. $\Sigma - \Delta$ modülatör topolojileri Simulink kullanılarak modellendi ve MATLAB tabanında yönlendirme kodları yazılarak farklı uygulamaları yapıldı. Çeşitli Butterworth ve Ters Chehebyshev tabanlı $\Sigma - \Delta$ modülatörler, sinyal-gürültü oranını (SNR) arttırmak için davranışsal düzeyde tasarlandı ve gerçekleştirildi. Sistemin performans analizleri ve zorlukları çeşitli tek döngülü ve çok döngülü alçak-geçiren ve rezonans tabanlı bant-geçiren sigma-delta modülatör simulasyonlarıyla analiz edildi. Sistem düzeyinde tek döngülü ve çok döngülü $\Sigma - \Delta$ modülatörlerin tasarımını ve değerlendirmesini çabuklaştırmak için bir tasarım aracı geliştirildi. Medikal ultason demetleme uygulaması olarak tasarım aracında geliştirilmiş ikinci derece alçak geçiren $\Sigma - \Delta$ modülatör kullanıldı. Bu amaçla, 10-bit analog-dijital çevirici ile elde edilmiş imaj ile tek-bitlik $\Sigma - \Delta$ modulator ile elde edilmiş imajlar karşılaştırıldı. 1-bitlik $\Sigma - \Delta$ modulator kullanmanın avantajları ve zorlukları verildi.

Anahtar Sözcükler: Delta-sigma modülatör, analog-digital çevrici, alçak ve dar bantlı bant-geçiren modülasyon, tasarım aracı.

TABLE OF CONTENTS

ACKNOWLEDGMENTS iii
ABSTRACT iv
ÖZET v
LIST OF FIGURES viii
LIST OF TABLES xii
LIST OF SYMBOLS xiii
LIST OF ABBREVIATIONS xv
1. INTRODUCTION 1
2. NYQUIST RATE A/D CONVERTERS 4
2.1 Sampling 4
2.2 Quantizing 6
2.2.1 Quantization Error 7
2.3 Performance Definitions 8
3. PRINCIPLES OF SIGMA-DELTA A/D CONVERTERS 10
3.1 Oversampling 10
3.2 Noise-Shaping 12
4. LOW-PASS SIGMA-DELTA MODULATORS 16
4.1 First Order Sigma-Delta Modulators 17
4.2 Second Order Sigma-Delta Modulators 20
4.3 Tonality 23
5. HIGH-ORDER SIGMA-DELTA MODULATORS 25
5.1 Single Loop Structure 25
5.2 Multi-stage (Cascaded) Sigma-Delta Modulators 28
5.3 Butterworth High-Pass Response 33
5.4 Inverse Chebyshev Complex Response 33
5.5 Loop Filter Topologies 34
5.5.1 Weighted Feedforward Summation 35
5.5.2 Feedforward summation with Local Feedbacks 36
6. BAND-PASS SIGMA-DELTA MODULATORS 39

6.1 Band-Pass $\Sigma - \Delta$ Modulator Loop-Filter Design 40
6.2 Loop-Filter Topologies 43
6.2.1 Chain of Resonators with Weighted Feedforward Summation . . 44
6.2.2 Chain of Accumulators with Feedforward Summation and Local Feedbacks 46
7. A DESIGN, EVALUATION AND MEASUREMENT TOOL FOR $\Sigma-\Delta$ MODULATORS 49
7.1 The Graphical User Interface 49
7.1.1 Input Parameters 50
7.1.2 Modulator Specifications 50
7.1.3 Display of Results 51
7.2 The Graphical User Interface in Operation 52
7.2.1 Step-by-Step Example-1 (Low-Pass Case) 52
7.2.2 Step-by-Step Example-2 (Band-Pass Case) 56
8. ULTRASOUND BEAMFORMING IMPLEMENTATION 62
8.1 Background: Basic Principles of Medical Ultrasound Imaging 62
8.2 Front-end Components of the Digital Ultrasound System 63
8.3 Beamforming 64
8.3.1 The Transmitter and Transmitted Beam Focusing 64
8.3.2 The Receiver and Beam Forming 66
8.4 Digital Phased Array Beamforming Implementation 69
8.4.1 Experimental Data-set 69
8.4.2 Beamforming Using Conventional Multi-bit A/D Converters . . 72
8.4.3 Beamforming Using Single-Bit $\Sigma - \Delta$ A/D Converters 78
8.4.4 Simulation Results and Discussion 82
9. CONCLUSION 87
APPENDIX A. LOOP FILTER TOPOLOGIES 90
A.1 Weighted Feedforward Structure 90
A.2 Weighted Feedforward Summation with Local Feedbacks 91
REFERENCES 92

LIST OF FIGURES

Figure 2.1	Conventional analogue-to-digital conversion process.	4
Figure 2.2	Nyquist rate sampling ($f_s > 2f_b$) with an anti-aliasing filter response.	5
Figure 2.3	Quantizer with quantizing level $Q = 5$.	6
Figure 2.4	Quantizer errors as additive noise model.	7
Figure 3.1	Power of the quantization noise for Nyquist-rate and oversampled modulators.	11
Figure 3.2	Block diagram of the $\Sigma - \Delta$ modulator.	13
Figure 3.3	Linearized model of the $\Sigma - \Delta$ modulator block diagram.	14
Figure 3.4	Power spectrum of quantized signal.	15
Figure 4.1	Block diagram of a first order $\Sigma - \Delta$ modulator.	16
Figure 4.2	The linearized model of the first order $\Sigma - \Delta$ modulator.	17
Figure 4.3	Output spectrum of a first order $\Sigma - \Delta$ modulator for a 0.5 input sine wave amplitude.	20
Figure 4.4	Block diagram of a second order $\Sigma - \Delta$ modulator.	21
Figure 4.5	Output spectrum of a second order $\Sigma - \Delta$ modulator.	22
Figure 4.6	In-band SNR vs amplitude of input sinusoid for first order and second order $\Sigma - \Delta$ modulators.	23
Figure 4.7	Block diagram of a first order $\Sigma - \Delta$ modulator structure with dither.	24
Figure 5.1	Block diagram of a N^{th} order $\Sigma - \Delta$ modulator.	25
Figure 5.2	The magnitude spectra of NTFs of $\Sigma - \Delta$ modulators.	26
Figure 5.3	The NTF's of the (a) 1^{st}, (b) 2^{nd}, (c) 3^{rd} order $\Sigma - \Delta$ modulators.	27
Figure 5.4	Block diagram of a cascaded $\Sigma - \Delta$ modulator.	29
Figure 5.5	1-1-1 cascade: a 3^{rd} order $\Sigma - \Delta$ modulator by cascading three 1^{st} order $\Sigma - \Delta$ modulators.	31
Figure 5.6	3^{rd} order $\Sigma - \Delta$ modulator using the structure of (a) single loop, (b) MASH structure.	33

Figure 5.7	The comparison of the frequency responses of the $H(z)$ after modification.	34
Figure 5.8	Chain of accumulators with weighted feedforward summation.	35
Figure 5.9	5^{th} order $\Sigma-\Delta$ modulator using the chain of accumulators structure with local feedbacks.	36
Figure 5.10	NTF's of a third order $\Sigma-\Delta$ modulator using the chain of integrators (a) weighted feedforward summation, (b) weighted feedforward summation and local feedbacks.	38
Figure 6.1	(a) Block diagram of a BP $\Sigma-\Delta$ modulator (b) Typical NTF and STF.	40
Figure 6.2	A 4^{th}-order band-pass $\Sigma-\Delta$ modulator obtained with $z^{-1} \rightarrow -z^{-2}$ transformation.	41
Figure 6.3	The pole-zero alignments of the NTFs for (a)LP (b)BP $\Sigma-\Delta$ modulators.	42
Figure 6.4	The NTF of a 4th-order $\Sigma-\Delta$ modulator with resonant frequency $\nu = 0.25$.	43
Figure 6.5	Output spectrum of a 4^{th} order BP $\Sigma-\Delta$ modulator with resonance frequency of $\nu = 0.125$.	44
Figure 6.6	Loop-filter topology for a 4^{th} order BP $\Sigma-\Delta$ modulator using cascaded integrators with feedforward coefficients.	45
Figure 6.7	The output power spectrum of a 4th order BP $\Sigma-\Delta$ modulator employing weighted feedforward summation structure.	46
Figure 6.8	4^{th} order BP $\Sigma-\Delta$ modulator designed with the topology of chain of accumulators with feedforward summation and local feedbacks.	47
Figure 6.9	The output power spectrum for the 4^{th} order BP $\Sigma-\Delta$ modulator employing weighted feedforward summation with local feedbacks architecture.	48
Figure 7.1	Screenshot of the GUI consisting of the options for the LP or BP $\Sigma-\Delta$ modulators.	50
Figure 7.2	The second part of the GUI to specify the input parameters.	53
Figure 7.3	The second part of the GUI to specify the structure type and the order of the modulator.	54

Figure 7.4	A 3^{rd} order LP $\Sigma-\Delta$ modulator using cascaded (MASH) structure.	55
Figure 7.5	Zoomed simulation results displayed in the GUI.	56
Figure 7.6	Screenshot of the GUI consisting of the input parameters and simulation results for the 6^{th} order BP $\Sigma-\Delta$ modulator.	57
Figure 7.7	A 6^{th} order BP $\Sigma-\Delta$ modulator using chain of accumulators with weighted feedforward summation.	58
Figure 7.8	A 6^{th} order BP $\Sigma-\Delta$ modulator (with normalized frequency of 0.125) simulation results displayed in GUI.	59
Figure 7.9	A 6^{th} order BP $\Sigma-\Delta$ modulator (with a normalized frequency of 0.3) simulation results displayed in GUI.	60
Figure 8.1	Simplified block diagram of the front-end hardware of the ultrasound system.	63
Figure 8.2	Transmit mode array systems.	65
Figure 8.3	Focal point geometry in polar coordinates.	65
Figure 8.4	Receive mode array system.	67
Figure 8.5	(a) Steering (b) Steering and focusing.	67
Figure 8.6	Schematic diagram of ultrasound scanning format.	68
Figure 8.7	Schematic experimental setup.	70
Figure 8.8	Cross-section field of 6-wire phantom.	70
Figure 8.9	RF signal of 2048 samples from 3.5 MHz transducer insonifying wire phantom.	72
Figure 8.10	Frequency spectrum of the RF echo signal sampled at the Nyquist-rate.	73
Figure 8.11	Sampling rate is increased to 16 times the Nyquist rate.	73
Figure 8.12	Frequency spectrum of the signal after interpolation filter.	74
Figure 8.13	Wave-field of the 1^{st} receivers data obtained from all 128 transmit elements.	75
Figure 8.14	Signal received by the 64^{th} element transmitted by 1^{st} element, original signal and delayed signal.	76
Figure 8.15	Echo signals of the 1^{st}, 64^{th} and 128^{th} receive elements after transmit-delays.	77

Figure 8.16	First two: 1^{st} and 64^{th} receive elements unfocused, third: total echo signals after transmit focusing.	78
Figure 8.17	Image in polar coordinates ($r - sintheta$).	79
Figure 8.18	Block diagram of a 2^{nd} order low-pass $\Sigma - \Delta$ modulator.	80
Figure 8.19	Frequency spectrum of the signal modulated with 2^{nd} order low-pass $\Sigma - \Delta$ modulator.	81
Figure 8.20	Image in polar coordinates before decimation process ($r-sintheta$).	82
Figure 8.21	Image in polar coordinates ($r - sintheta$).	83
Figure 8.22	(a) 10-bit A/D beamformer (b) 1-bit $\Sigma - \Delta$ beamformer.	85

LIST OF TABLES

Table 8.1 Simulation parameters. 71

LIST OF SYMBOLS

Δ	quantization step
$\Sigma - \Delta$	sigma-delta
Σ-Δ-M	delta-sigma modulator
ϵ	error term
ω	angular frequency
ν	normalized frequency
σ_e^2	variance of the error
σ_x^2	variance of the signal
A	signal amplitude
a	feedforward coefficient
Amax	maximum signal amplitude
B	internal resolution, number of bits, value of feedback bit
b	feedback coefficient
d[n]	dither signal in discrete time-domain
e[n]	quantization noise term in discrete time-domain
E	quantization noise term in z-domain
f_0	resonance frequency, centre frequency
f_B	desired signal band
f_N	Nyquist frequency
f_b	signal frequency
f_s	sampling frequency
g	gain of resonator
h[n]	transfer function of integrator in time-domain
H(z)	transfer function of integrator in z-domain
L(z)	transfer function of the loop-filter in z-domain
P(f)	power spectral density
T_s	sampling period
Q	quantizing level

V_{off}	offset voltage
V_{ref}	reference voltage
x(t)	continuous-time input signal
x[n]	discrete-time input signal
X(z)	input signal in z-domain
X_m	full-scale level of the A/D converter
y(t)	continuous-time output signal
y[n]	discrete-time output signal
Y(z)	output signal in z-domain

LIST OF ABBREVIATIONS

A/D	Analogue-to-Digital
ADC	Analogue-to-Digital Converter
BP	Band-pass
DAC	Digital-to-Analog Converter
DR	Dynamic Range
DSP	Digital Signal Processing
DT	Discrete-Time
FIR	Finite Impulse Response
GNSS	Global Navigation Satellite System
GUI	Graphical User Interface
IC	Integrated Circuit
IF	Intermediate Frequency
IIR	Infinite Impulse Response
LP	Low-pass
MASH	Multi-Stage Noise-Shaping
NTF	Noise Transfer Function
OSR	Oversampling Ratio
PSD	Power Spectral Density
RF	Radio Frequency
S/H	Sample-and-Hold
SC	Switched-Capacitor
SNR	Signal-to-Noise Ratio
SNDR	Signal-to-(Noise+Distortion) Ratio
STF	Signal Transfer Function
VDSL	Very high bit-rate digital subscriber line

1. INTRODUCTION

The signals in the real world are analogue in nature. However, for the efficient transmission, storage data and processing of signals, it is preferable to convert analogue signals into digital signals using an Analogue-to-Digital (A/D) converter. As a result of its many advantages, digital signal processing has been applied in practical systems covering a broad range of disciplines. Signal processing in the digital domain is also desirable in such areas as biomedical applications especially in ultrasound imaging [1, 2], providing the needed accuracy for biomedical imaging [3]. There are two main steps in A/D conversion: sampling and quantizing. Thus digital implementation has its own limitations. Two practical limitations are the speed of A/D converters, in other words how fast the converter discriminates the signal in time and the quantization error which describes how accurate the converter discriminates the signal in amplitude. To overcome the limitations, one modulation technique, $\Sigma - \Delta$ modulation technique has been widely used to convert analogue signals to their digital equivalents because they are capable of providing high resolution [4, 5]. Even though the concepts of $\Sigma - \Delta$ modulation were first presented in the middle of the last century, they were not widely used until the last two decades due to improvements in silicon technology. As a result of recent developments in digital VLSI technologies, there exist various low-pass (LP) $\Sigma - \Delta$ architectures which have been used in applications such as instrumentation, voice band data telecommunications high-fidelity audio and speech, metering applications, data-acquisition [4, 5, 6]. Also there are typical applications of band-pass (BP) $\Sigma - \Delta$ data converters such as digital radio systems, [7, 8], receivers for digital mobile cellular telephony [9], high-speed modems [10], satellite communication services [11], in phased-array ultrasound imaging [2], and GNSS front-end applications [12]. In addition, other applications for $\Sigma - \Delta$ modulation are in sensor systems to shape out the noise from the sensor itself and its environment [13]. $\Sigma - \Delta$ modulators use oversampling and noise-shaping to achieve high resolution. Oversampling reduces the amount of quantization noise power present in the signal band and noise-shaping further attenuates the quantization noise in the signal band, thereby pushing most of

the noise power to out-of-band frequencies [14]. The high frequency quantization noise can be removed without affecting the signal itself by using a digital low-pass filter operating on the output of the sigma-delta modulator [15]. Therefore; ultra-low power $\Sigma - \Delta$ modulators for are widely used in biomedical applications such as: electrocardiography (ECG), electroencephalography (EEG), Electrooculography (EOG) . On the other hand, the non-linear quantizer in combination with the feedback loop employed by the $\Sigma - \Delta$ modulators, cause significant stability and tonality problems. This is especially true for single-loop $\Sigma - \Delta$ modulators whose orders are higher than two [14]. To overcome instability, various single-loop or multi-stage $\Sigma - \Delta$ modulator topologies can be developed. Since there is not a unique methodology to guarantee the stability and proper operation of high-order $\Sigma - \Delta$ modulators, the various design procedures can be used based on performance analysis. Thus, several design automation tools for LP, and BP $\Sigma - \Delta$ modulators at the system level were reported in the literature [14, 16, 17]. The most common approach to automate the design procedure is based on iterative performance optimization via a performance evaluation loop using statistical methods or behavioral simulations for the desired modulator parameters [16, 18, 19]. The other common approach is the automation of the modulator coefficients by optimizing the Noise Transfer Functions (NTF) or Signal Transfer Functions (STF) for the desired design specifications. Inverse Chebyshev or Butterworth filters are used for the NTF designs in order to obtain acceptable quantization noise reduction in the signal band [14, 17, 20]. In this study, a user-friendly software tool to speed up the design, analysis, and evaluation of LP and BP single-loop and multi-stage $\Sigma - \Delta$ modulators applicable in many biomedical applications at the system-level is presented. This tool gives designers the ability to use easy-to-implement $\Sigma - \Delta$ modulator topologies and view their corresponding simulation results including the power spectral densities of the modulator output and quantizer input signals as well as their SNR values. The MATLAB routines embedded in the Graphical User Interface (GUI) simulate the desired topologies according to the input parameters defined by the user.

In contrast to many $\Sigma - \Delta$ design tools in the literature, which mostly employ specific design structures; this tool enables the user to design and analyze a variety of LP and BP based $\Sigma - \Delta$ modulator topologies such as the single-loop, multi-stage

(MASH), chain of accumulators with weighted feedforward summation and chain of accumulators with feedforward summation with local resonator feedbacks. Moreover, the tool allows the user to design the NTFs of Butterworth and Inverse Chebyshev filters based on input specifications such as the cut-off frequency, bandwidth and modulator order. At this point, the thesis is organized as follows: Chapter-2 describes conventional A/D conversion with a conventional Nyquist sampling rate. This is followed in the Chapter-3 by the basic principles of $\Sigma - \Delta$ converters and how they combine the advantages of oversampling techniques with the noise-shaping concepts. The $\Sigma - \Delta$ data converters are discussed and contrasted with the Nyquist-rate converters. Low-order $\Sigma - \Delta$ modulators and high-order LP $\Sigma - \Delta$ modulators are designed, examined and analyzed, in Chapters 4 and 5 respectively. Next, in Chapter-6 $\Sigma - \Delta$ converter architectures for narrow-band BP signals are described. Various single-loop and multi-stage LP and BP $\Sigma - \Delta$ modulator analysis and simulations are introduced. The noise transfer functions of these designs have involved the use of differencers, Butterworth and inverse Chebyshev filters. The system performance analysis and tradeoffs are introduced in Chapter-7. This chapter involves developing SNR routines to assess the performance of these $\Sigma - \Delta$ modulators. This work will form the foundation for the proposed design methodology, which details the design tool created in the MATLAB that will speed up the design, analysis, and evaluation of single-loop and multi-stage $\Sigma - \Delta$ modulators at the system-level. The proposed tool will allow researchers and practitioners to design and verify the feasibility of the $\Sigma - \Delta$ modulator at a much earlier stage of the design process thus saving considerable time, effort and cost. It can be also used as a valuable teaching tool for advanced courses on data converters. Finally, in Chapter-8 an ultrasound imaging application of a second order low-pass $\Sigma - \Delta$ modulator is performed. Using the desired $\Sigma - \Delta$ modulator built in the design tool is used in the medical ultrasound beamforming architecture. A comparison of ultrasound images constructed by 10-bit ADC beamformer and single-bit $\Sigma - \Delta$ modulators is detailed. Besides the advantages of reduced size, cost and power consumption, the artifacts in the images constructed using 1-bit $\Sigma - \Delta$ modulators are examined.

2. NYQUIST RATE A/D CONVERTERS

Signals in the real world are continuous in time and amplitude. In order to process these analogue signals using digital systems, they should be converted into the digital domain using A/D converters, i.e. the signals have to be sampled in time and quantized to discrete amplitudes. The conventional A/D conversion processes involves converting an analogue input signal $x(t)$ into a sequence of digital codes $x[n]$ [21], as shown in Figure 2.1.

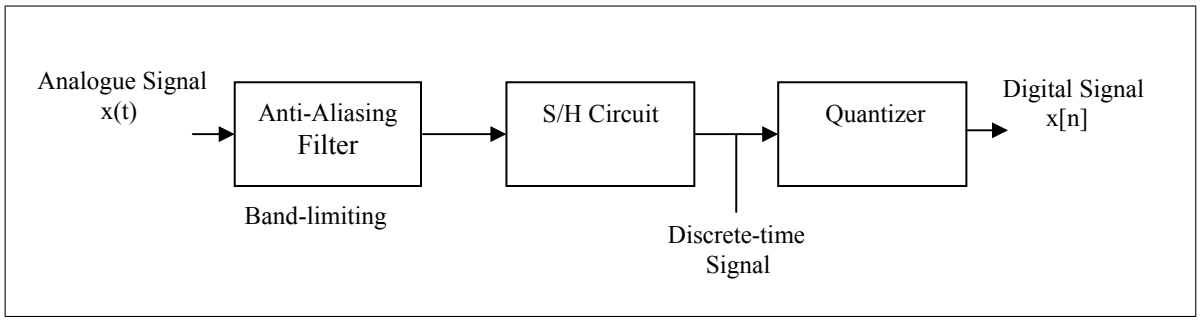

Figure 2.1 Conventional analogue-to-digital conversion process.

First, an anti-aliasing filter is used, which is an analogue LP filter, to limit the bandwidth of the input signal $x(t)$ in order to eliminate distortion. Second, the filter output is sampled with a sample and hold (S/H) circuit at a sampling rate $f_s = 1/T_s$, where T_s denotes the sampling period. As a result of this process, a discrete-time signal is produced. Next, the amplitude of this sampled signal is quantized and encoded by an appropriate quantizer, so that a discrete-amplitude signal $x[n]$ is generated.

2.1 Sampling

A sampler converts a continuous-time signal into a discrete-time signal obtained by taking samples of the continuous-time signal at discrete time instants [21]. Ideally,

a sampler yields a sequence of delta functions whose amplitude equals the signal at the sampling times. For a uniform sampling with an interval of T_s, the output of a sampler is given by [22]:

$$\sum_{n=-\infty}^{\infty} x(t)\delta(t - nT). \tag{2.1}$$

According to the Nyquist sampling theorem [21]; if the sampling frequency $f_s = 1/T_s$ is greater than the twice the highest input signal frequency f_b, then the input signal can be fully recovered from the output samples, where f_s is denoted for Nyquist frequency. As seen in Figure 2.2, in the frequency domain, the sampled signal is the repeated version of the original signal spectrum at integer multiples of the sampling frequency f_s. As a result, the spectrum is periodic with period T_s [22].

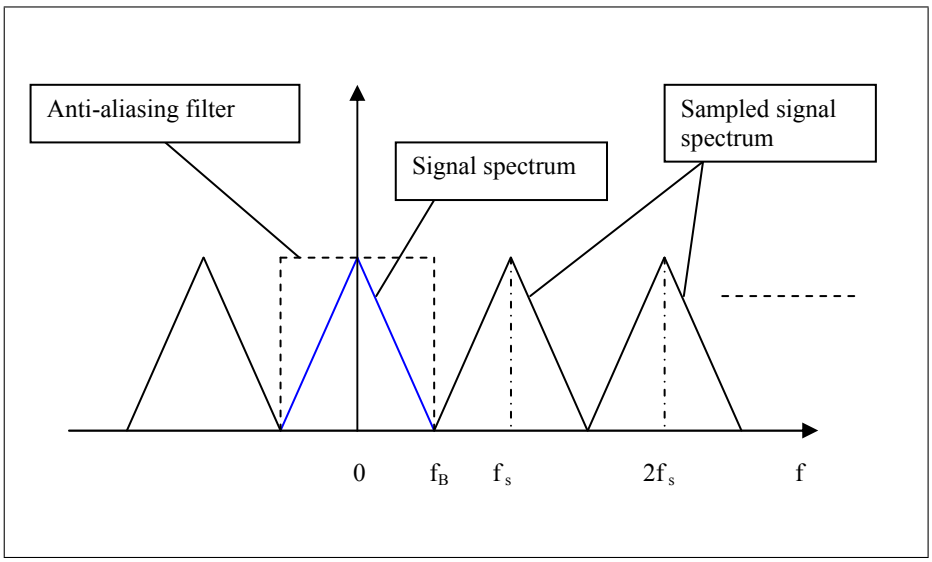

Figure 2.2 Nyquist rate sampling ($f_s > 2f_b$) with an anti-aliasing filter response.

If the sampling frequency is less than twice the signal bandwidth, the repeated versions of the signal will partially overlap and alter the signal spectrum so that the spectrum cannot be properly reconstructed. This non-linear signal distortion is called aliasing [22]. To overcome the aliasing phenomenon, pre-filtering the input signal is used. This LP filter is called the anti-aliasing filter, which has a flat response over the frequency band of interest as shown in Figure 2.2 and attenuates the frequencies above the signal-band [23]. In other words, the frequency response of the filter passes the

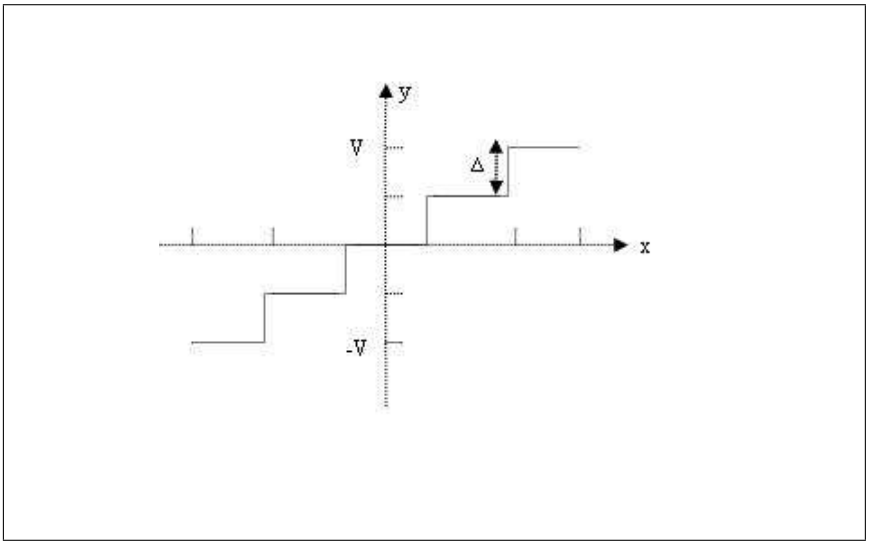

Figure 2.3 Quantizer with quantizing level $Q = 5$.

signal in the signal-band-region and rejects the out-of-band components. As a result, the input signal is forced to be band-limited [21].

2.2 Quantizing

The sampled signal is quantized in amplitude by transforming the sample sequence into a finite set of predefined values. The quantized output amplitudes are rounded to the nearest of this finite set of values, which are usually digitally coded with fixed word length, n. The quantizing levels Q and the digital word length n, i.e. number of bits, can be expressed by the following relationship:

$$Q = 2^n. \tag{2.2}$$

In order to be resolved to different output levels, the step size (Δ of the quantizer would be written as:

$$\Delta = \frac{2V}{Q-1} = \frac{2V}{2^n - 1}. \tag{2.3}$$

The relation described in Eq. 2.3 can be seen in Figure 2.3.

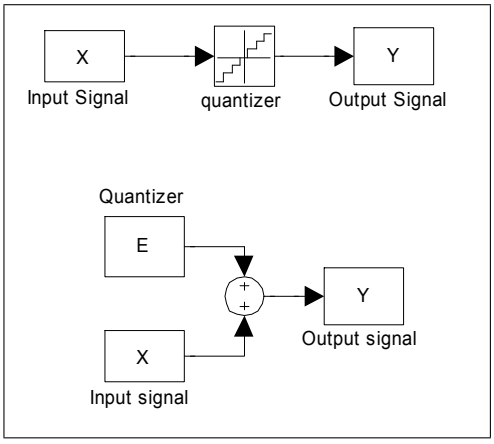

Figure 2.4 Quantizer errors as additive noise model.

2.2.1 Quantization Error

From Figure 2.3, it can be easily seen that the quantized signal is not exactly equal to the actual signal, due to the approximation of the sampled signal to the nearest code word. Therefore the error of the quantizer added to the system can be modeled as shown in Figure 2.4, where the error term $e[n]$ is the difference between the output sequence $y[n]$ and the input sequence $x[n]$:

$$e[n] = y[n] - x[n], \tag{2.4}$$

$e[n]$ is a random quantity in the interval $(-\Delta/2, \Delta/2)$ with equal probability. The quantization error can be considered as an independent additive white noise source [24]. By doing so, the quantization error signal is assumed to be:

- A white random signal,
- Independent of the quantizer input signal,
- Uniformly distributed within the interval $[-\Delta/2, \Delta/2]$.

For zero mean $e[n]$ the noise power can be written as [25];

$$\sigma_e^2 = E[e^2] = \frac{1}{\Delta}\int_{-\Delta/2}^{\Delta/2} e^2 de = \frac{\Delta^2}{12}. \tag{2.5}$$

Consider a n-bit A/D converter with $Q = 2n$ quantization levels, i.e. substitute Δ with $\Delta = 2V/(2^n - 1)$, so that Eq. 2.5 yields;

$$\frac{\Delta^2}{12} = \left(\frac{2V}{2^n - 1}\right)^2 /12 \cong \left(\frac{2V}{2^2}\right) /12. \tag{2.6}$$

2.3 Performance Definitions

As a result of the conversion processes, the original signal is distorted; therefore the major aim of the efficient conversion is to reduce the error caused by the sampling and quantization processes. The performance of the A/D converters is mostly analyzed by several parameters.

1. *Signal-to-noise ratio (SNR)*:

   The SNR is the ratio of the input signal power to the noise power of the converter. It is expressed in decibels [26].

   $$SNR = 10\log_{10}\left(\frac{P_{signal}}{P_{noise}}\right) = 10\log_{10}\left(\frac{\sigma_x^2}{\sigma_e^2}\right). \tag{2.7}$$

   Using Eq. 2.7 for σ_e^2 so that Eq. 2.9 can be rewritten as;

   $$SNR = 10\log_{10}(\sigma_x^2) + 10\log_{10}\left(\frac{12 \cdot 2^{2n}}{2^2 V^2}\right). \tag{2.8}$$

   Then the signal to quantization noise ratio becomes;

   $$SNR = 10\log_{10}\left(\frac{\sigma_x^2}{V^2}\right) + 4.77 + 6.02n \quad (dB). \tag{2.9}$$

   Note that there is an SNR improvement of 6.02 dB for every increment of the extra bit of resolution in the A/D converter.

2. *Resolution*: The resolution is the number of bits, n, that an A/D converter uses to represent its analogue input as digital output.

3. *Dynamic Range (DR)*: The DR is the ratio of the maximum signal amplitude to the noise level, expressed in dB. It is the value of the input signal at which the SNR is 0 dB. Considering the input is sinusoidal, the dynamic range of an A/D converter is expressed as the ratio of the signal power of a sinusoidal input signal to the signal power of a small sinusoidal input that results in a SNR of 0 dB [26] The average power of a sinusoidal signal is $V^2/2$. The SNR of a sinusoid with signal power equal to the noise power; $\sigma_x^2 = \sigma_e^2 = \Delta^2/12$ will be 1 i.e. 0 dB [26]. Thus, the dynamic range can be calculated by combining the definition function with Eq. 2.6:

$$\left(\frac{V^2}{2}/\frac{\Delta^2}{12}\right) \cong \frac{V^2}{2}/\frac{(2V/2^n)^2}{12}, \tag{2.10}$$

where $\Delta = 2V/(2^n - 1)$.

This expression reduces to a dynamic range value given by:

$$DR \quad (dB) = 1.76 + 6.02n \tag{2.11}$$

3. PRINCIPLES OF SIGMA-DELTA A/D CONVERTERS

Different from the Nyquist rate A/D converters, $\Sigma - \Delta$ modulators are based on two major concepts: oversampling and noise-shaping [27].

3.1 Oversampling

Oversampling techniques reduce the specifications of the anti-aliasing filter and also improve the resolution obtained from Nyquist rate converters [26]. This improvement is achieved by oversampling, i.e. sampling the signal considerably larger than the Nyquist sampling rate $f_s > 2f_b$. Since the input signal has equal probability to have any value between the step sizes Δ, the total power of the sampled signal and the total power of the original signal are exactly the same. In oversampling method, the frequency resolution is exchanged for amplitude resolution, so that the area under the power spectrum remains the same [22]. On the other hand; the noise power produced is the same as produced by a Nyquist rate converter, but its frequency distribution is different because of the oversampling ratio, OSR. The quantization noise is designated as white noise [28] with zero mean uniformly distributed between $-f_s/2$ and $f_s/2$, and independent from the input signal, as discussed in Chapter-2. Therefore; the probability density function for the quantization noise is uniform as shown in Figure 3.1.

Figure 3.1 shows the power spectral density, $P_e(f)$, of the quantization noise for Nyquist-rate sampling and oversampling. For Nyquist-rate sampling, all the quantization noise power occurs across the signal bandwidth f_B (un-shaded rectangle). In the oversampling case, the same noise power (shaded rectangle) is spread over a bandwidth f_s which is much greater than the signal bandwidth, f_B. Therefore, a considerably smaller part of this total noise power falls in the signal-band $[-f_B, f_B]$. As a result, the quantization-noise power has been reduced by the factor of the oversampled ratio, OSR, where $OSR = f_s/2f_B$. This OSR defines how much faster the signal is sampled

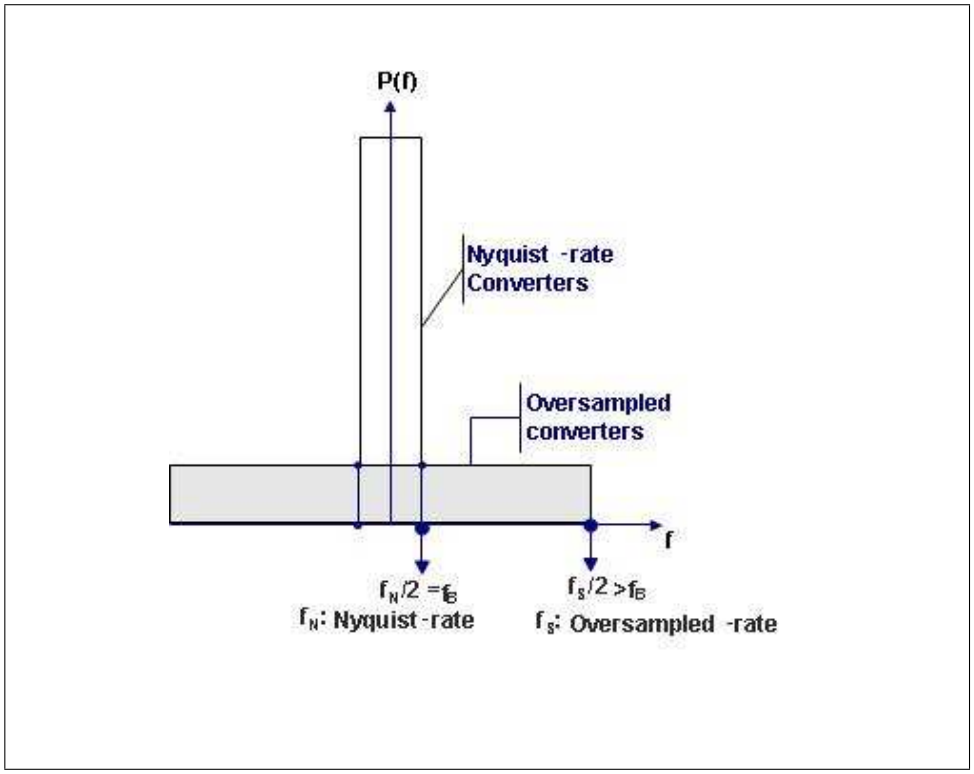

Figure 3.1 Power of the quantization noise for Nyquist-rate and oversampled modulators.

in the oversampled modulator than in a Nyquist-rate converter. The assumed white noise concept states that $P_e(f) = \sigma_e^2/f_s$ [22]. The in-band noise power σ_{ey}^2, at the output of the A/D yields then [26];

$$\sigma_{ey}^2 = \int_{-f_B}^{f_B} P_{ey}(f)\,df = 2\int_0^{f_B} P_{ey}(f)\,df = \int_0^{f_B} \frac{2\sigma_e^2}{f_s}\,df,$$

$$\sigma_{ey}^2 = \sigma_e^2 \underbrace{(2f_B/f_s)}_{OSR}. \tag{3.1}$$

The quantization noise power is $\sigma_e^2 = \Delta^2/12$, where $\Delta^2 = (2V/2^2)^2$ as discussed in Chapter-2. The in-band noise power is reduced by the OSR to;

$$\sigma_{ey}^2 = \frac{V^2}{12\cdot 2^{2n}}\cdot\frac{2f_B}{f_s}, \tag{3.2}$$

where V is the reference voltage and n is the number of bits of the quantizer. As seen from Eq. 3.1, the in-band power σ_{ey}^2 is less than σ_e^2 obtained by the conventional Nyquist rate sampling, as much as the OSR. The $\Sigma-\Delta$ modulator output can then

be low-pass filtered in order to attenuate the out-of-band quantization noise. Since the signal power at the output σ_{xy}^2, remains the same as the input signal power σ_x^2 described in Chapter-2, the SNR improves as much as the additional OSR terms [26]. The SNR in dB is defined as;

$$SNR = 10\log_{10}\left(\frac{\sigma_{xy}^2}{\sigma_{ey}^2}\right),$$

$$SNR = \underbrace{10\log_{10}\frac{\sigma_x^2}{\sigma_e^2}}_{SNR-Nyquist} + 10\log_{10}\underbrace{\frac{f_s}{2f_B}}_{OSR} \quad (dB). \tag{3.3}$$

Note that when $f_s = 2f_B$, which is the case of Nyquist-rate sampling ($OSR = f_s/2f_B = 1$), Eq. 3.3 reduces to the SNR formula for Nyquist-rate converters described in Chapter-2. Compared to an A/D converter sampled at Nyquist rate (Eq. 2.10), the SNR is improved as much as $10\log_{10}(OSR)$, i.e. Every doubling of the OSR values potentially improves the SNR by 3.01 dB. Consequently, the overall SNR value is greatly improved by this oversampling process by spreading the quantization noise power from the signal bandwidth to a larger bandwidth without changing the input signal power.

3.2 Noise-Shaping

The oversampling technique becomes more effective if the noise-shaping concept is also used i.e. the noise spectrum in the signal band is further reduced. As discussed in Section-3.1 the power of the noise spectrum is constant over the entire frequency band. Noise-shaping is a technique which alters this noise spectrum so that it is no longer uniform, but rather, is shaped such that most of the noise power is shifted to higher frequencies. A $\Sigma - \Delta$ modulator consists of a feedforward filter (integrator) and a coarse quantizer (ADC) enclosed in a feedback loop, as shown in Figure 3.2 [29]. $\Sigma - \Delta$ modulators combine sampling rates well above the Nyquist-rate with negative feedback structures. The feedback loop of an oversampling $\Sigma - \Delta$ modulator allows the

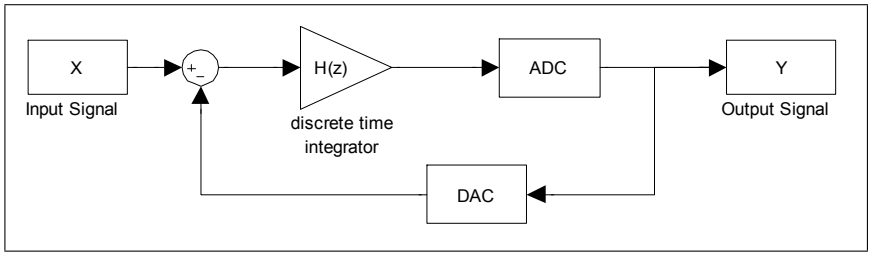

Figure 3.2 Block diagram of the $\Sigma - \Delta$ modulator.

input signal to pass essentially unfiltered through the converter but high-pass filters the quantization noise [26, 27].

The block diagram represents the general operation of noise-shaping by the $\Sigma - \Delta$ modulator. The oversampled input signal filtered through an accumulator, i.e loop-filter $H(z)$. The output is the sum of the output of this discrete time integrator. The digital output is then subtracted as feedback from the input signal so that the noise is shifted to higher frequencies as a result of the introduced delay by this feedback [30]. The quantizer in the feedback loop together with the loop-filter, gives rise to the desired in-band noise suppression and emphasizes the high frequency noise components. Pushing the quantization noise towards high frequencies out of the signal band is referred to as noise-shaping. Since the signal is oversampled, the high frequency noise terms can be removed without affecting the input signal by means of a digital low pass filter at the output [29]. In fact a non-linear system is highly difficult to analyse, therefore a linear model equivalent of the system is used. By the linear model of the system, the quantization noise is assumed to be an additive white noise as discussed in the previous Chapter-2. Consequently, the quantizer is replaced with a noise source $e[n]$, and also the DAC is assumed to be ideal, as shown in Figure 3.3.

The output of a $\Sigma - \Delta$ modulator can be written in the z-domain as follows;

$$Y(z) = X(z)H_x(z) + E(z)H_e(z). \tag{3.4}$$

$Y(z)$, $X(z)$ and $E(z)$ are the output signal, input signal and quantization error in the z-domain, respectively. However, unlike the Nyqusit-rate modulators, for $\Sigma - \Delta$

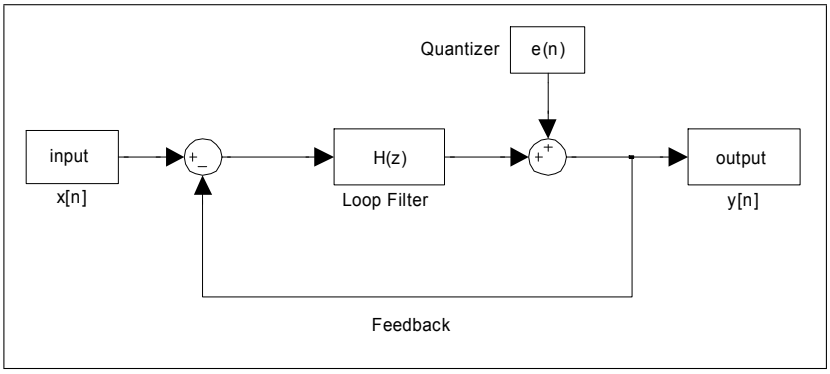

Figure 3.3 Linearized model of the $\Sigma - \Delta$ modulator block diagram.

modulators, $H_x(z)$ is different from $H_e(z)$, where $H_x(z)$ is the Signal Transfer Function (STF) and $H_e(z)$ is the Noise Transfer Function (NTF). As seen in Eq. 3.4 the output of the modulator is the superposition of the input signal filtered by an appropriate STF, and the added noise component shaped by the NTF.

$$H_x = STF = \frac{Y(z)}{X(z)}\bigg|_{E(z)=0} \qquad \text{and} \qquad H_e = NTF = \frac{Y(z)}{E(z)}\bigg|_{X(z)=0}.$$

The general structure of a $\Sigma - \Delta$ modulator is represented in Figure 3.3. The system can be analyzed as follows;

$$[X(z) - Y(z)]H(z) + E(z) = Y(z)$$

$$X(z)H(z) + E(z) = Y(z)[1 + H(z)].$$

So the loop-filter can be expressed in terms of the STF and NTF;

$$Y(z) = X(z)\underbrace{\frac{H(z)}{H(z)+1}}_{STF} + E(z)\underbrace{\frac{1}{H(z)+1}}_{NTF}. \tag{3.5}$$

The STF is designed to be different from the NTF such that the STF usually leaves the signal undisturbed but the NTF shapes the noise to allow a high resolution output [14, 27]. The gain of the STF is close to one in the signal bandwidth and close to zero outside the band. On the other hand, the gain of the NTF is close to zero in the signal band and close to one outside the signal-band.

As seen in Figure 3.4, $\Sigma - \Delta$ modulators use oversampling to reduce the in-band

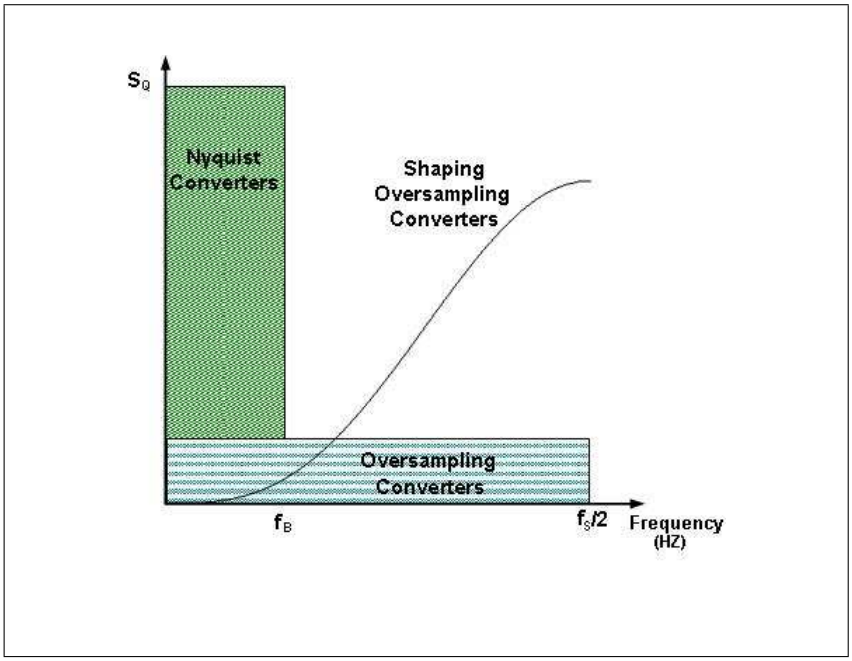

Figure 3.4 Power spectrum of quantized signal.

noise power by spreading a fixed amount of noise power over a bandwidth much larger than the signal bandwidth. To emphasize the result of oversampling, noise-shaping is used to provide further attenuation of the in-band noise by pushing much of the noise components out-of-band.

4. LOW-PASS SIGMA-DELTA MODULATORS

For a LP $\Sigma - \Delta$ data converter the STF should be a low-pass filter and the NTF a high-pass filter in order to satisfy a large attenuation at lower frequencies and amplification at higher frequencies, by leaving the input signal unchanged. The general structure of a $\Sigma - \Delta$ modulator is shown in Figure 4.1. The system consists of a discrete time integrator, usually called feedforward filter, a quantizer (ADC) and D/A converter (DAC) in the feedback loop. The output signal is a bit stream of 1's and 0's. Therefore the output signal $y[n]$ is converted to its predicted analogue value by the DAC before it is subtracted from the input signal $x[n]$. The input of the integrator is the difference between the input signal $x[n]$ and the analogue prediction of the quantized modulator output $y[n]$.

The DAC is considered to operate perfectly, so that it is replaced by a unity gain transfer function [4]. The difference between the input signal $x[n]$ and the analogue conversion of the output signal $y[n]$ gives the quantization error, which is then summed up by the integrator, and quantized again by the quantizer. As the system continues, because of the nature of the 1-bit quantizer, it generates $+1$ and -1. These bit streams can be averaged over many input sample periods to give a very precise result. As a result, a very high SNR can be achieved [30].

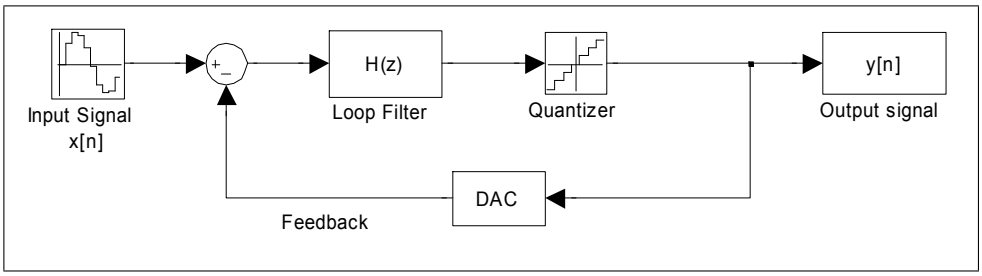

Figure 4.1 Block diagram of a first order $\Sigma - \Delta$ modulator.

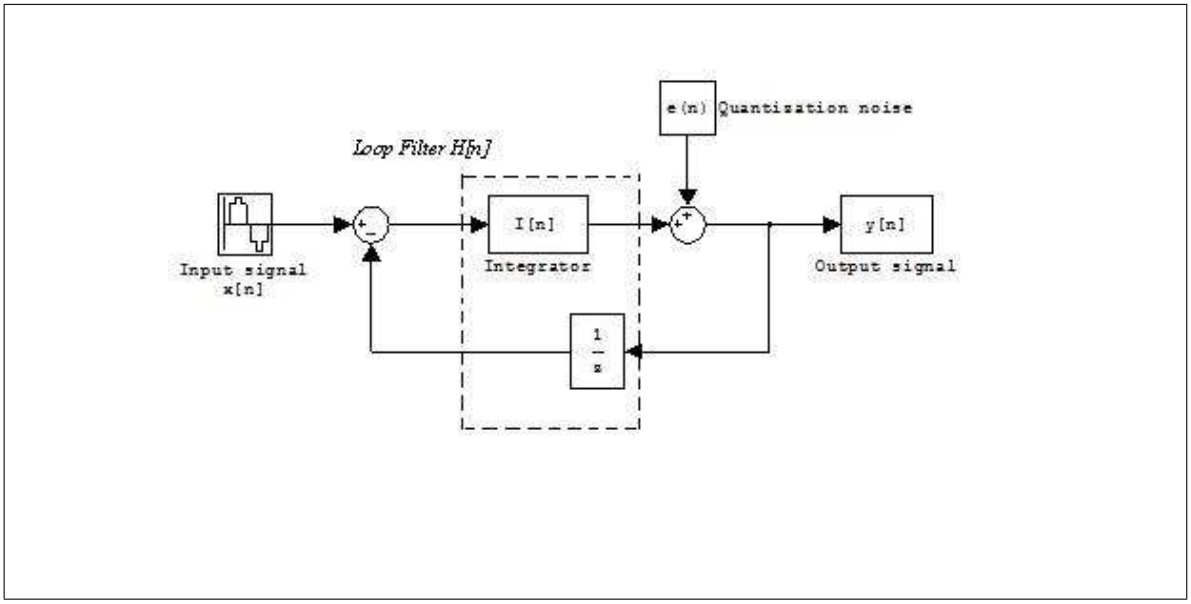

Figure 4.2 The linearized model of the first order $\Sigma - \Delta$ modulator.

4.1 First Order Sigma-Delta Modulators

The number of the integrators used around the loop gives actually the order of the modulator. In the first order $\Sigma - \Delta$ modulator, there is only one accumulator operating, as shown in Figure 4.1. With the linear model of the system, the quantization noise source is assumed to be an additive white noise as discussed in Chapter-3. Consequently, the quantizer is replaced with a noise source $e[n]$, as shown in Figure 4.2 and the DAC is assumed to be ideal. The standard system analysis in the z-domain gives the modulator output $Y(z)$ as follows;

$$Y(z) = [X(z) - Y(z)z^{-1}]I(z) + E(z),$$

$$Y(z) = X(z)\frac{I(z)}{1 + I(z)z^{-1}} + E(z)\frac{1}{1 + I(z)z^{-1}}. \tag{4.1}$$

An ideal integrator is expressed as [23];

$$I(z) = \frac{1}{1 - z^{-1}} = \frac{z}{z - 1}. \tag{4.2}$$

Finally Eq. 4.1 becomes;

$$Y(z) = X(z) + E(z)\underbrace{(1 - z^{-1})}_{NTF}. \tag{4.3}$$

As seen in Eq. 4.3, the input signal remains unchanged while the quantization noise is shaped by the $NTF = 1 - z^{-1}$. Note that the NTF is a high pass filter with a zero at dc, so that it reduces noise components at around dc. Due to the high gain of the loop-filter in the signal band, the in-band quantization noise is strongly attenuated. The corresponding output in the time-domain is;

$$y[n] = x[n] + e[n] + e[n-1].$$

Here the first order differentiation $e[n] - e[n-1]$ of the error $e[n]$, suppresses the error at low frequencies compared to the error terms resulted by the conventional A/D converters.

Using the definition of the z-domain on the unit circle: $z \rightarrow e^{j\omega T}$, the NTF can be rewritten in the frequency-domain as;

$$NTF = 1 - e^{-j2\pi fT} = 2je^{-j2\pi fT}\sin(\pi fT). \tag{4.4}$$

The squared magnitude of the NTF results in amplification of the quantization noise by 4, but due to the term $\sin^2(\pi fT)$ it has huge attenuation at low-frequencies in the spectrum. As a result, the in-band noise power can be computed by the same procedure used in oversampling in Chapter-3;

$$\sigma_{ey}^2 = \int_{-f_B}^{f_B} P_{ey}(f)df = 2\int_0^{f_B} P_{ey}(f)df,$$

$$\sigma_{ey}^2 = 2\int_0^{f_B} \left(2\sin(\pi fT)\right)^2 P_e(f)df.$$

Using the approximation $\sin(x) \cong x$, for $\pi f_B T << \pi/2$ [31] and $P_e(f) = \sigma_e^2/f_s$ [22], and $Ts = 1/fs$, then the above equation yields;

$$\sigma_{ey}^2 = 2\frac{\sigma_e^2}{f_s}\int_0^{f_B} 4\pi^2 \frac{1}{f_s^2} f^2(df) = \sigma_e^2 8\frac{\pi^2}{3}\left(\frac{f_B}{f_s}\right)^3,$$

$$\sigma_{ey}^2 = \sigma_e^2 \frac{\pi^2}{3}\left(\frac{2f_B}{f_s}\right)^3. \tag{4.5}$$

Then the SNR can be computed as follows;

$$SNR = 10\log\left(\frac{\sigma_{xy}^2}{\sigma_{ey}^2}\right),$$

$$SNR = 10\log\left(\frac{\sigma_x^2}{\sigma_e^2}\right) - 5.17 + 30\log\left(\frac{f_s}{2f_B}\right)(dB). \tag{4.6}$$

As seen in Eq. 4.6, the in-band noise power σ_e^2 is decreasing with increasing oversampling ratio ($OSR = f_s/2f_B$). Thus for every doubling of OSR, the SNR improves by 9.03 dB, or accordingly, the resolution improves by 1.5 bits. In order to provide high resolution, it is required to use a large enough OSR. A first order $\Sigma - \Delta$ modulator is simulated for an input amplitude of 0.5, a normalized frequency of 0.01. The FFT of the PSD of the output signal is plotted in Figure 4.3. Note that the vertical peaks represent the FFT of the input signal of the normalized frequency, $\nu = f_B/f_s$, where $f_B = 0.01 f_s$. The simulation result shows the expected noise-shaping around dc and shows that the quantization noise has a significantly large attenuation in the signal-band i.e. in the frequency range of $[-f_B, f_B]$, and relative amplification at higher frequency, i.e. in the out-of-band region. The power of the input signal (σ_x^2) and quantization noise (σ_e^2) can be calculated numerically as discussed in Chapter-2. The input sine wave of 0.5 amplitude has a signal power 0.25, -0.6 dB. For the noise of a single bit quantizer, the relationship such as $\Delta = V/2^n = V/2$ can be used, so that the noise power is $\sigma_e^2 = \Delta^2/12 = (V^2/2^2)\cdot(1/12) = 0.02$. For an FFT of 32768 point sequence used in the simulation, the noise power is $1.2 \cdot 10^{-6}$ in each of the 16384 samples. Since the NTF at Nyquist corresponds to amplification by 4 in power [32], the expected power in bins (samples) around Nyquist is $5.08 \cdot 10^{-6}$, -59.2 dB. The

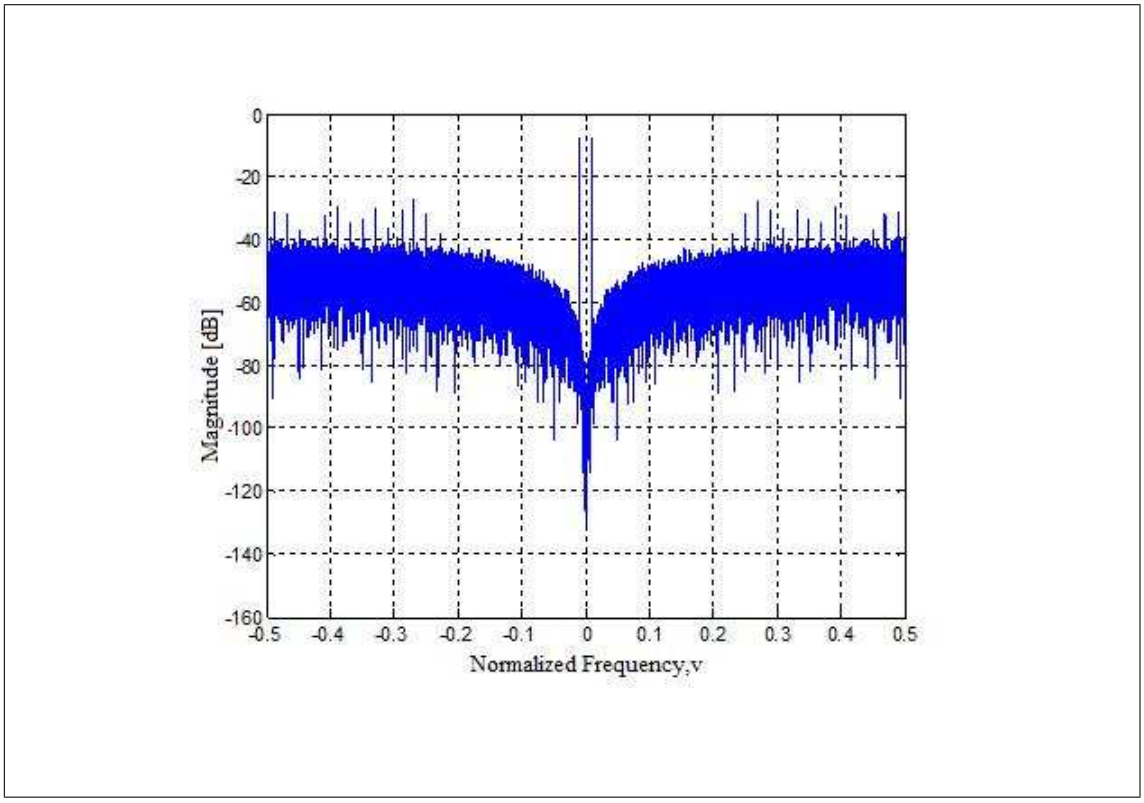

Figure 4.3 Output spectrum of a first order $\Sigma - \Delta$ modulator for a 0.5 input sine wave amplitude.

simulation results in Figure 4.3 are consistent with the calculations such that the level near Nyquist ranges between -55 and -65 dB.

4.2 Second Order Sigma-Delta Modulators

Considerable important improvements in terms of resolution and the in-band SNR values were achieved with the development of second order $\Sigma - \Delta$ modulators [29]. A standard second order $\Sigma - \Delta$ converter is constructed by adding another integrator to the first-order modulator structure as shown in Figure 4.4, which consists of two integrators (loop-filters), a quantizer and a feedback loop feeding the input. The system can be analyzed as;

$$Y(z) = X(z) + E(z)\underbrace{(1 - z^{-1})^2}_{NTF}. \tag{4.7}$$

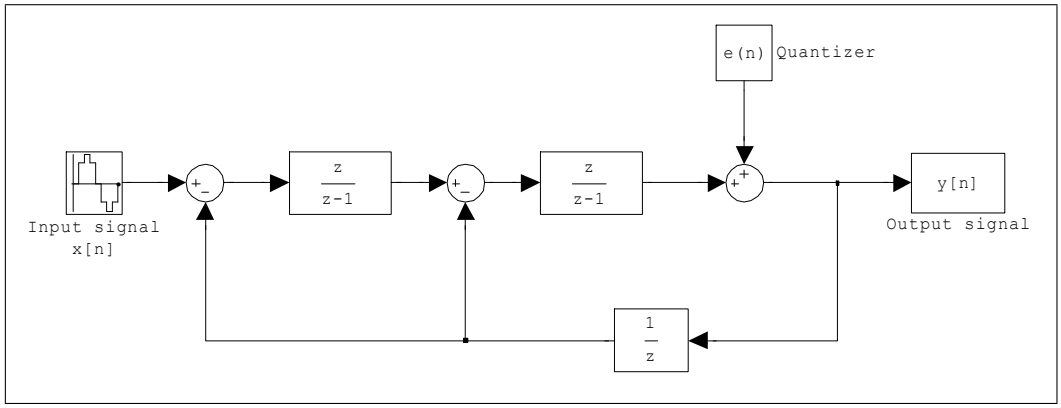

Figure 4.4 Block diagram of a second order $\Sigma - \Delta$ modulator.

This gives the NTF as $(1 - z^{-1})^2$. Note that, the past two sequences are cancelled in the NTF, which results in more attenuation at the low frequencies. The NTF can be rewritten in the frequency domain by replacing z by $e^{j\omega T}$ as;

$$NTF = (1 - e^{-j\omega T})^2 = 4je^{-j\omega T} \sin^2(\omega T/2). \tag{4.8}$$

As seen in Eq. 4.8, the output noise spectrum is shaped by the term $\sin^4(\omega T/2)$, which causes a significant attenuation of the noise components in the signal-band. The power of the output noise power can be computed using the squared magnitude of the NTF as a function of frequency.

$$\sigma_{ey}^2 = \int_{-f_B}^{f_B} P_{ey}(f)df = 2\int_0^{f_B} \left(4\sin^2(\pi fT)\right)^2 P_e(f)df,$$

$$\sigma_{ey}^2 = 2\frac{\sigma_e^2}{f_s}\int_0^{f_B} 16\pi^4 \frac{1}{f_s^4} f^4(df) = \sigma_e^2 32\frac{\pi^4}{5}\left(\frac{f_B}{f_s}\right)^5,$$

$$\sigma_{ey}^2 = \sigma_e^2 \frac{\pi^4}{5}\left(\frac{2f_B}{f_s}\right)^5, \tag{4.9}$$

$$SNR = 10\log(\frac{\sigma_x^2}{\sigma_e^2}) - 10\log(\frac{\pi^4}{5}) - 50\log\left(\frac{2f_B}{f_s}\right)(dB),$$

$$SNR = 10\log(\frac{\sigma_x^2}{\sigma_e^2}) - 1.29 + 50\log\left(\frac{f_s}{2f_B}\right)(dB). \tag{4.10}$$

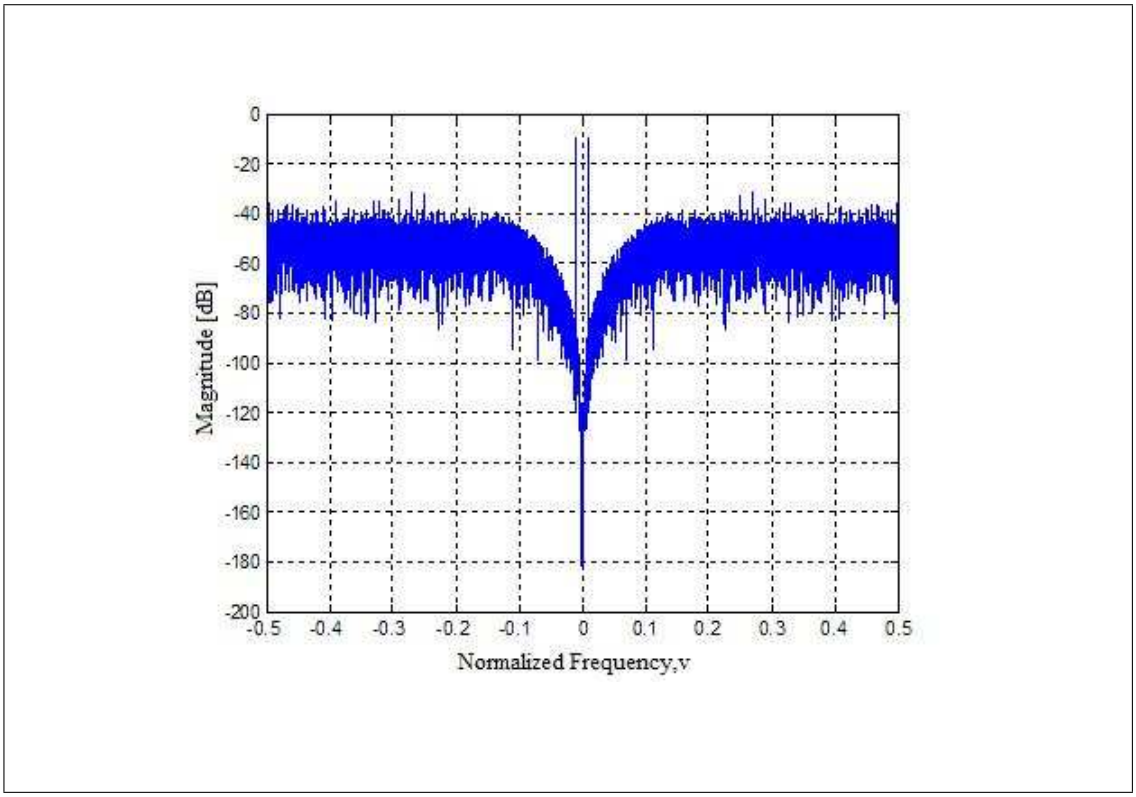

Figure 4.5 Output spectrum of a second order $\Sigma - \Delta$ modulator.

Thus, for every doubling of the oversampling ratio, $OSR = fs/2f_B$, the SNR improves by 15.05 dB, or the resolution by 2.5 bits, which is 1 bit better than the improvement achieved by a first order $\Sigma - \Delta$ modulator.

The FFT of the output spectrum of a second order $\Sigma - \Delta$ modulator simulated for a sinusoidal input signal of an amplitude of 0.5, a normalized frequency of 0.01 and dither amplitude signal of 0.03 is plotted in Figure 4.5.

Note that, compared with the output spectrum of a first order $\Sigma - \Delta$ modulator, a second order $\Sigma - \Delta$ modulator provides more attenuation of the quantization noise at low frequencies, and more amplification outside the signal-band. Furthermore, simulations show that, the output spectrum of the first order $\Sigma - \Delta$ modulator is poorly noise-shaped and has more tones in the signal band, compared to the performance results of the second order $\Sigma - \Delta$ modulator.

Using such an output spectrum, the in-band SNR value of a modulator can be calculated numerically. Figure 4.6 shows the corresponding SNR values of the first and

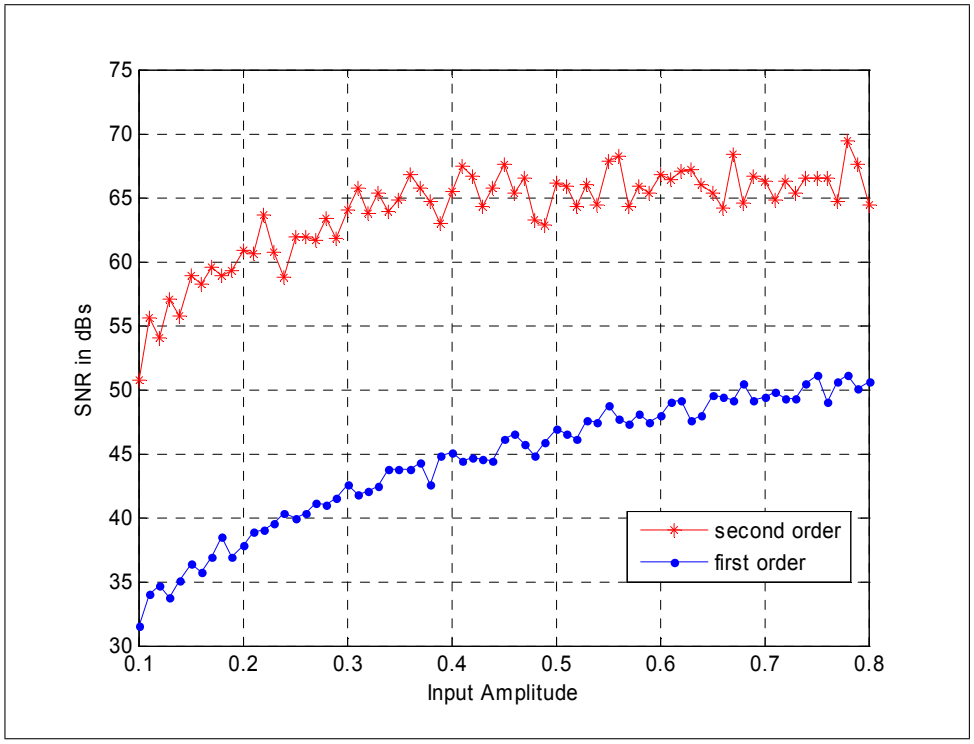

Figure 4.6 In-band SNR vs amplitude of input sinusoid for first order and second order $\Sigma - \Delta$ modulators.

second order $\Sigma - \Delta$ modulators for different input amplitudes varying between $0.1 - 0.8$ for the OSR of 128.

As expected from Eq. 4.6 and Eq. 4.10, the in-band SNR values of a second order modulator are on the average 20 dB higher than the SNR values obtained from a first order $\Sigma - \Delta$ modulator.

4.3 Tonality

In practice there are discrete tones appearing in the output spectrum because of the non-linearity of the negative feedback which can distort the signal by coupling to the baseband region [33]. The periodic components and repetitive patterns in the system like sinusoidal input signals cause harmonic tones. These tones can cause serious problems if they occur in the signal-band. Since the human eye and ear are sensitive to these repetitive signals, tones can be distinguished by humans as audio or visual. Moreover, the pattern noise in the signal band degrades the SNR values by means of

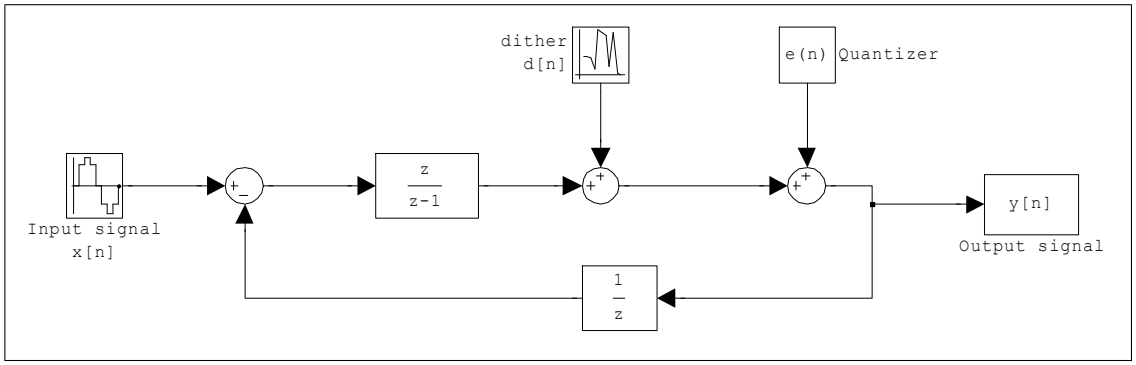

Figure 4.7 Block diagram of a first order $\Sigma - \Delta$ modulator structure with dither.

bumps and slope changes [34]. Several methods are introduced in the literature to reduce these harmonic tones, and the most commonly used technique is dithering [14]. In the dithering method, white noise i.e. random numbers are generated and added to the system in order to make the quantization noise more random and minimized in the signal-band, so that the correlation of the input signal with the quantizer output due to the feedback is reduced [35]. This pseudo-random signal is added to the input of the quantizer as shown in Figure 4.7.

On the other hand, besides the complexity of the dither circuitry, adding white noise into the spectrum reduces the SNR of the modulator; therefore the amplitude of the dither should be adjusted according to the optimum condition investigations [36]. Moreover, perfect elimination of the tones of the system requires the dither amplitude to be large, which is also a trade off for the stability of the system. Therefore, the optimum condition is hard to predict thus it should be checked by extensive simulations [30].

5. HIGH-ORDER SIGMA-DELTA MODULATORS

5.1 Single Loop Structure

High order $\Sigma - \Delta$ modulator is a straightforward extension of the first order $\Sigma - \Delta$ modulator with additional accumulators added in the feedforward loop. Single-loop modulators have only one quantizer, or comparator, as shown in Figure 5.1.
The output sequence $y[n]$ can be written as;

$$Y(z) = X(z) + E(z)\underbrace{(1 - z^{-1})^N}_{NTF}. \tag{5.1}$$

Due to Eq. 5.1, as the order (N) of the modulator increases, the attenuation of the quantization noise in lower frequencies becomes higher by pushing more noise power out of the signal band as shown in Figure 5.2. Using the $NTF = (1 - z^{-1})^N$, the in-band SNR value can be computed in the same manner as in the case of the low-order $\Sigma - \Delta$ modulators.

$$SNR = 10\log_{10}(\frac{\sigma_x^2}{\sigma_e^2}) - 10\log_{10}\left(\frac{\pi^{2N}}{2L+1}\right) + 10(2N+1)\log_{10}\left(\frac{f_s}{2f_B}\right) \quad (dB). \tag{5.2}$$

As seen in Eq. 5.2 for every doubling of the OSR, SNR improves as much as $(6N + 3)$ dB, or the resolution gains extra $(N + 0.5)$ bits. Note that Figure 5.2 and the Eq. 5.2

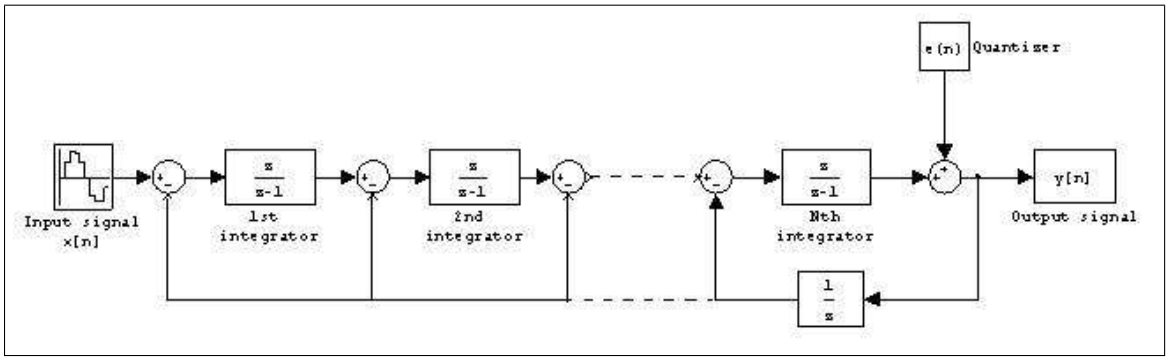

Figure 5.1 Block diagram of a N^{th} order $\Sigma - \Delta$ modulator.

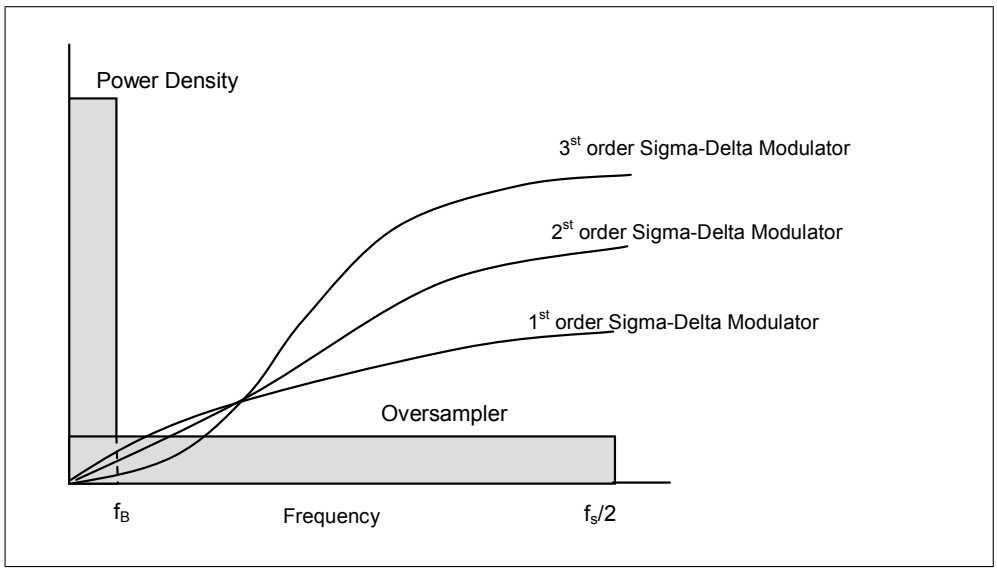

Figure 5.2 The magnitude spectra of NTFs of $\Sigma - \Delta$ modulators.

are true for the ideal case. In practice, they are not achievable because of the stability problem of the 1-bit quantizer [14]. According to the general form given in Eq. 5.1, the third order ($N = 3$) NTF is $(1 - z^{-1})^3$. For the comparison of the NTFs, the magnitude output spectra of 1^{st}, 2^{nd} and 3^{rd} order $\Sigma - \Delta$ modulators for the same sinusoidal input signal of an amplitude of 0.5 and a normalized frequency of 0.01 and the dither amplitude of 0.3 are plotted in Figure 5.3.

As seen the simulation results in Figure 5.3 and the corresponding SNR values increase as the order of the modulator increases. Moreover, the 3^{rd} order NTF secures a significant decrease of the quantization noise in the signal band, and amplification at the higher frequencies compared to the 1^{st} and 2^{nd} order NTFs. The NTF of the 1^{st} order modulator is more tonal, i.e. it has more unwanted harmonics interfaced with the signal. Even though high-order $\Sigma - \Delta$ modulators have been designed and simulated [37, 38, 39], the SNR performance in Eq. 5.2 is not achievable in practice because the NTF given in Eq. 5.1 is not stable with a 1-bit ADC for orders higher than 2 [40]. It is difficult to maintain the stability when a 1-bit quantizer is used, because of its variable gain depending on the input signal. The smaller the input amplitude is, the larger is the gain of the quantizer, which makes the linear analyses more difficult [26]. The instability of the system can be defined as the condition in which the signal levels in the modulator grow indefinitely. This indefinite growth causes the quantizer

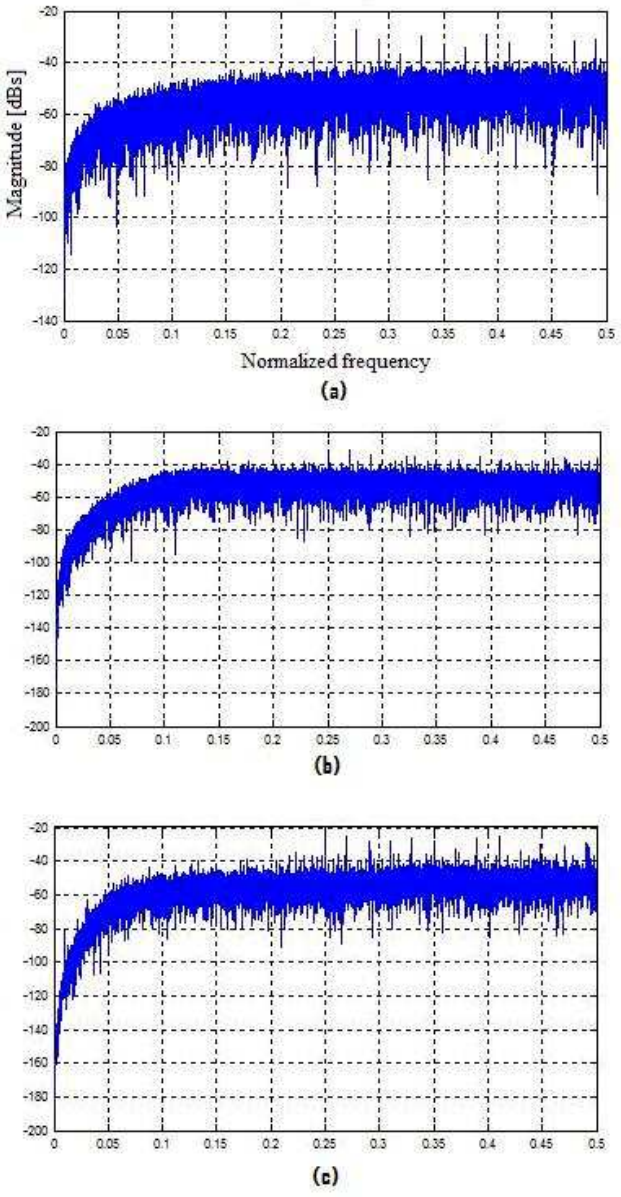

Figure 5.3 The NTF's of the (a) 1^{st}, (b) 2^{nd}, (c) 3^{rd} order $\Sigma - \Delta$ modulators.

to overload and produce an output of alternating long strings of 1's and 0's. In that condition the system have poor SNR compared with that expected by linear models [14]. Therefore, as the order of the modulator increases the modulator will become more unstable depending on the feedback coefficients, the gain of the loop-filter, non-ideality of the integrator in the feedback loop, and the amplitude of the input signal [41, 42]. Because of the non-linear nature of the quantizer, for higher order modulation, adding a quantizer especially one with a small number of bits, makes the stable linear architecture unstable [32]. According to the stability theory, the system is not stable if the gain of the loop is not adequate i.e. if the poles of the STF are outside the unit circle, which can occur if the gain of the quantizer is so large that the system have uncontrolled transients [14]. Therefore, for higher order $\Sigma - \Delta$ modulators, the coefficients are adjusted until the gain of the loop filter is appropriate to secure the stability of the system [43, 44]. When designing the NTF, their gains have to be less than 2 dB [45].

5.2 Multi-stage (Cascaded) Sigma-Delta Modulators

The cascaded structure is used to design high-order $\Sigma - \Delta$ modulators to overcome the stability problems of the single-loop structure and provide high resolution [46]. The MASH (Multi-stAge noise-SHaping) architecture consists of cascaded low-order (first or second) single-loop modulators with their own quantizers. Each modulator in the loop converts the quantization error from the previous modulator, which are then digitally canceled [26, 46]. Figure 5.4 gives the general structure of two cascaded modulators.

As seen in Figure 5.4, the quantization error of the 1st modulator $e_1[n]$ is the input of the 2nd modulator while the output of the second modulator $y_2[n]$ is combined with the output of the first modulator $y_1[n]$ via a noise cancelation circuit. As a result, the first stage quantization noise is canceled digitally. The system can be analyzed in the z-domain as follows;

$$Y_1 = X \cdot STF_1 + E_1 \cdot NTF_1, \tag{5.3}$$

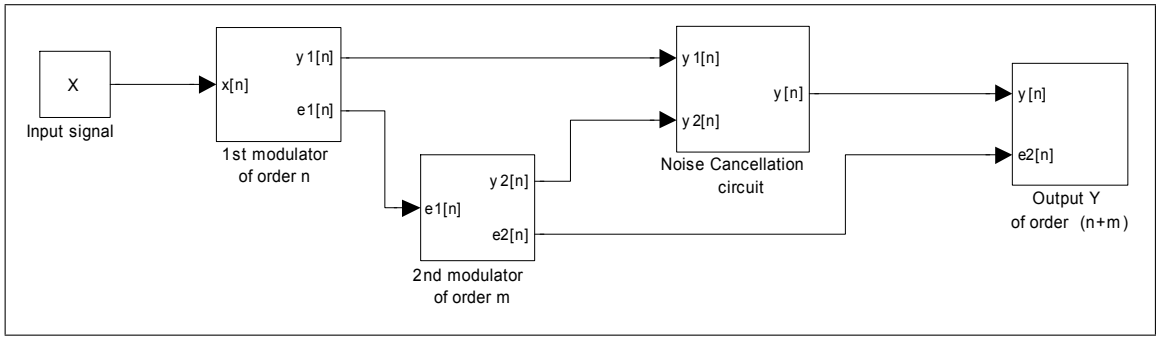

Figure 5.4 Block diagram of a cascaded $\Sigma - \Delta$ modulator.

$$Y_2 = E_1 \cdot STF_2 + E_2 \cdot NTF_2, \tag{5.4}$$

where $NTF_1 = (1 - z^{-1})^n$, $NTF_2 = (1 - z^{-1})^m$ are the noise transfer functions of the first and second modulators. The corresponding STF's are; $STF_1 = z^{-k_1}$, $STF_2 = z^{-k_2}$ for the 1^{st} and 2^{nd} modulator respectively. Then the outputs of the modulators become;

$$Y_1 = X \cdot z^{-k1} + E_1 \cdot (1 - z^{-1})^m, \tag{5.5}$$

$$Y_2 = E_1 \cdot z^{-k2} + E_2 \cdot (1 - z^{-1})^n. \tag{5.6}$$

The noise cancellation circuit cancels the quantization error of the first modulator, E_1, by the following process in the digital domain;

$$Y = Y_1 \cdot STF_2 - Y_2 \cdot NTF_1. \tag{5.7}$$

Using the explicit forms of the transfer function given in Eq. 5.5 and Eq. 5.6 so that the output becomes;

$$Y = X \cdot z^{-(k1+k2)} + E_2 \cdot (1 - z^{-1})^{m+n}. \tag{5.8}$$

As seen in Eq. 5.8, the first stage error is canceled digitally by the signal process of the cancelation circuit. Moreover, the signal is just delayed at the output while the quantization error contributed from the second modulator is shaped by the NTF of order $m + n$.

The overall system is still stable because the structure contains only feedforward paths

and no feedbacks between the single-loop modulators [14]. Using this advantage of the inherent stability of low-order $\Sigma - \Delta$ modulators, high order modulators of any order can be constructed. Beside the improvements in stability, the cascaded modulators have fewer tones compared to a first or second order $\Sigma - \Delta$ modulators [47].
On the other hand, in reality the error contribution from the first modulator, E_1, does not completely cancel out because the NTF of the first modulator may not be exactly equal to $(1 - z^{-1})^m$. The mismatch of the components and the non-idealities of the op-amps cause residual noise at the output. The noise leakage is [32]:

$$E_{1,out} = (NTF_{expected} - NTF_{ideal})E_1. \tag{5.9}$$

The non-idealities cause a shift in the NTF as much as the δ so that the zero of the NTF is moved from $z = 1$ to $z = 1 - \delta$. When the case of the first order modulator is considered, then the residual noise term yields to;

$$E_{1,out} = [(1 - z^{-1}) - (1 - (1 - \delta)z^{-1})] \cdot E_1 = \delta \cdot z^{-1} \cdot E_1. \tag{5.10}$$

The quantization noise of the second modulator, E_2, is attenuated by an order $(m+n)$ as seen in Eq. 5.8 and the in-band power of the residual noise E_1,out is shaped by δ^2, which is lower than the power of E_2.

$$\log(\frac{\delta^2}{OSR}) < \log\left(\frac{\pi^{2N}}{2N+1} \cdot \frac{1}{OSR^{2N+1}}\right). \tag{5.11}$$

Therefore the overall in-band SNR value given in Eq. 5.2 does not become worse, so that the general structure given in Figure 5.4 can be extended to any stages for the desired order of the modulator. However, these mismatches between the actual NTF and the ideal NTF restrict the maximum number of the stages used in the MASH structure, to be limited to three [32]. For the case of the 1-1-1 cascaded third order modulator, another single-loop modulator will be added to the diagram Figure 5.4. Figure 5.5 gives the block diagram of a 1-1-1 cascaded third order $\Sigma - \Delta$ modulator with the analyzed noise cancelation circuitry. As seen in Figure 5.5, the modulators use the quantization error of the preceding modulators as the input and finally the outputs of all the modulators are added and manipulated through the signal processing via

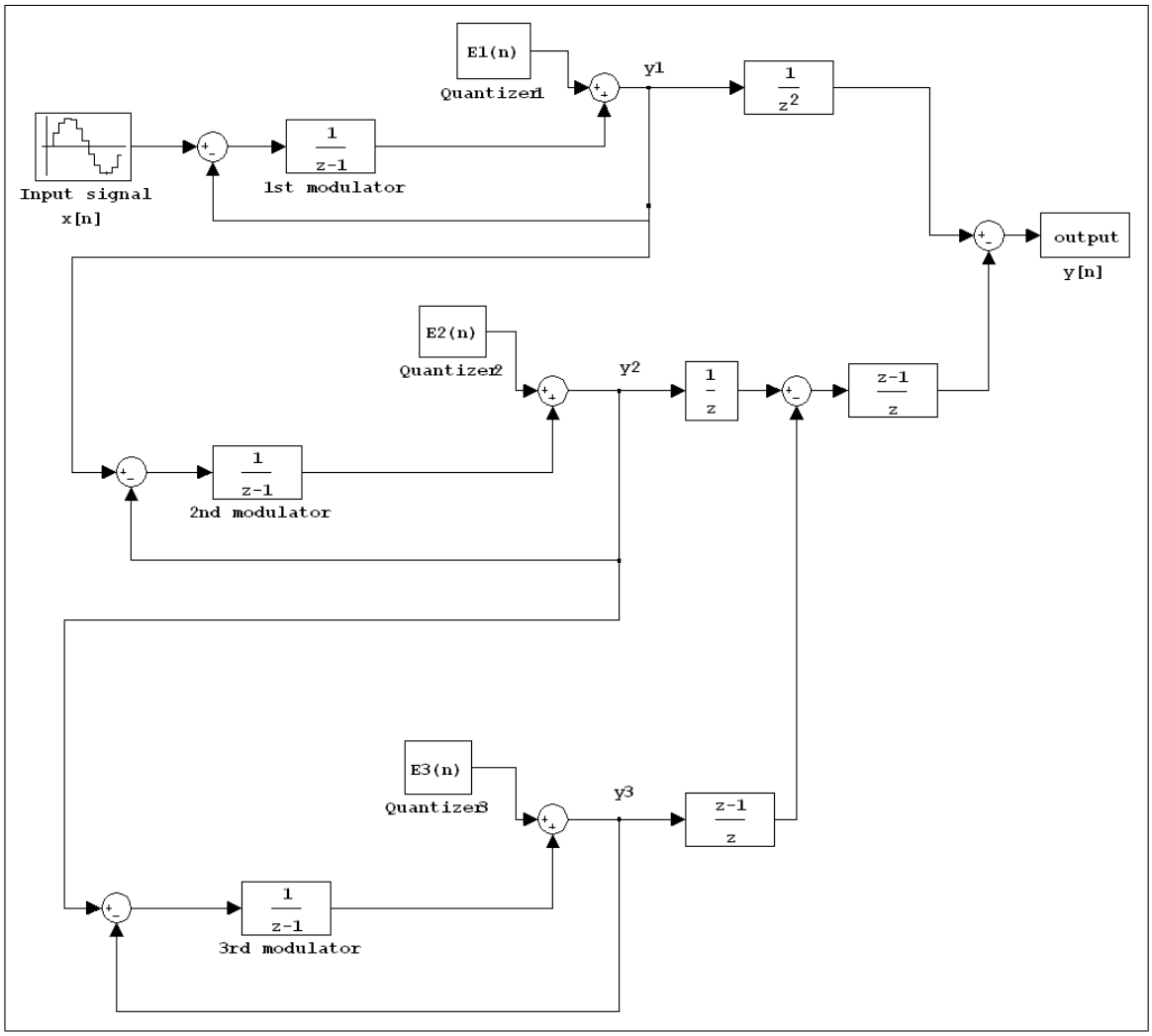

Figure 5.5 1-1-1 cascade: a 3^{rd} order $\Sigma-\Delta$ modulator by cascading three 1^{st} order $\Sigma-\Delta$ modulators.

some noise cancelation circuits. Y_1, Y_2, Y_3 are the outputs of the first, second and third modulators, respectively.

$$Y_1 = X(z^{-1}) + E_1(1 - z^{-1}),$$

$$Y_2 = E_1(z^{-1}) + E_2(1 - z^{-1}),$$

$$Y_3 = E_2(z^{-1}) + E_3(1 - z^{-1}).$$

To eliminate the quantization error terms of the second modulator, E_2;

$$Y^{'} = \left[Y_2 \cdot (z^{-1})\right] - \left[Y_3 \cdot (1 - z^{-1})\right] = E_1(z^{-1})^2 - E_3(1 - z^{-1})^2.$$

The output $Y[z]$ is obtained in the same manner by canceling the quantization error contributed from the first modulator E_1.

$$Y[z] = \left[Y_1 \cdot (z^{-1})^2\right] - \left[Y' \cdot (1 - z^{-1})\right] = X \cdot (z^{-1})^3 - E_3 \cdot (1 - z^{-1})^3. \tag{5.12}$$

As obtained in Eq. 5.3, the input sequence is delayed by the $STF = (z^{-1})^3$ and the error term is shaped by $NTF = (1 - z^{-1})^3$.

Figure 5.6 gives the output spectrums of 3^{rd}-order $\Sigma - \Delta$ modulators using single-loop structure and 1-1-1 cascaded structure for the same input signal of the input amplitude of 0.5 and normalized frequency of 0.01. Note that, the output power spectrum of the MASH structure has fewer tones and higher attenuation of the noise components in the signal-band, compared to the single-loop structure.

As a result of the MASH structure, a higher order $\Sigma - \Delta$ modulator is obtained whose overall system stability is guaranteed by the unconditional stable low-order $\Sigma - \Delta$ modulators. Higher order structures can be designed only from 1^{st} order modulators [46] or also using 2^{nd} order modulators [48, 49]. However, more than three cascaded stages introduce quantization error leakage to the output and reduce the performance of the modulator.

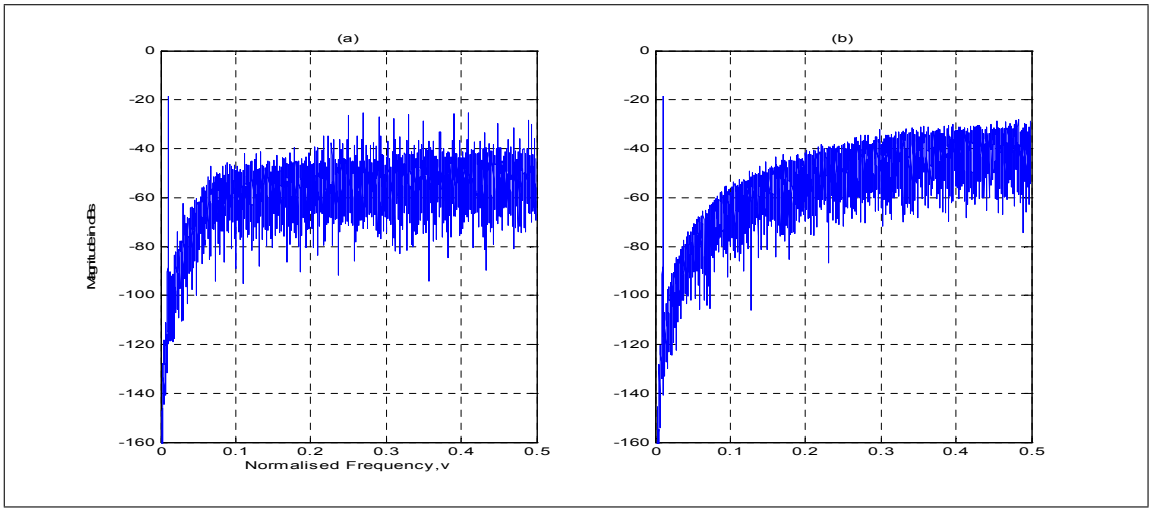

Figure 5.6 3^{rd} order $\Sigma - \Delta$ modulator using the structure of (a) single loop, (b) MASH structure.

5.3 Butterworth High-Pass Response

Using the n^{th} order pure differentiator $H(z) = (1 - z^{-1})^n$ as the NTF causes instability for higher number of n, as discussed before. One approach to this problem is to introduce poles into the $H(z)$ to flatten the response at higher frequencies [45].

$$H(z) = \frac{(z-1)^n}{D(z)}. \tag{5.13}$$

As seen in Figure 5.7, the $H(z)$ has a flat response in the out-of band region due to the $D(z)$ in the denominator.

The poles can be chosen according to a Butterworth alignment so that the 3 dB-gain rules as well as the causality rules are satisfied [14].

5.4 Inverse Chebyshev Complex Response

The Butterworth response can be modified so that the zeros are moved to other frequencies from dc i.e. to the complex locations on the unit circle in the vicinity of dc (zero splitting). As a result of these complex alignments, compared to the Butterworth alignment, SNR improvements and more attenuation of the noise contribution in the

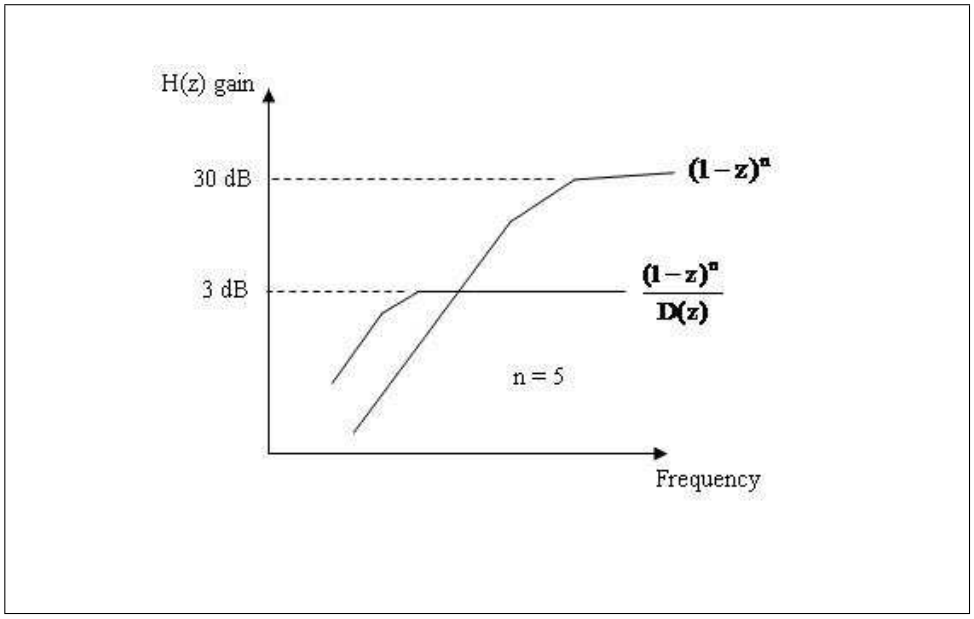

Figure 5.7 The comparison of the frequency responses of the $H(z)$ after modification.

in-band region are achieved [14]. In order to have complex zeros besides the real zeros, one should use inverse Chebyshev filters instead of Butterworth filters [45, 50]. The lower and upper frequencies of the NTF are selected so as to ensure that the input signal is positioned at the centre of the signal bandwidth.

5.5 Loop Filter Topologies

There are many structures and circuit topologies to design LP modulators based on the same universal single-loop structure as given in Figure 4.1 [14].The signal is filtered by the STF and the noise is shaped by the NTF, which are defined by the loop-filter $H(z)$ as;

$$STF = \frac{H(z)}{1 + H(z)}$$

and

$$NTF = \frac{1}{1 + H(z)}.$$

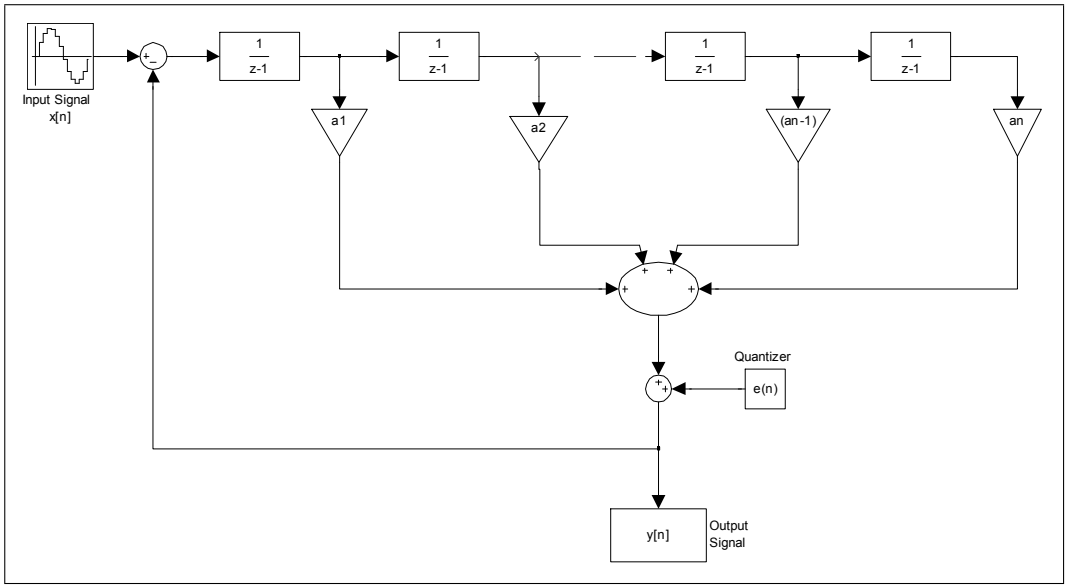

Figure 5.8 Chain of accumulators with weighted feedforward summation.

The circuit topologies of the single-loop structure modulators can be modified with adding extra feedback paths. There are many possible design implementations, however the most frequently used structures are: chain of accumulators with weighted feedforward summation [51, 37] and chain of accumulators with feedforward summation with local resonator feedbacks [52, 53].

5.5.1 Weighted Feedforward Summation

The design topology consists of cascaded integrators with the transfer functions $H(z) = z^{-1}/(1-z^{-1})$, whose outputs are weighted and summed up to form the overall loop-filter transfer function, $L(z)$. The summation output is used as the input of the quantizer generating the feedback signal $y[n]$ [14]. The structure should have a delay of at least one sample period to maintain the causality of the system [54], as shown in Figure 5.8.

The linear system analysis gives the transfer function of the loop-filter, $L(z)$;

$$L(z) = \frac{1}{(z-1)} \cdot a_1 + \frac{1}{(z-1)^2} \cdot a_2 + \frac{1}{(z-1)^3} \cdot a_3 + ... + \frac{1}{(z-1)^n} \cdot a_n. \qquad (5.14)$$

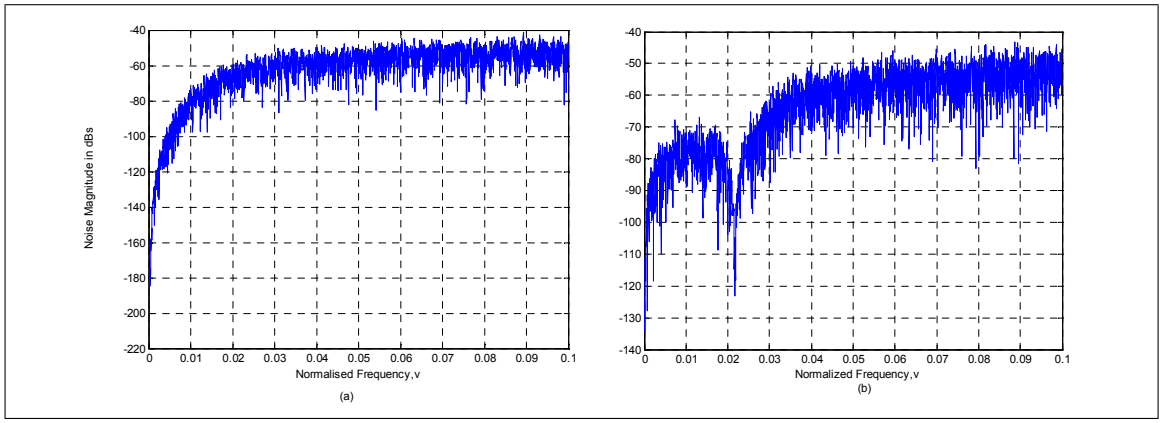

Figure 5.9 5^{th} order $\Sigma-\Delta$ modulator using the chain of accumulators structure with local feedbacks.

In which, n is the order of the loop-filter, a_i, for $i = 0, 1, ..., n$, are the feedforward coefficients to determine the poles of the loop-filter or NTF zeros. As seen in Eq. 5.14 all the poles of $L(z)$ are at dc, i.e. at $z = 1$. Therefore, a Butterworth high-pass filter can be used to obtain adequate coefficients that make the system stable. Once the NTF is obtained from the linear system analysis, the corresponding $L(z)$ can be computed from the relationship that $NTF = 1/(1 + L(z))$, it is then equated to the Butterworth NTF to solve for the desired feedforward coefficients.

5.5.2 Feedforward summation with Local Feedbacks

For relatively large signals bands, the zeros of the NTF do not need to be at a certain frequency to reduce the noise at certain points. Instead it is necessary to have a low noise level over the entire signal band [32]. The distribution of the NTF zeros across the signal band will cause moderate attenuation, when compared with having all zeros concentrated at a single frequency. The corresponding structure is shown in the Figure 5.9, which is achieved by adding a small negative feedback around pairs of integrators, so that the zeros of the loop-filter are shifted away from $z = 1$ [14]. As seen in the diagram, the second integrators of the pairs are without delay.

In which, a_i, for $i = 0, 1, ..., 5$, are the feedforward coefficients and b_1, b_2 are the gains of the negative feedbacks around the integrator pairs. For the case of one pair of the

integrators, the loop transfer function yields:

$$L(z) = \frac{z(a_1 + a_2) - a_1}{z^2 + z(b_1 - 2) + 1}. \tag{5.15}$$

As seen in Eq. 5.15, the poles of the $L(z)$ are moved away from the real axis to complex points on the unit circle, therefore the inverse Chebyshev filter can be used to obtain the desired coefficients. The coefficients can be solved by equating L(z) obtained from the system analysis ; to the transfer function obtained from the NTF of the Chebyshev filter [45].

Note that the poles of the transfer function of the loop-filter become zeros of the corresponding NTF, therefore the local feedbacks determine actually the shift of zeros away from $z = 1$. These zeros can be used to have a flat transfer function in the signal band and prevent a high STF gain at higher frequencies so that the overall performance of the modulator is improved. The signal band may be extended but this will be at the cost of a lower SNR value [32, 50].

Using MATLAB, the Butterworth and Inverse Chebyshev filters can be designed according to the implementation specifications. The feedforward coefficients for a third-order Butterworth filter are calculated as $a_1 = 0.3138, a_2 = 0.0473, a_3 = 0.0033$. For a third order inverse Chebyshev filter, the feedforward coefficients are: $a_1 = 0.3648$, $a_2 = 0.0573$, $a_3 = 0.0012512$ and the feedback coefficient: $b_1 = 0.0185$. The corresponding modulator is simulated for a dither signal of amplitude 0.3. Figure 5.10 compares the simulation results of the NTF's of third order modulators with (a) weighted feedback summation structure, that has all the zeros at $z = 1$, (b) weighted feedback summation with local resonators, that has one zero at $z = 1$ and others moved to complex conjugates on the unit circle.

At low frequencies, there is higher noise suppression when all the zeros of the NTF are at $z = 1$, as shown in Figure 5.10. As a comparison; in (a) all the zeros are located at dc ($z = 1$) and in (b) there are complex conjugate zeros. However for a signal-band at the frequencies around $\nu = 0.02$, the second modulator with complex zeros becomes more effective by means of noise-shaping.

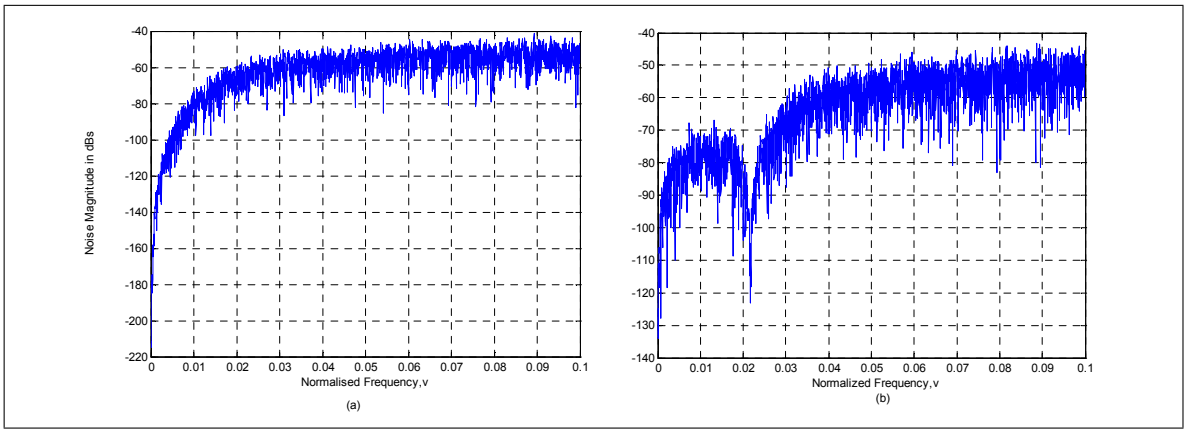

Figure 5.10 NTF's of a third order $\Sigma - \Delta$ modulator using the chain of integrators (a) weighted feedforward summation, (b) weighted feedforward summation and local feedbacks.

6. BAND-PASS SIGMA-DELTA MODULATORS

Band-pass $\Sigma-\Delta$ modulators with high resolution performance [55] have typical applications in many diverse areas especially in modern receiver systems to convert high frequency narrow-band signals [30], AM digital radios [55], digital radio systems [7], cellular mobile radios [56], cellular telephony [9], phased-array ultrasound imaging [2], RF communication receivers [57] and satellite communication services [11]. Low-pass $\Sigma-\Delta$ modulators use a sampling frequency, f_s, that is much greater than the highest frequency of the input signal, which is also the bandwidth of the signal, f_B. However, the highest frequency component of a band-pass signal is shifted to a much higher frequency as much as the center frequency of the signal, f_o, i.e. it is located at $f_o + f_B/2$. Therefore, for band-pass signals with very large f_o, as IF signals, choosing the sampling rate much greater than the highest frequency will be unreasonably large to achieve [26]. Thus, according to the band-pass sampling theorem, BP $\Sigma-\Delta$ modulators have a sampling rate much greater than the signal bandwidth instead of the highest frequency in the input signal, $f_s >> f_B$ [57]. The loop-filter used in the BP $\Sigma-\Delta$ modulators have very high gain in the signal band centred at f_o in order to give a big attenuation of the in-band noise while the input signal remains unchanged [55]. The corresponding block diagram and the behavior of the NTF and the STF are given below in Figure 6.1. $\Sigma-\Delta$ modulators, LP or BP, have a small amount of noise in the narrow band around the zeros of the loop-filter. However, unlike the high-pass NTFs of the LP $\Sigma-\Delta$ modulators, that have zeros at around $z = 1$, the NTFs realized by the BP $\Sigma-\Delta$ modulators have zeros in the signal band around f_o, which cause the NTF to be band-stop and the loop-filter to have an infinite gain in the signal band region $[f_o \pm f_B/2]$ [58].

Moving the poles of the loop-filter, $H(z)$, from dc to complex conjugates on the unit circle cause $H(z)$ to be infinite around f_o [55]. As discussed before, the poles of $H(z)$ become the zeros of the NTF and $H(z)$ defines directly the NTF and STF of the

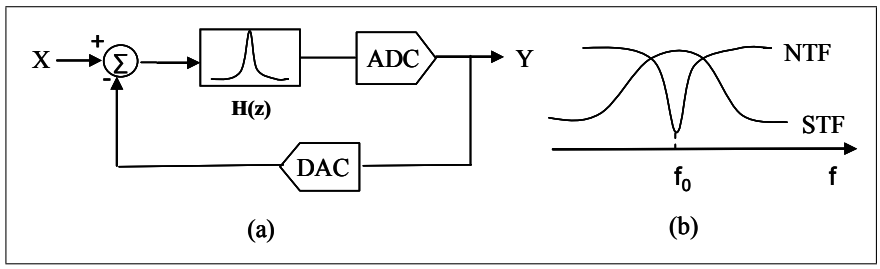

Figure 6.1 (a) Block diagram of a BP $\Sigma - \Delta$ modulator (b) Typical NTF and STF.

modulator as shown below;

$$STF = \frac{H(z)}{1 + H(z)} \qquad \text{and} \qquad NTF = \frac{1}{1 + H(z)}. \tag{6.1}$$

Therefore, the infinite gain of the $H(z)$ provides the NTF to go to zero and the STF to become unity in the signal region, while away from the centre frequency, the NTF gives rise to the quantization noise in the out-of band region, as illustrated in Figure 6.1.

6.1 Band-Pass $\Sigma - \Delta$ Modulator Loop-Filter Design

The simplest and the most common way to design the loop-filter for a BP $\Sigma - \Delta$ modulator is to derive it from a LP $\Sigma - \Delta$ modulator via simple mathematical transformations in [55]. In this LP prototype method, a low-pass-to-band-pass ($LP \rightarrow BP$) transformation is applied on a suitable LP modulator, so that from a LP modulator of order n, a BP modulator of order $2n$ is obtained by maintaining the stability of the system as well as the noise properties of the original case [14]. The LP prototype can be a single-loop structure [59] as well as a MASH structure [60, 61]. The loop-filter transfer function can be obtained by applying a low-pass-to-band-pass transformation at the points $z = \pm e^{j2\pi\nu}$. By moving the zeros from $z = 1$ to complex conjugates, The NTF yields;

$$NTF = \frac{(z - e^{j2\pi\nu})(z - e^{-j2\pi\nu})}{z^2}. \tag{6.2}$$

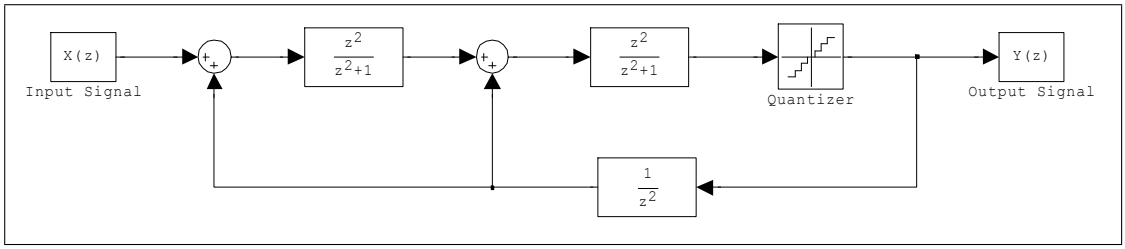

Figure 6.2 A 4^{th}-order band-pass $\Sigma - \Delta$ modulator obtained with $z^{-1} \rightarrow -z^{-2}$ transformation.

The Eq. 6.2 can be rewritten explicitly;

$$NTF = \frac{z^2 - ze^{j2\pi\nu} + ze^{-j2\pi\nu} + 1}{z^2} + \frac{z^2 - z(e^{j2\pi\nu} + e^{-j2\pi\nu}) + 1}{z^2}. \tag{6.3}$$

Using $\frac{e^{j2\pi\alpha}+e^{-j2\pi\alpha}}{2} = \cos\alpha$ [31], NTF yields;

$$NTF = \frac{z^2 - 2z\cos 2\pi\nu + 1}{z^2}. \tag{6.4}$$

The conventional form of Eq. 6.4 can be written as;

$$NTF = 1 - (2\cos 2\pi\nu)z^{-1} + z^{-2}. \tag{6.5}$$

Since $H(z) = (1 - NTF)/NTF$, the transfer function of the loop-filter becomes;

$$H(z) = \frac{(2\cos 2\pi\nu)z^{-1} - z^{-2}}{1 - (2\cos 2\pi\nu)z^{-1} + z^{-2}}. \tag{6.6}$$

Note that the above generalized equation Eq. 6.4 is valid for all values of the normalized frequency v. There are some special cases used in the literature due to the circuit design simplicity [14]. For the case of $\nu = 0.25$, which implies that $2\pi\nu = \pi/2$ or $z = \pm e^{j2\pi\nu} = \pm j$, the loop-filter yields;

$$H(z) = \frac{-z^{-2}}{1 + z^{-2}}. \tag{6.7}$$

Note that, Eq. 6.5 is the mapping of $z^{-1} \rightarrow -z^{-2}$ applied to the LP prototype, which is not complicated to design. As seen below, Figure 6.2 is a transformed BP version of the second-order LP modulator given in Figure 4.4.

The transformation of $z^{-1} \rightarrow -z^{-2}$ in the LP loop-filter transfer function, dou-

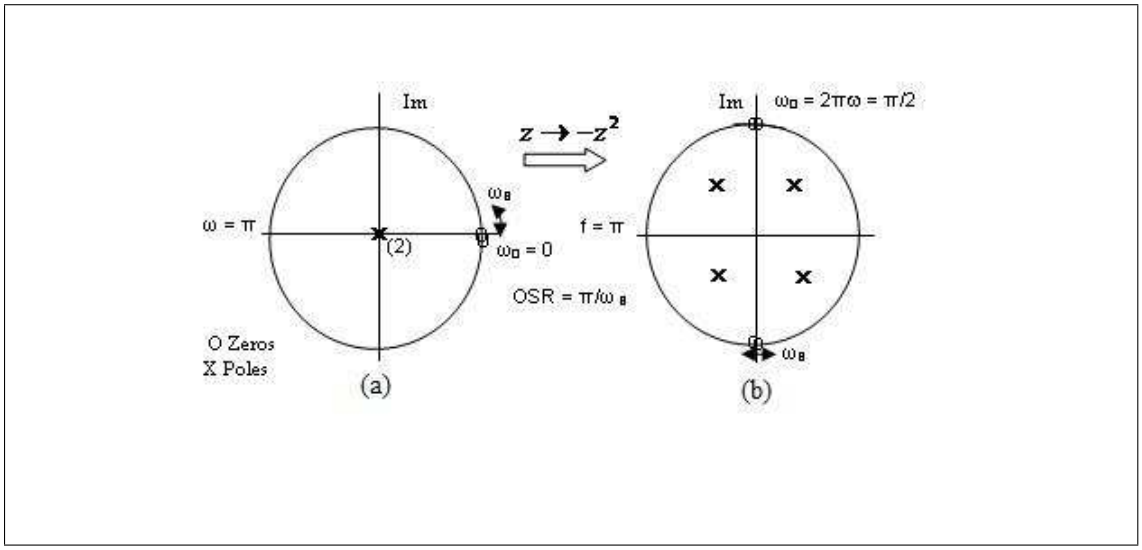

Figure 6.3 The pole-zero alignments of the NTFs for (a)LP (b)BP $\Sigma - \Delta$ modulators.

bles the order of the LP NTF and shifts the zeros of the NTF from dc to $\pm\pi/2$ i.e. from $z = 1$ to $z = \pm j$. The corresponding locations of the zeros of the LP and BP NTFs are given in Figure 6.3. Note that ω_B is the normalized bandwidth, which is a narrow-band surrounding the zeros and $\omega_0 = 2\pi f_o$ [14].

Figure 6.4 shows the corresponding magnitude spectrum of the NTF of the fourth-order BP $\Sigma - \Delta$ modulator, where the zeros of the NTF are moved from dc to $\pm\pi/2$ or in terms of the normalized frequency $\nu = 0.25$.

As seen in Figure 6.4, the quantization noise is significantly reduced in the narrow-band around the normalized centre frequency 0.25 and pushed away from the signal band region. This band-reject noise-shaping of the BP modulators provides high SNR values while lowering the sampling rate used by LP $\Sigma - \Delta$ modulators [62]. Furthermore, as expected the spectrum is exactly equivalent to two copies of the original LP prototype modulator, which are centered at $\nu = \pm 0.25$. Therefore, the stability properties are also the same as obtained by LP $\Sigma - \Delta$ modulators [30]. Another special case is $\nu = 0.125$, that gives $2\pi\nu = \pi/4$, so that the loop-filter becomes;

$$H(z) = \frac{z^{-1}\sqrt{2} - z^{-2}}{1 - z^{-1}\sqrt{2} + z^{-2}}. \tag{6.8}$$

The PSD of the output of a 4^{th} order BP $\Sigma - \Delta$ modulator with a loop-filter transfer function defined in Eq. 6.6 is plotted in Figure 6.5. For the simulation, a sinusoidal

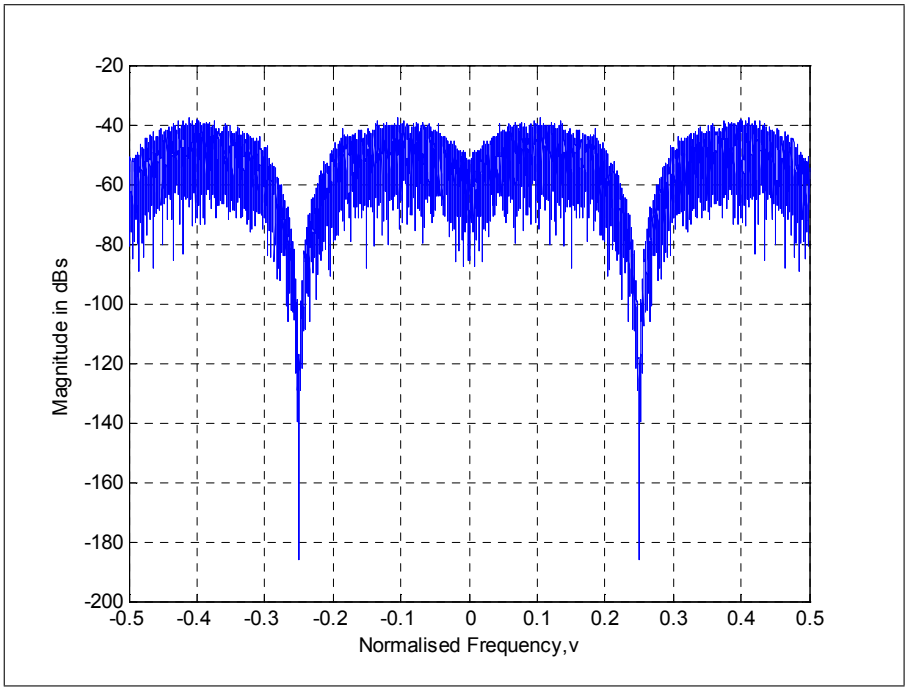

Figure 6.4 The NTF of a 4th-order $\Sigma - \Delta$ modulator with resonant frequency $\nu = 0.25$.

input signal of the frequency of $f_o = \pi/4$ and amplitude of 0.5, is used, which is represented as the vertical peaks in the plot.

The simulation result shows the expected noise-shaping around $\omega_0 = \pi/4$ and relative amplification away from the center frequency, i.e. in the out-of-band region. On the other hand, non-integer coefficients in the loop transfer function given in Eq. 6.6 make the circuit implementation difficult, because of the problems faced by satisfying non-integer capacitances. These possible inaccuracies in design alter the NTF so that the zeros are shifted away from the unit-circle and the noise attenuation is degraded in the signal band around the center frequency, f_o [32].

6.2 Loop-Filter Topologies

BP $\Sigma - \Delta$ modulators preserve many advantages of the LP $\Sigma - \Delta$ modulators and have the same structural variety as LP $\Sigma - \Delta$ modulators with all the trade-offs, so that the NTFs of BP modulators are faced with the same stability constraints as their LP counterparts. The transformation methodology from LP to BP $\Sigma - \Delta$ modulators

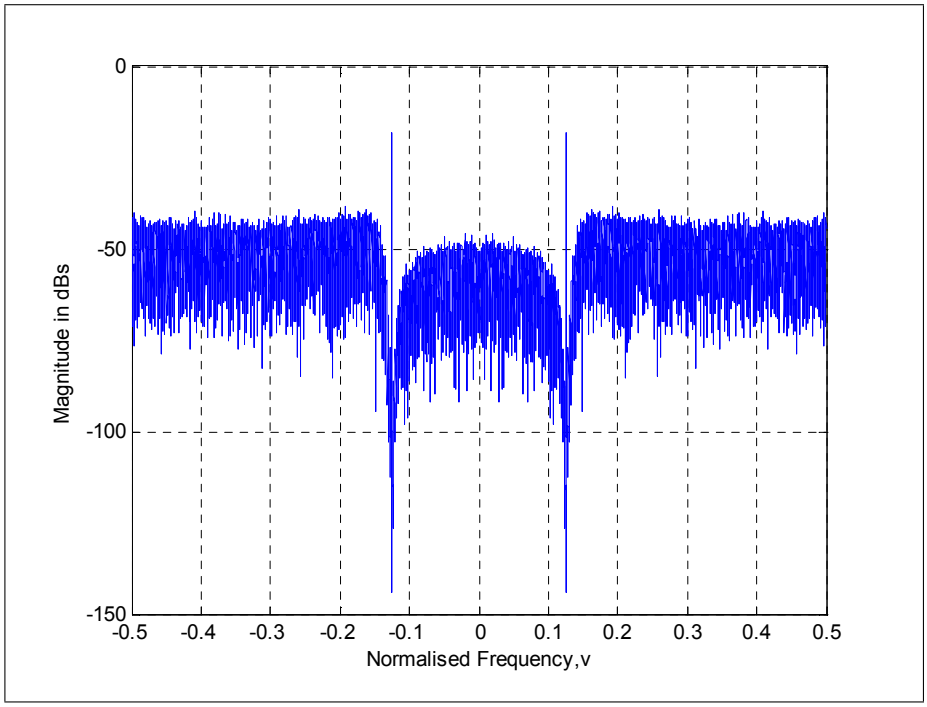

Figure 6.5 Output spectrum of a 4^{th} order BP $\Sigma - \Delta$ modulator with resonance frequency of $\nu = 0.125$.

can be realized with any structure discussed in the Chapter-5, by mapping each delay component with two delay components [30]. Therefore, the same loop-filter topologies, given in the Chapter-5 for LP $\Sigma-\Delta$ modulator can be transformed simply for BP $\Sigma-\Delta$ modulators. There are many possible design implementations; however two of them are analyzed here: the chain of accumulators with weighted feedforward summation and the chain of accumulators with feedforward summation and local resonator feedbacks.

6.2.1 Chain of Resonators with Weighted Feedforward Summation

The structure shown in Figure 6.7 is a transformed version of the topology used in Chapter-5 for LP $\Sigma - \Delta$ modulators, which consists of a chain of resonators whose outputs are weighted and summed up and used as the input of the quantizer generating the feedback signal $y[n]$. Note that the resonators are of the form $z^{-2}/(1 + z^{-2})$ to have noise suppression at $\nu = 0.25$ to form the loop-filter of the system, $L(z)$.

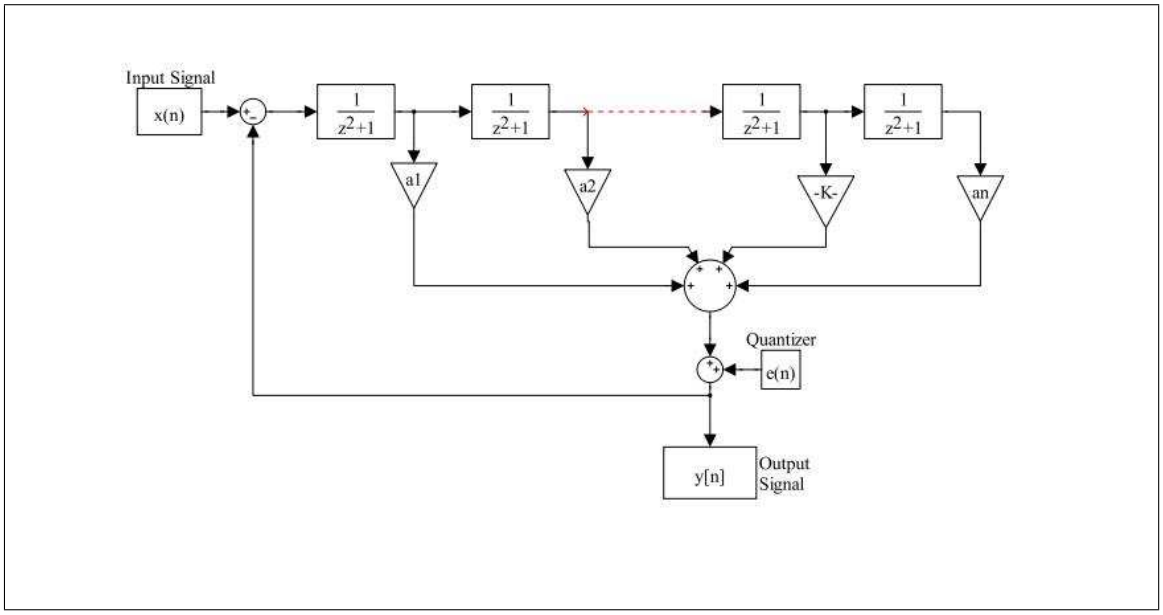

Figure 6.6 Loop-filter topology for a 4^{th} order BP $\Sigma - \Delta$ modulator using cascaded integrators with feedforward coefficients.

The loop-filter transfer function results by linear system analyses as;

$$L(z) = \frac{1}{z^2+1}a_1 + \frac{1}{(z^2+1)^2}a_2 + ... + \frac{1}{(z^2+1)^n}a_n, \tag{6.9}$$

where, n is the order of the loop-filter, a_i, for $i = 0, 1, ..., n$, are the feedforward coefficients to determine the poles of the loop-filter or the zeros of the NTF. As seen in Eq. 5.14 all the poles of $L(z)$ are at $\nu = 0.25$, i.e. at $z = \pm j$. Therefore, a Butterworth BP filter can be used to obtain the adequate coefficients that make the system stable by reducing the magnitude of the NTF gain in order to provide maximally flat out-of-band gain [63]. Once the NTF is obtained from the linear system analysis, the corresponding $L(z)$ can be computed from the relationship that $NTF = 1/(1 + L(z))$, it is the equated to the Butterworth NTF to solve for the desired feedforward coefficients. The required Butterworth filter can be designed using MATLAB. For a 4^{th} order structure, the feedforward coefficients are calculated as $a_1 = -0.1773$ and $a_2 = 0.0145$. The corresponding $\Sigma - \Delta$ modulator is simulated for an input sinusoid of amplitude of 0.5 and frequency of $\pi/2$ and a dither signal of amplitude of 0.05. The simulation result is shown in Figure 6.8.

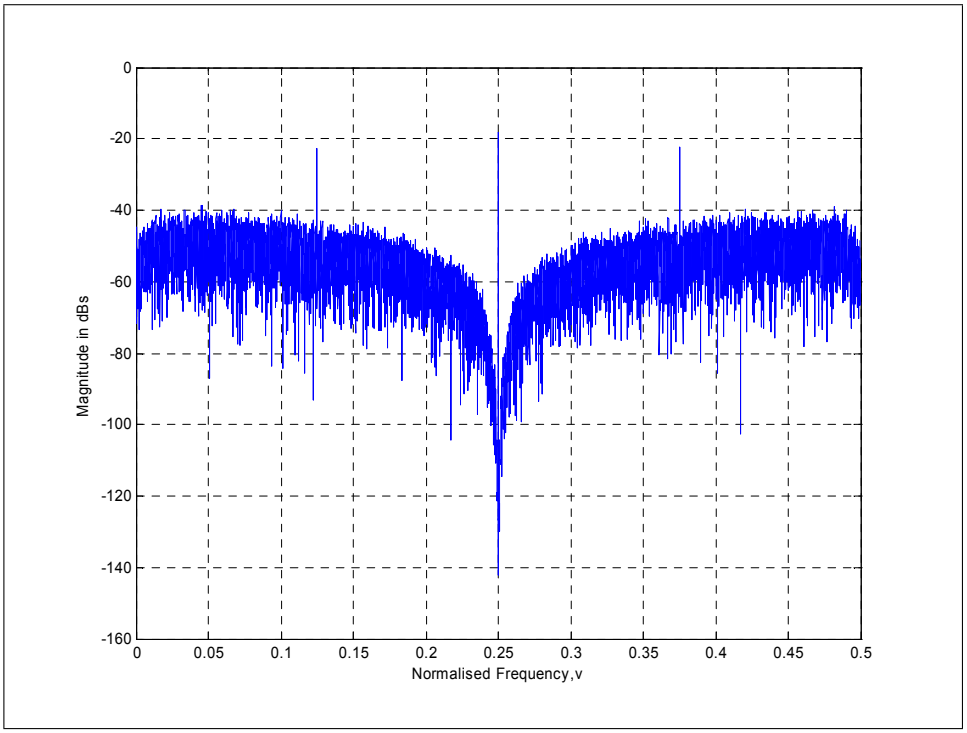

Figure 6.7 The output power spectrum of a 4th order BP $\Sigma - \Delta$ modulator employing weighted feedforward summation structure.

As expected, there is a sharp attenuation of quantization noise in the signal band around 0.254.

6.2.2 Chain of Accumulators with Feedforward Summation and Local Feedbacks

The loop topology is derived from the LP modulator topology in Figure 5.8 by mapping $z \rightarrow -z^2$. The corresponding structure is shown in Figure 6.9, which is composed of small negative feedbacks around pairs of integrators, which are summed up prior to the quantizer input. As seen in the diagram, the second integrators of the pairs are without delay. a_i, for $i = 0, 1, ..., 5$ are the feedforward coefficients and b_1, b_2 are the gains of the negative feedbacks around the integrator pairs.

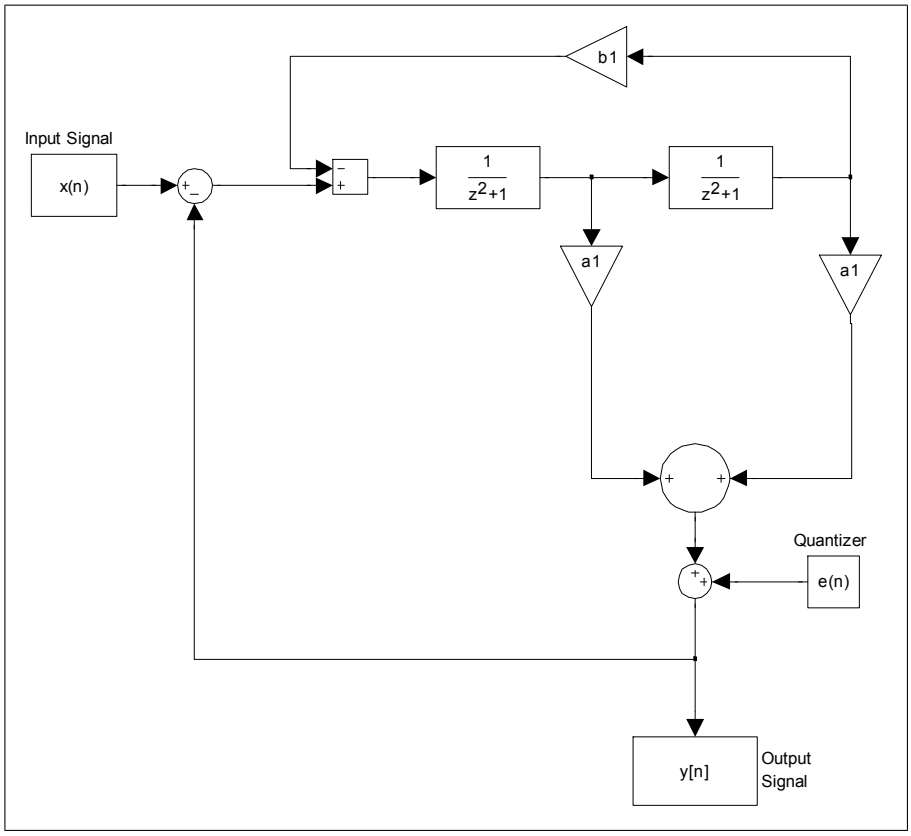

Figure 6.8 4^{th} order BP $\Sigma - \Delta$ modulator designed with the topology of chain of accumulators with feedforward summation and local feedbacks.

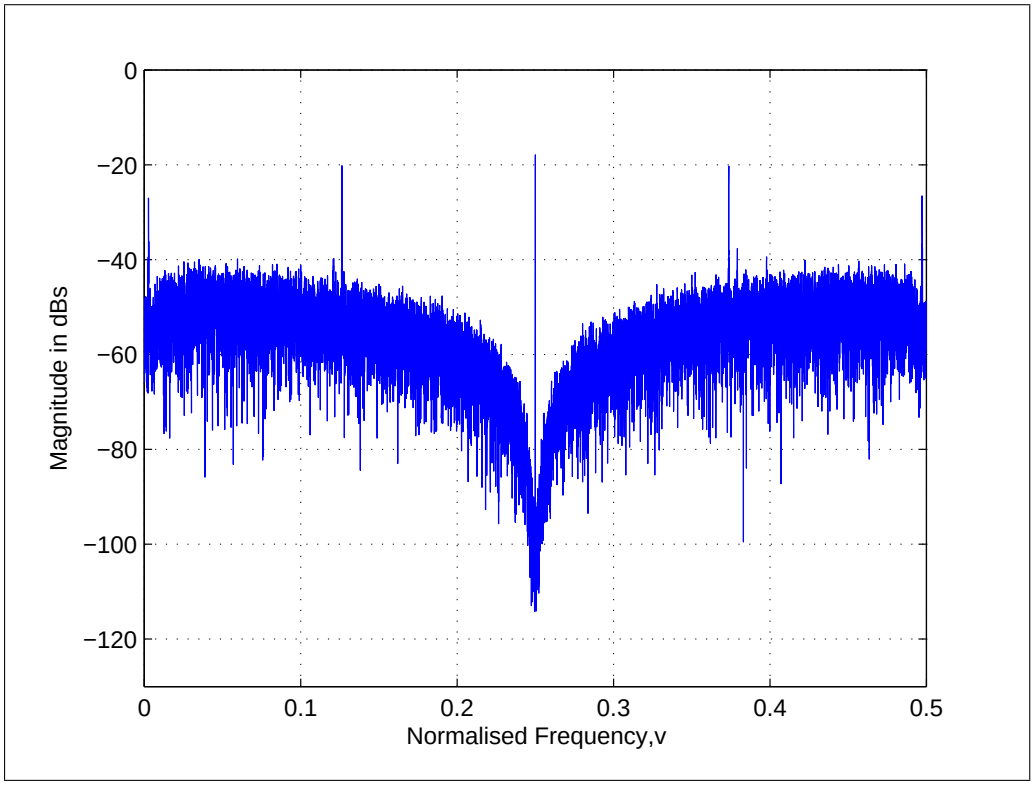

Figure 6.9 The output power spectrum for the 4^{th} order BP $\Sigma - \Delta$ modulator employing weighted feedforward summation with local feedbacks architecture.

For the case of one pair of the integrators, the loop transfer function is obtained;

$$L(z) = \frac{z^2(a_1 + a_2) + a_1}{z^4 + z^2(b_1 + 2) + 1} \tag{6.10}$$

The inverse Chebyshev filters can be implemented to obtain the coefficients. The coefficients can be solved by equating the loop-filter transfer function, $L(z)$ obtained from the NTF to the transfer function obtained from Chebyshev NTF, which can be computed using MATLAB.

For a fourth order modulator, the feedforward coefficients are calculated as $a_1 = -0.0899$ and $a_2 = -0.0042$ and feedback coefficient is $b_1 = 0.0005$. The corresponding modulator is simulated for an input sinusoid of amplitude 0.5 and frequency $\pi/2$ and a dither signal of amplitude 0.01. The simulation result is shown in Figure 6.9. Note that there is a sharp attenuation of quantization noise in the signal-band around 0.25, as expected.

7. A DESIGN, EVALUATION AND MEASUREMENT TOOL FOR $\Sigma - \Delta$ MODULATORS

To speed up the design, analysis, evaluation and measurement of single-loop and multi-stage $\Sigma - \Delta$ modulators explained in the previous chapters, a user-friendly design tool at the system level is developed. This tool allows users to specify the desired parameters in the Graphical User Interface (GUI), simulate the corresponding $\Sigma - \Delta$ modulators for the specified inputs. It then produces the resulting output spectrums, the corresponding NTFs, the histograms of different stage outputs as well as the SNR values and optionally the corresponding modulator structure. The GUI was created using MATLAB and the simulation models were designed in the Simulink environment. The models can be easily developed in Simulink using block formats which can be controlled by MATLAB routines so that it can be used in conjunction with the GUI. The models are already created in the workspace of the MATLAB according to the procedures explained for each type of the $\Sigma - \Delta$ modulator in the Chapters-1-6. The models are navigated by the parameters defined by the user through the GUI and the simulation results are displayed again on the GUI panes. Since the GUI secures the interaction between the user and the simulator, users do not work directly with the Simulink models. Therefore this design tool enables the user easily to edit the design specifications and view the simulation results without dealing with the simulation models.

7.1 The Graphical User Interface

Users just run the lowband.m function and the GUI will start. GUI consists of two parts. In the first part, the user can select either LP or BP $\Sigma - \Delta$ modulation. A screenshot of this part can be seen in Figure 7.1.
In the second part of the GUI, for the chosen type of the modulator, the desired specifications should be edited by the user.

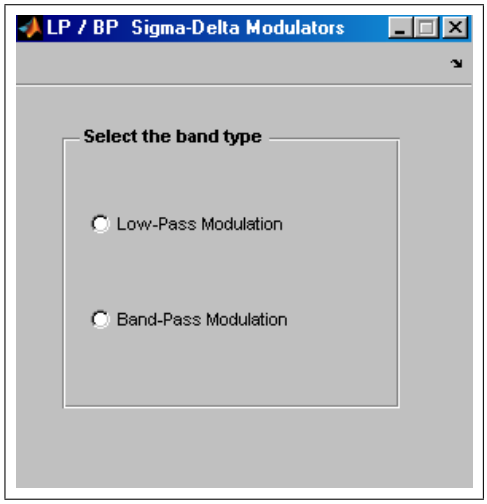

Figure 7.1 Screenshot of the GUI consisting of the options for the LP or BP $\Sigma - \Delta$ modulators.

7.1.1 Input Parameters

The input signal parameters are directly set in the *Parameters* section.
Number of samples: It defines the number of samples in that the program continues simulation. 10000 points are assumed to be transients. Thus, the default value is set to be 42468 which refer to $215 + 10000$ so that the system becomes steady state.
Input amplitude: Since the amplitude is normalized to 1, the amplitude of the input signal must be set to be less than 1.
Input frequency: The input frequency is normalized to a sampling frequency i.e. $\nu = f/f_s$, where f_s is the sampling frequency.
Dither amplitude: The amplitude of the dither can be adjusted for the desired system performance. The default values are already set. However, the user can change the parameters by typing in the edit boxes.

7.1.2 Modulator Specifications

One uses the pop-up menu to select the structure type and the order of the modulator from among a variety of different design architectures: For low-pass modulation; single-loop, multi-stage (MASH), chain of resonators with weighted feedforward

summation, chain of accumulators with feedforward summation and local feedbacks, Butterworth filter response or inverse Chebyshev filter response are the options for the modulator design types. For band-pass modulation; single-loop, chain of resonators with weighted feedforward summation, chain of accumulators with feedforward summation and local feedbacks, Butterworth filter response or Inverse Chebyshev filter response are the selection options.

7.1.3 Display of Results

The plots of the $\Sigma - \Delta$ modulator output spectrums, the corresponding NTFs, the histograms of different stage outputs as well as the SNR values are computed, when the modulator type and order are chosen.
The simulink models are created already in the MATLAB workspace and called via the selection of the user. The MATLAB routines set the user-defined parameters to Simulink models, run the simulation, analyze and give the simulation results.
The power spectral densities are computed using the FFT of the corresponding signals, which are windowed with a Hanning window with the same length as the signal length. The FFT sample number is specified by the user in the parameter section, which is defined as "number of samples". The SNR values are calculated for oversampling ratios (OSR) of 32, 64, 128, and 256, as well as other user defined ones. Moreover, for the power spectrum estimation the Welch's averaging method is used. The associated overlap number is chosen as 2048. The MATLAB routines used to perform the outputs are:
plot.output.m: to plot the output spectrum
snr.lopasshalf.m: to obtain the SNR values of LP $\Sigma-\Delta$ modulators for OSR $32, 64, 128, 256$
snr.band.m: to obtain the SNR values of the BP $\Sigma-\Delta$ modulators for OSR $32, 64, 128, 256$
snr.osr.m: to obtain the SNR value for the desired OSR value
snr.disp.m: to display the calculated SNR values for OSR $32, 64, 128, 256$
snr.osr.disp.m: to display the calculated SNR values for desired OSR value
plot.inputquantizer.m: to plot the input of the quantizer
hist.m: to obtain the histograms for different output stages

plot.NTF_low.m: to plot the NTF for LP $\Sigma - \Delta$ modulators

plot.NTF2.m: to plot the NTF for BP $\Sigma - \Delta$ modulators

pwelch.m: to average the output PSD

bandbutter.cal.m: to calculate the coefficients of the loop-filter for Butterworth filter response for BP $\Sigma - \Delta$ modulators

bandcheby.cal.m: to calculate the coefficients of the loop-filter for Inverse Chebyshev filter response for BP $\Sigma - \Delta$ modulators

butterworth.cal.m: to calculate the coefficients of the loop-filter for Butterworth filter response for LP $\Sigma - \Delta$ modulators

cheby.cal.m: to calculate the coefficients of the loop-filter for Inverse Chebyshev filter response for LP $\Sigma - \Delta$ modulators

save.plot.m: to save the corresponding Figures

The tool can be explained easier through example cases.

7.2 The Graphical User Interface in Operation

7.2.1 Step-by-Step Example-1 (Low-Pass Case)

In this section, the tool is explained through an example for a 3^{rd} order low-pass $\Sigma - \Delta$ modulator using a cascaded (MASH) structure. The specified $\Sigma - \Delta$ modulator is simulated for an input amplitude signal of 0.5, a normalized frequency of 0.01 and a dither amplitude signal of 0.3. The mentioned parameters are directly set in the text-boxes in the *Parameters* section. In the *Structure & Order* Selection Section, the third-order cascaded (MASH)-option is chosen.

When in the Structure & Order Selection section the 3^{rd} order Multistage (MASH) option is chosen as seen in Figure 7.3, the third-order cascaded LP $\Sigma - \Delta$ modulator is called via MATLAB routines and the user-defined parameters are assigned to the Simulink model parameters. The simulations of the histogram of the second-stage output, the $\Sigma - \Delta$ modulator output spectrum and the corresponding SNR values are all shown in Figure 7.3.

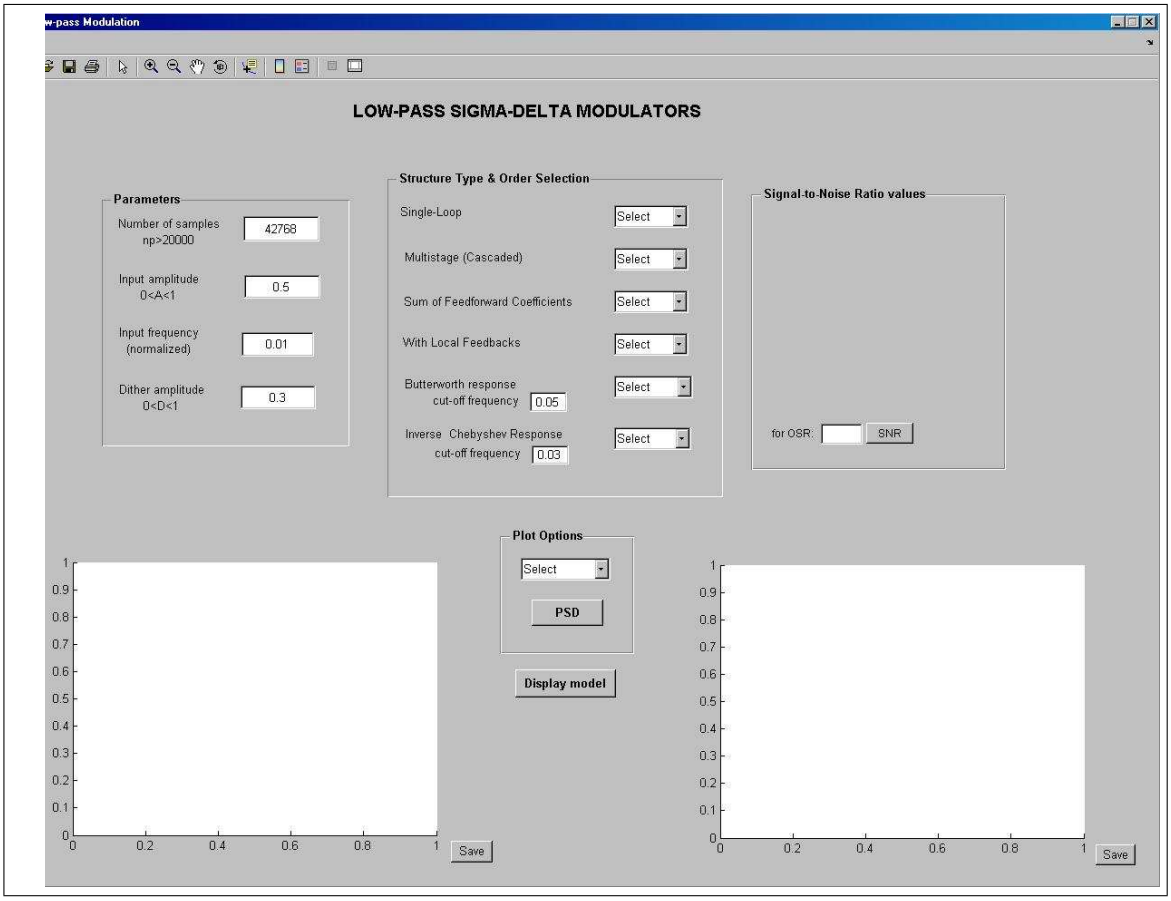

Figure 7.2 The second part of the GUI to specify the input parameters.

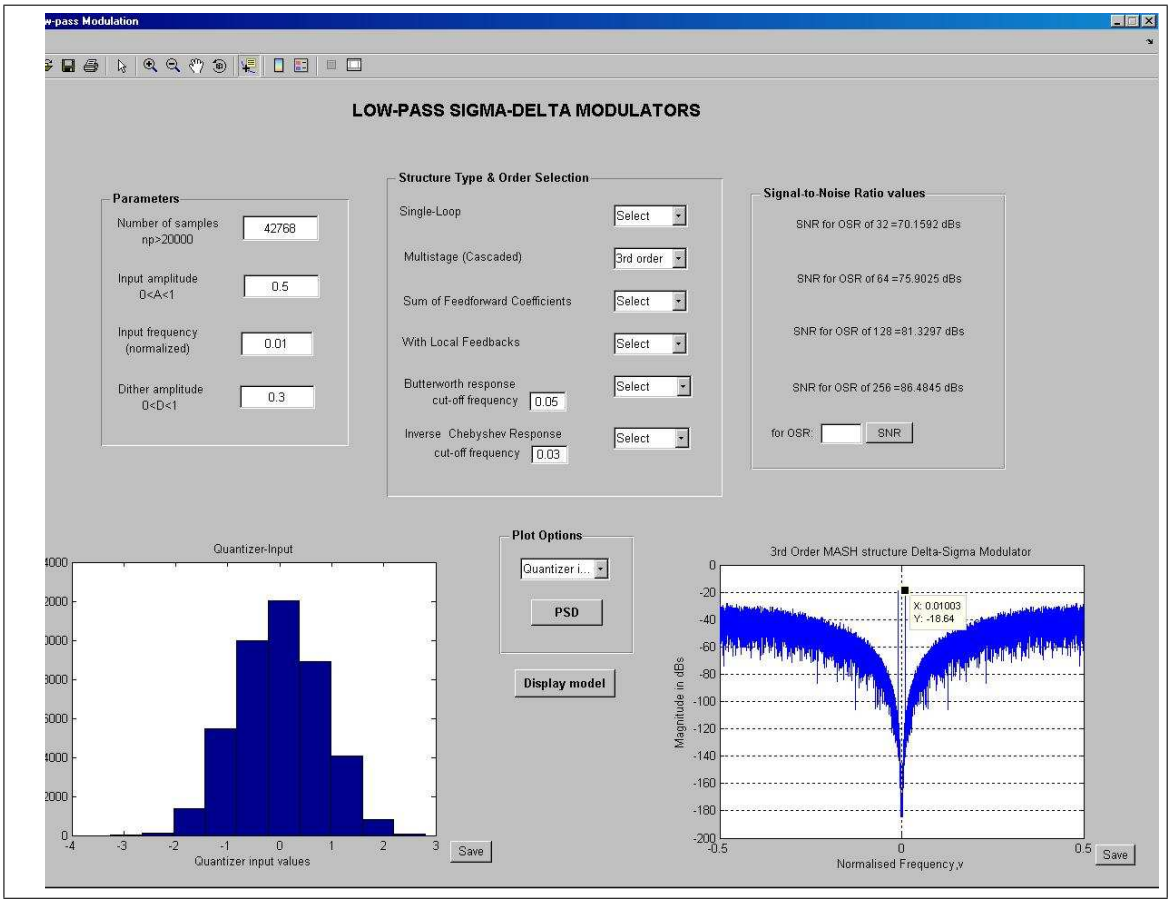

Figure 7.3 The second part of the GUI to specify the structure type and the order of the modulator.

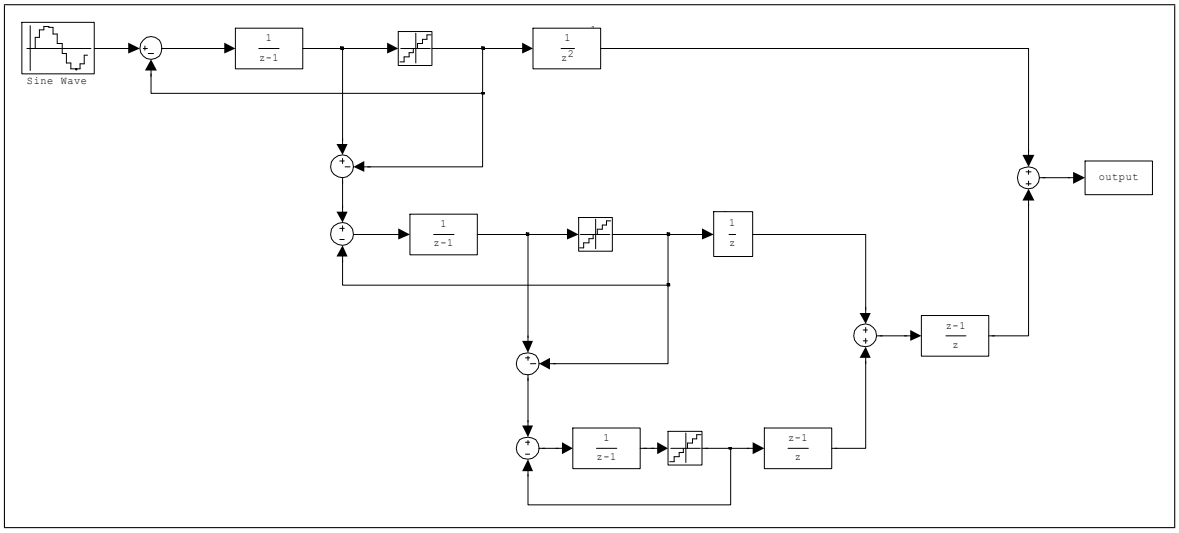

Figure 7.4 A 3^{rd} order LP $\Sigma - \Delta$ modulator using cascaded (MASH) structure.

The output spectrum from Figure 7.3 shows the input signal at the correct frequency (0.01) as well as spectral tones at lower frequencies.

The Simulink model for the 3^{rd} order modulator with variable parameters as shown in Figure 7.4 is already created in the workspace, which is controlled by the GUI specifications. Using the option Display model, the corresponding structure can be seen, as given in Figure 7.4.

As explained in the example case, the user can select the specifications in order to design a variety of single-loop or multi-stage $\Sigma - \Delta$ modulators. In the parameter selection section, default values are entered automatically to guide the user. Different from the single-loop and MASH structures, for Butterworth and Inverse Chebyshev structures, the user can change the filter cut-off frequencies for desired modulator performance. In these cases, the MATLAB routines do not call the specified Simulink models; rather they design automatically the specified models according to the user-defined cut-off frequencies. The programs *butterworth.cal.m* and *cheby.cal.m* calculate and design the Simulink model block parameters for the entered cut-off frequencies for the Butterworth filter and inverse Chebyshev filters. The default values for the cut-off frequencies are already set; however there is no restriction for the frequency ranges. The fifth order low-pass delta sigma modulator using inverse Chebyshev filter response is shown in Figure 7.5. Moreover, using the figure toolbar above the interface, the user

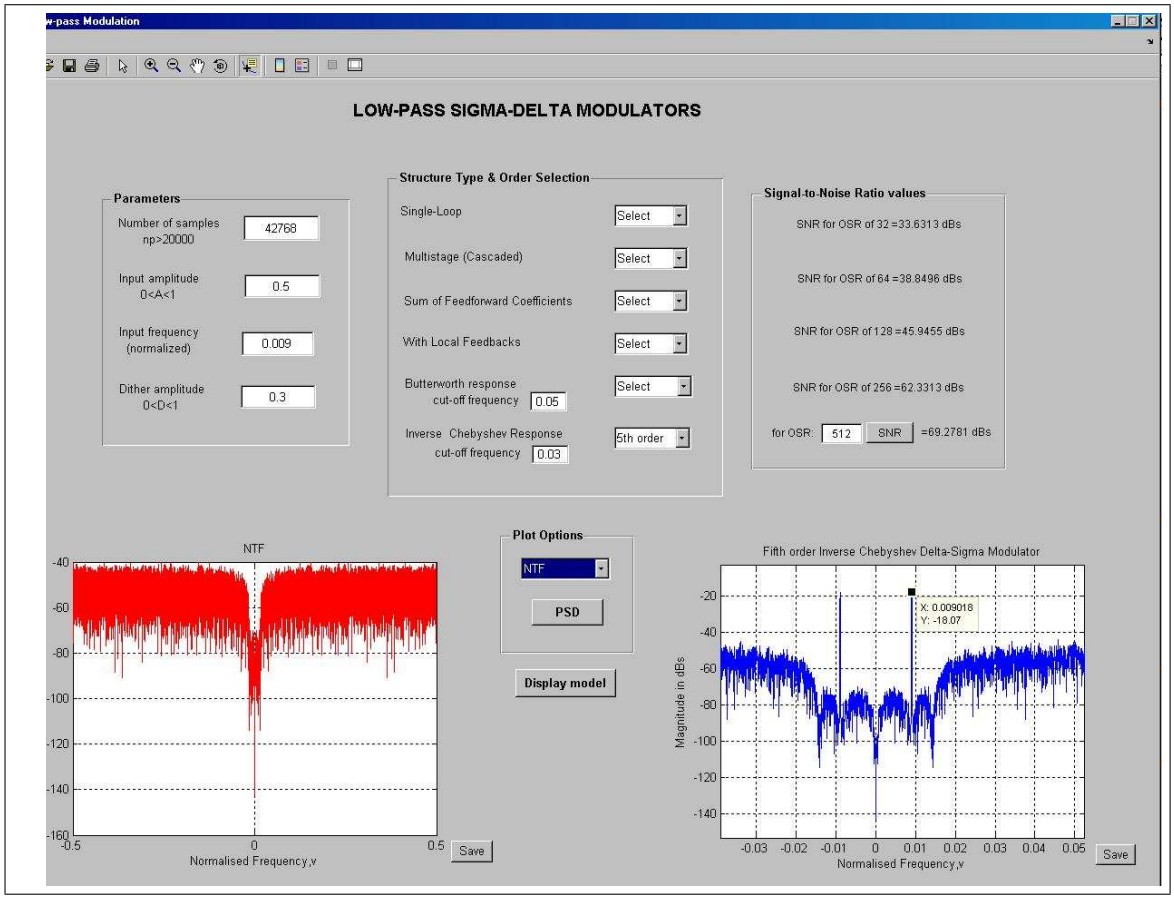

Figure 7.5 Zoomed simulation results displayed in the GUI.

can zoom in the plots in order to analyse the signal band region in more detail. GUI updates instantaneously the quantizer input and the output spectrum plots and the SNR values for each parameter change that the users make to the input signal, therefore the effects of small input changes can be easily observed in the output.

7.2.2 Step-by-Step Example-2 (Band-Pass Case)

As soon as the user selects the band-pass modulation option in the main window (Figure 7.1), the parameter-specification-window for BP $\Sigma-\Delta$ modulators will be displayed. A 6^{th} order mid-band band-pass $\Sigma-\Delta$ modulator using the chain of accumulators structure with weighted feedforward summation was simulated for an input amplitude of 0.5, a normalized input frequency of 0.25, and a dither amplitude signal

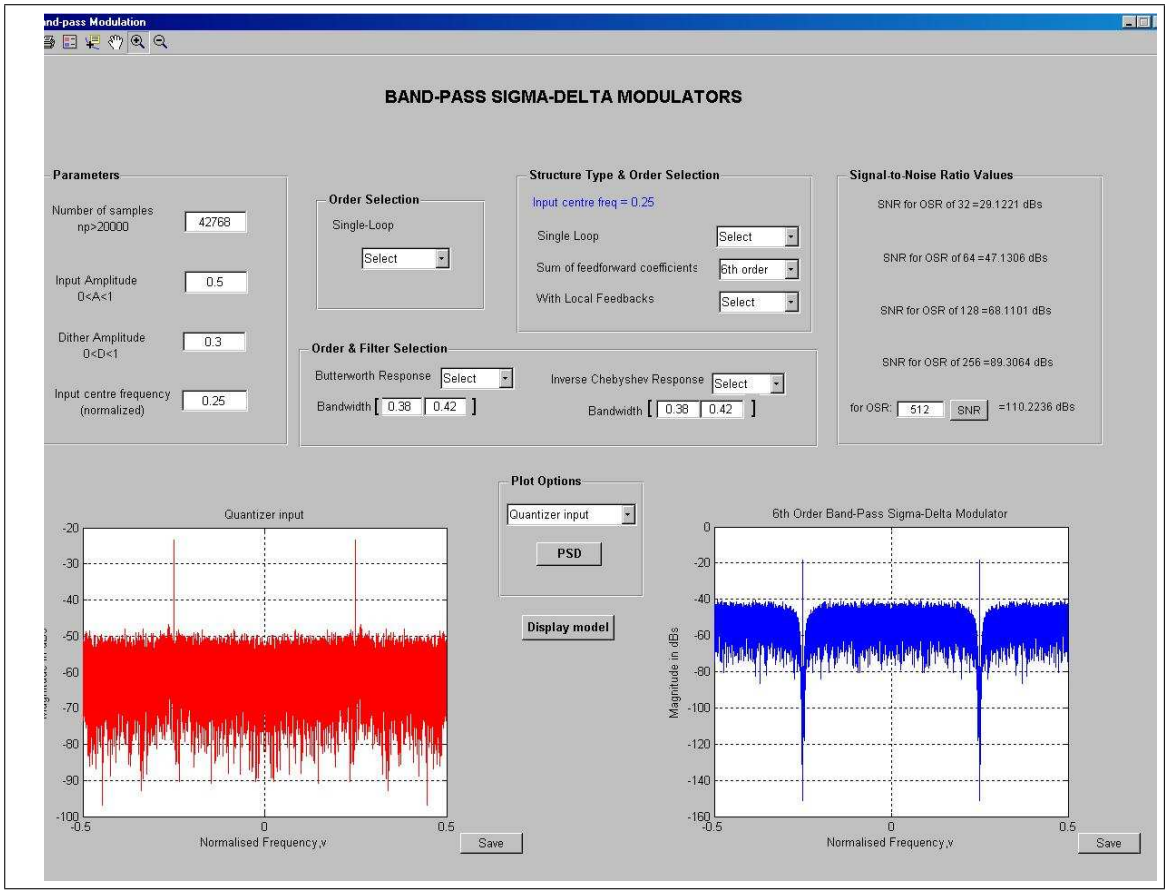

Figure 7.6 Screenshot of the GUI consisting of the input parameters and simulation results for the 6^{th} order BP $\Sigma - \Delta$ modulator.

of 0.1. The NTF and the output spectrum are plotted. The corresponding simulation results are shown in Figure 7.6.

The output spectrum from Figure 7.6 shows the input signal at the correct frequency (0.25) as well as the resulting SNR values for OSRs of 256 and 512 are 98 dB and 122 dB respectively, which shows a good agreement with the reported results in the literature [64].

The corresponding structure of a 6^{th} order BP $\Sigma - \Delta$ modulator is given in Figure 7.7 The coefficients a_1, a_2 and a_3 are calculated as -0.2512, 0.0306 and -0.0018 respectively.

PSD of the output signal is averaged using the Welch's averaged modified periodogram method of spectral estimation with 2048 overlaps. By averaging the output spectrum, the tones can be distinguished so that the $\Sigma - \Delta$ modulators performance can be ana-

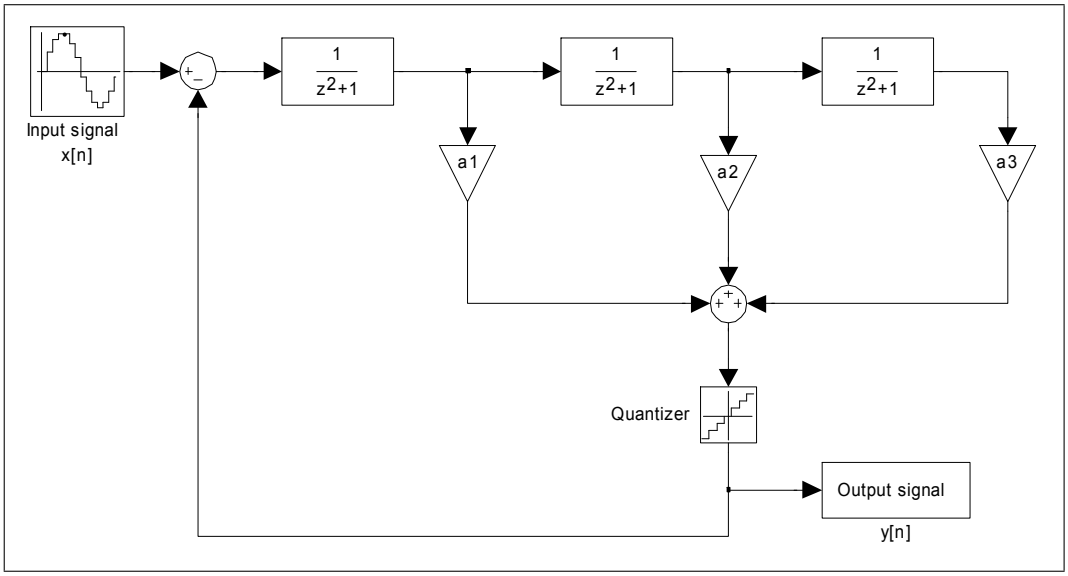

Figure 7.7 A 6^{th} order BP $\Sigma-\Delta$ modulator using chain of accumulators with weighted feedforward summation.

lyzed more effectively. The averaged PSD of the BP $\Sigma-\Delta$ modulator is plotted using the "average" options in the GUI pane, as shown in Figure 7.4

Moreover, the tool allows the user to design the NTFs of Butterworth and Inverse Chebyshev filters based on input specifications such as the cut-off frequency, bandwidth and modulator order. The Butterworth filter or inverse Chebyshev filter responses can be used to design higher order BP $\Sigma-\Delta$ modulators, by adjusting the bandwidth of the filter according to the desired input signal frequency. The lower and upper frequencies of the NTF of the filters are selected so as to ensure that the input signal is positioned at the centre of the signal bandwidth.

Figure 7.9 gives the simulation results for 6^{th} order BP $\Sigma-\Delta$ modulator designed using the Butterworth filter. Since the input normalized frequency is 0.3, the bandwidth is chosen as $[\ 0.58-0.62\ ]$. The center of the bandwidth is twice as the input frequency (0.6), because of the MATLABs routines for NTF calculations. Furthermore, the upper and lower limits of the bandwidth should be chosen symmetric to the centre.

As seen in the examples, users can choose among different modulator structures and sinusoidal input signals. The GUI updates the frequency response of the output signal, the NTF and the output responses of different stages, as well as the SNR values for each alteration that the user makes to the input parameters. Thus, the effects of small

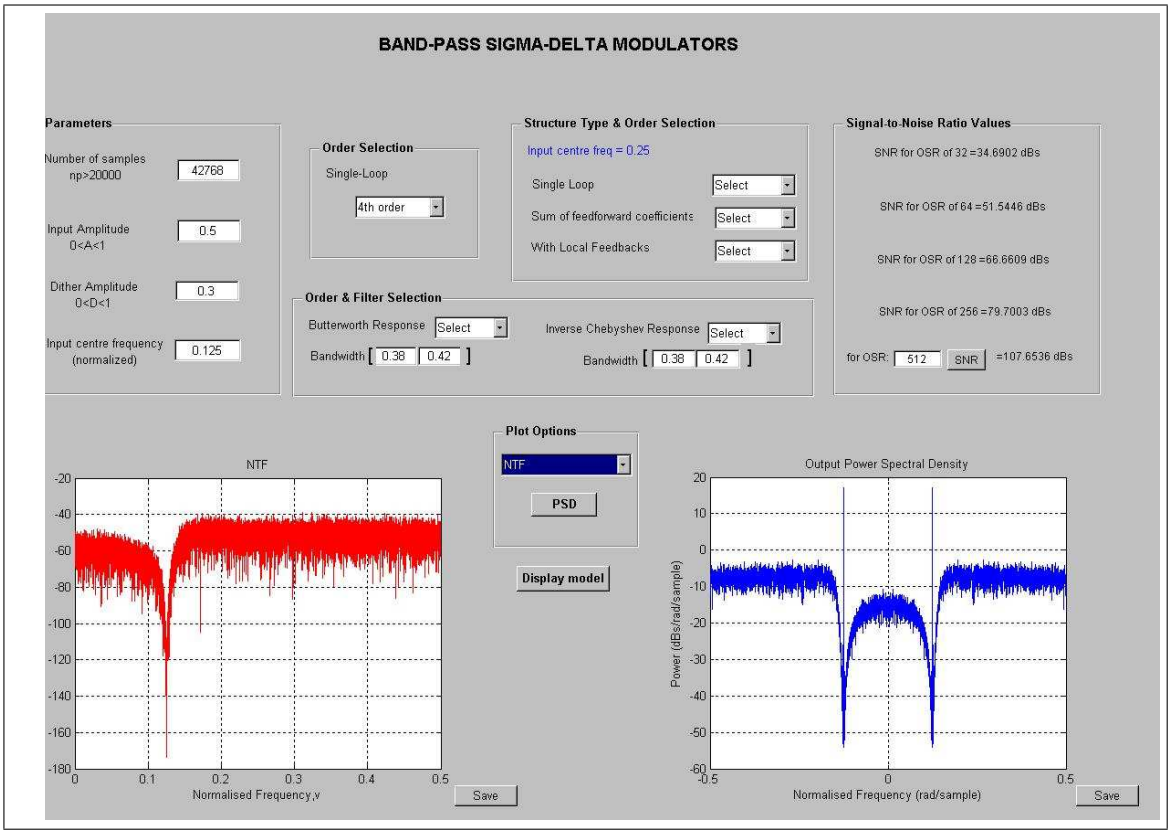

Figure 7.8 A 6^{th} order BP $\Sigma - \Delta$ modulator (with normalized frequency of 0.125) simulation results displayed in GUI.

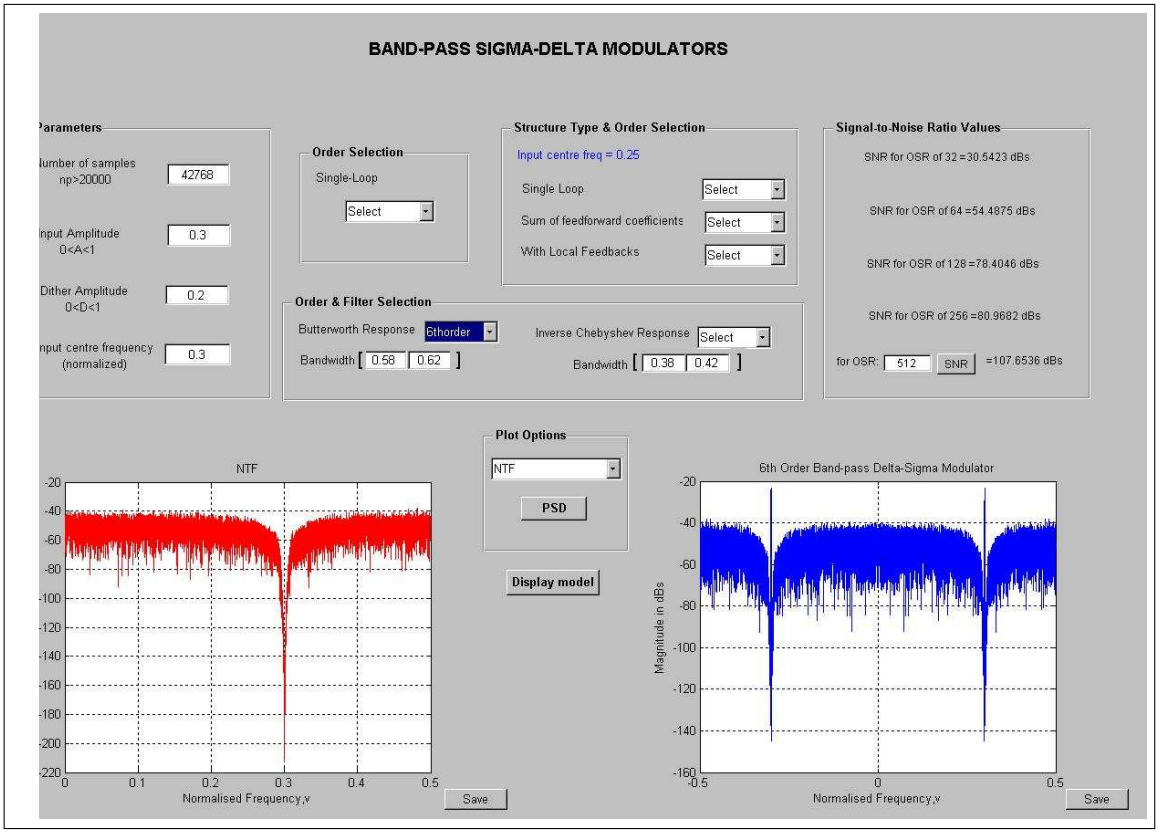

Figure 7.9 A 6^{th} order BP $\Sigma - \Delta$ modulator (with a normalized frequency of 0.3) simulation results displayed in GUI.

input changes can be easily observed in the output. As in the example above, the user can define the specifications in order to design a variety of single-loop or multi-stage LP, and BP $\Sigma - \Delta$ modulators.

8. ULTRASOUND BEAMFORMING IMPLEMENTATION

8.1 Background: Basic Principles of Medical Ultrasound Imaging

Ultrasound imaging, also called ultrasonography is a versatile and widely used medical imaging technique that uses high-frequency sound waves and the echoes, to produce images of the exposed part of the body including the heart, vessels, kidney, liver, developing fetuses and other soft tissues [65]. The performance of digital ultrasound imaging systems is strongly dependent on transducers, front-end components and on how they receive and process the reflected pulses. At this stage the precision of analogue-to-digital conversion becomes critically important. The ultrasound waves are generated by a transducer which is held against the body. The piezoelectric crystal elements in the transducer start to vibrate and produce high-frequency sound waves when a high voltage is applied across the transducer [66]. Ultrasound waves are simply sound waves, which travel through a conducting medium (e.g., body tissue) as a longitudinal wave oscillating back and forth in the direction the sound wave travels, which can be represented as a sinusoidal waveform. Diagnostic ultrasound is in the range of $1 - 15$ MHz, while human hearing is in the 20 Hz-20 KHz range. Different from sound waves, ultrasound waves with high frequencies tend to move more in straight lines, and will be reflected by much smaller objects like light beams and do not propagate easily in gaseous media. The speed of sound varies for different transmission media but the average transmission velocity is assumed to be nearly uniform at $1,540$ m/sec for most soft tissues [66]. Through their propagation, sound-waves are partially reflected and refracted depending on the tissue they are transmitted. When two mediums with different densities are located next to each other, an acoustic impedance mismatch is created and sound waves are reflected by this mismatch. The ultrasound imaging technique is based on processing the received pulse, which is partly reflected from the interfaces between two tissues, and partially transmitted. The greater the acoustic mismatch, the more pulses are reflected and returned to the transducer. Thus, an echo, which is

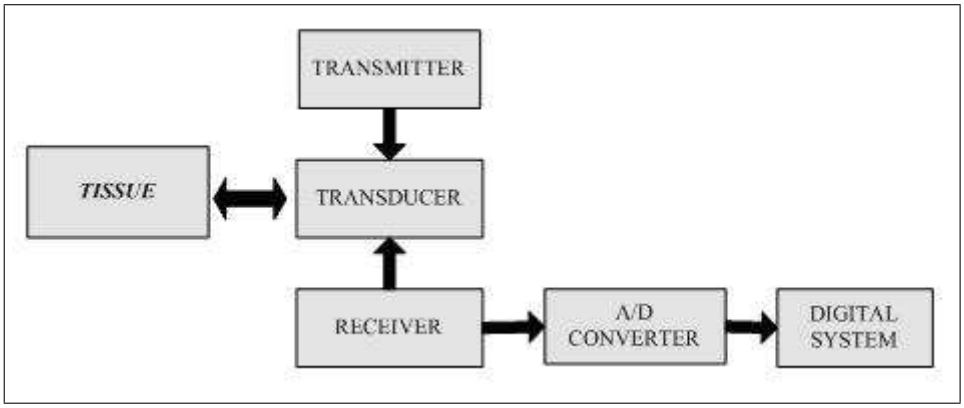

Figure 8.1 Simplified block diagram of the front-end hardware of the ultrasound system.

reflected by tissues with large tissue impedances differences, has large reflection power and generally seen as brighter areas on the image. The transducer is set to wait after the pulse is emitted, in order to receive the reflected pulses, i.e. echoes. The amplitude of the received echo defines the tissue properties in terms of image brightness, where the strong reflections due to the high tissue impedance (e.g. bone, gallstone) are represented as white and no reflections due to the weak tissue impedance (blood, urine) as black. Also, the total time for awaiting the echo is determined by the depth of the tissue. The system calculates how long it takes for the echo to return to the transducer using the relation: $Distance = Velocity * Time/2$. In B-mode imaging, the amplitude is displayed as the brightness of the certain point which is representing the target tissues, in which the image is constructed and displayed on the monitor as a gray-scaled, 2D image. In this study, B-mode implementation is considered.

8.2 Front-end Components of the Digital Ultrasound System

The performance of the digital ultrasound system is critically dependent on the front-end components in order to construct high resolution ultrasound image from received echo signals. The front-end system is summarized in Figure 8.1 below.

The transmitter excites the transducer with a series of pulses. The transducer converts electrical energy from the transmitter into ultrasound pulses sent to the target

tissue. The reflected echoes from tissue are converted back to the electrical signals by the same transducer.

8.3 Beamforming

In order to scan sufficiently wide far field, the beams have to diverge from virtually the same point. In other words, beams should be originated from the same point (focusing). This can be achieved by a single transducer or a transducer array, by focusing the beam patterns. Beam focusing can be performed *mechanically* by placing acoustic lenses on the surface of the transducer. However the common process is beam focusing electronically using *phased arrays*, as used in this study. Transducer arrays can be explained as a single transducer element divided into N-elements, and each element transmits and receives ultrasound pulses differently. The phased arrays typically consist of more than 128 elements.

8.3.1 The Transmitter and Transmitted Beam Focusing

In transmit mode of operation, multiple piezo-electric elements are excited with properly time-delayed pulses and then become sensors to record the reflected sound waves.

Figure 8.3 is used to explain how the time-delay values for each piezo-electric element are calculated. The location of the focal point (P) in this figure is referenced using polar coordinates ($r - \theta$).

Each transducer element is driven with the same pulse waveform. The propagation time, $\tau_n^{'}$ for the n^{th}-element to the focal point (P) can be approximated by the geometry given in Figure 8.3;

$$\tau_n^{'} = \tau^{'}(x_n, r_0, \theta_0) = \frac{r_n - r_0}{c} = -\frac{x_n \sin\theta_0}{c} + \frac{x_n^2 \cos^2\theta_0}{2cr_0}, \tag{8.1}$$

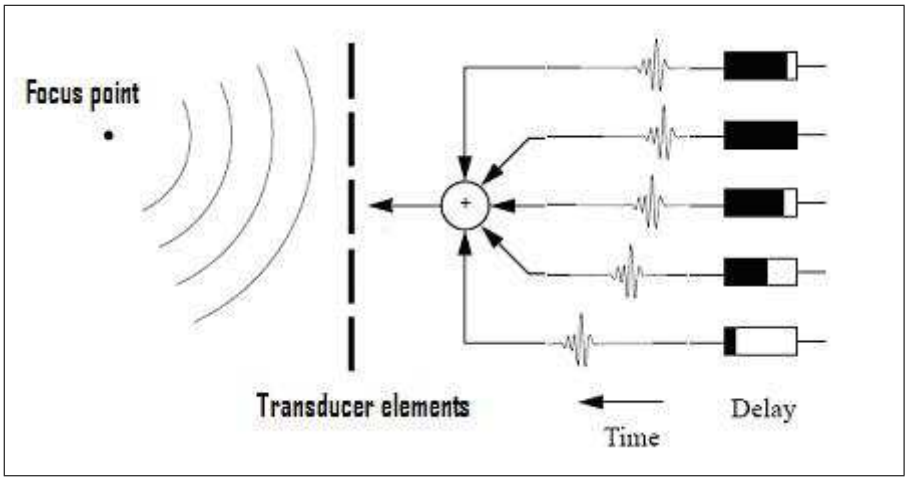

Figure 8.2 Transmit mode array systems.

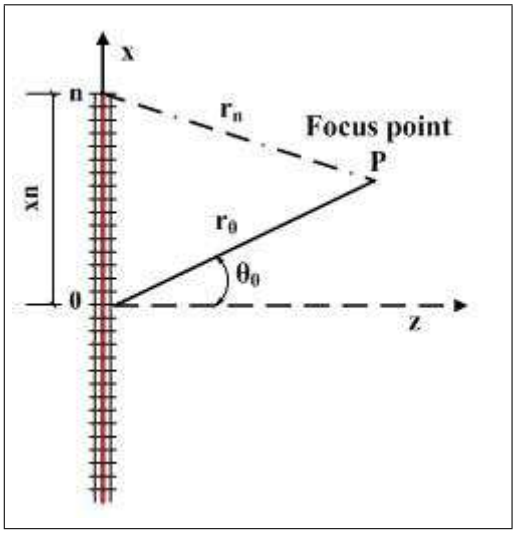

Figure 8.3 Focal point geometry in polar coordinates.

where x_n is the x coordinate of the n^{th}-element, (0 is at the center of the array), θ_0 is the angle to the horizontal axis and r_0 is the depth of the focal point to the center of the array system. Note that, the beams always intersect the array at the center. Usually, in transmit mode, fixed focusing is used. For fixed point focusing the above term yields to ($\theta_0 = 0$);

$$\tau_n^{'} = \tau^{'}(x_n, r_0, \theta_0) = \frac{x_n^2}{2cr_0}. \tag{8.2}$$

To ensure that the sound waves from each element arrive at the focal point at the same time, the pulse waveform to each element must be delayed by this amount to compensate the delay times. This value is used to bias the time-delay values so that the pulse start time for the element that is furthest away from the focal point is time zero.

8.3.2 The Receiver and Beam Forming

Beamforming is defined as the summation of phase-shifted signals that are generated from a common source, but received at different times. Beamformation can performed in two parts: steering and focusing. As seen in Figure 8.4; to receive the echoes with different arriving times, beam is focused by delaying each array elements so that the echoes from the same focal point reach the transducer at the same time.

Since the echoes are reflected from different depth positions, beams should be swept down through the depth range according to the desired position. Therefore, beams have to be deflected in different angles to construct a sector image (steering). The transducer elements have the ability to be dynamically focused by stimulating each element as shown in the Figure 8.5. The individual wave fronts sum up to a beam of ultrasound energy according to the *Huygens principle.*

Therefore receive beamformers employ dynamically focused beam. This can be changed electronically to focus pulses to give sufficient image detail at various depths within the body rather than just one depth as with the fixed focus transducer. Figure

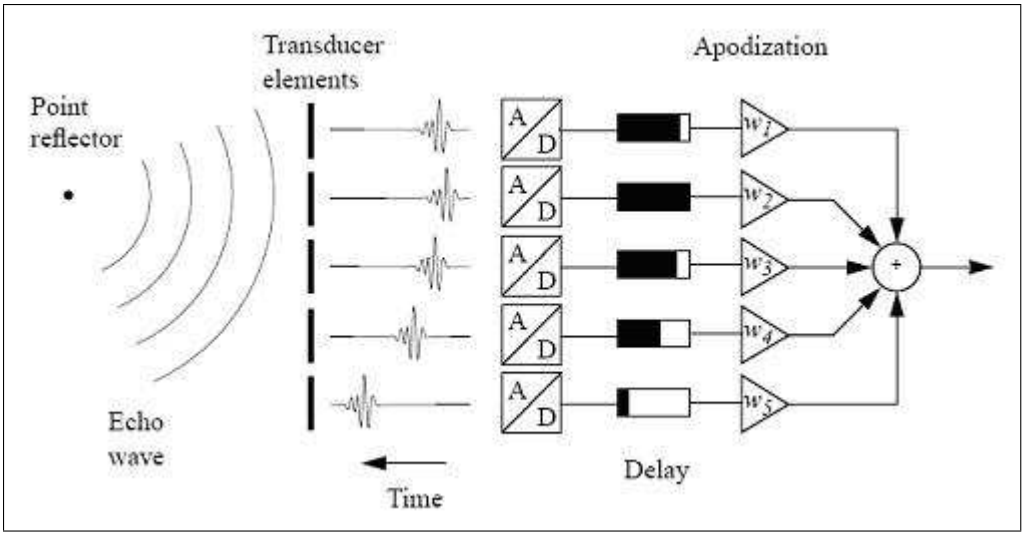

Figure 8.4 Receive mode array system.

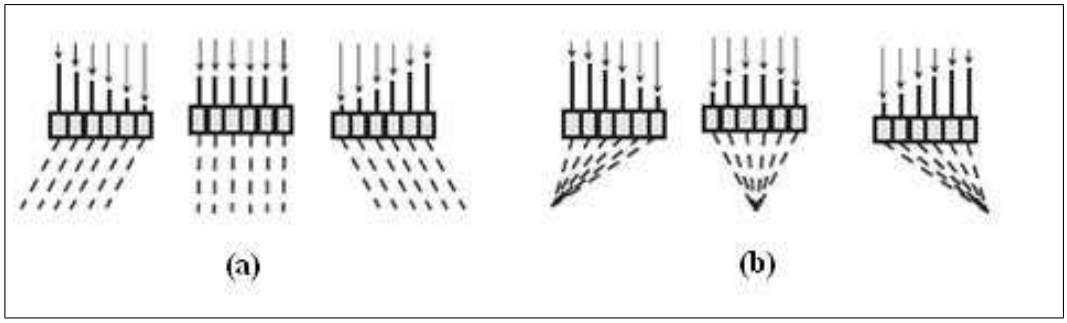

Figure 8.5 (a) Steering (b) Steering and focusing.

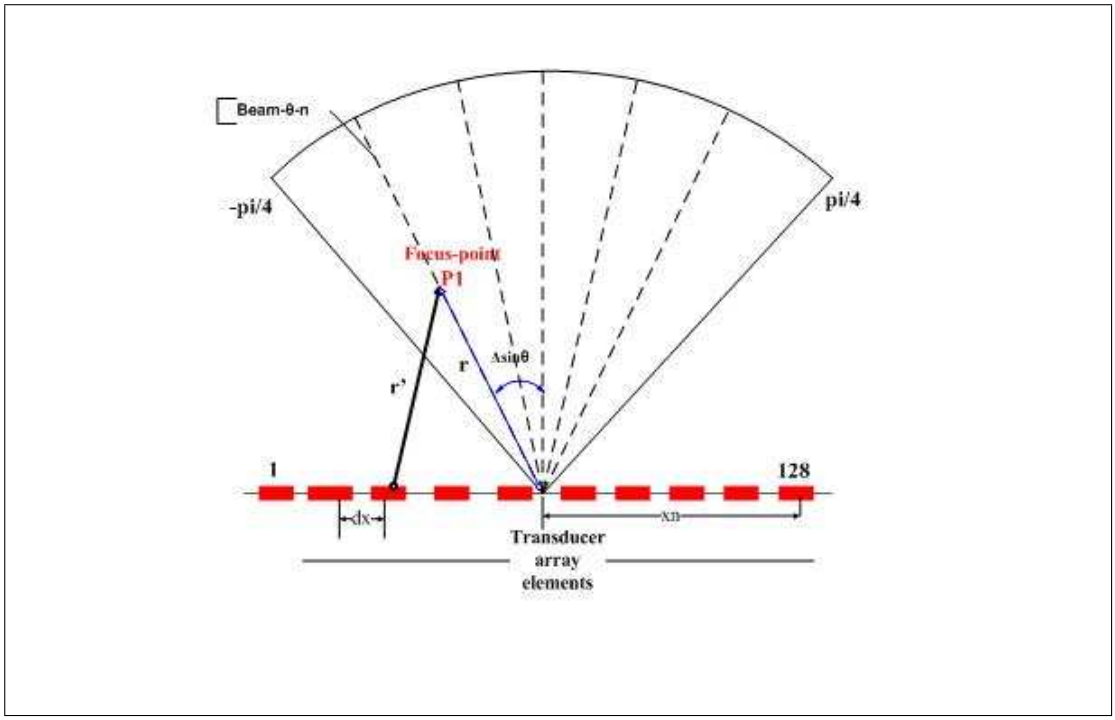

Figure 8.6 Schematic diagram of ultrasound scanning format.

8.6 below, gives the scanning format of the ultrasound imaging system. The delays of corresponding receive element is related to its position to the focus point.

Using the geometry, the general term given in Eq. 8.1 can be separated into two parts as steering and focusing;

$$\tau_n^{'} = \tau^{'}(x_n, r_0, \theta_0) = \underbrace{-\frac{x_n \sin\theta_0}{c}}_{steering-delay} + \underbrace{\frac{x_n^2 \cos^2\theta_0}{2cr_0}}_{focusing-delay} . \tag{8.3}$$

The first term focuses the beam to a particular angle and the second term is to focus to a particular range. The differences in propagation delays from a focus point to each receive element are compensated by time delays in order to maintain a coherent summation. Therefore, the echo signals are delayed by an appropriate amount and added together to form a receive beam. By adjusting the time delays across the array, a region of interest can be scanned over predetermined directions and depth. The echoes are processed by digital receive beamformer and brightness of each pixel in image adjusted as a function of the amplitude of the reflected signals.

In this study, a sector of 90-degree is scanned by B-scan phased array system. In other words, the received waves are steered and focused dynamically as a function of direction and range, by adjusting element delays. To perform a 90-degree scan, there is a angular sampling constraint; minimum spatial sampling frequency should be twice the spatial frequency bandwidth [67]; $\Delta \sin\theta \leq \lambda/4a = 1/2NA$, where $2a$ and NA are the array size and numerical aperture, respectively. Since the sampling is uniform in $\sin\theta$, the sufficient number of beams for a 90-degree scan should be predefined [67];

$$\text{Number of beams} = \frac{\max(\sin\theta) - \min(\sin\theta)}{\Delta \sin\theta}. \tag{8.4}$$

For a conventional 128-element transducer array, number of beams must be greater than 182. In this study, a number of beams is chosen as 200; so that each beam is steered in increments of $\Delta \sin\theta \approx 0.0071$.

8.4 Digital Phased Array Beamforming Implementation

8.4.1 Experimental Data-set

In order to compare images obtained by $\Sigma - \Delta$ beamformer with conventional 10-bit flash ADC beamformers; the experimental data from the Ultrasonic Research Laboratory of the University of Michigan is used. The RF data set is phantom containing six wire targets in a water tank. The experiment setup can be seen in Fig. 8.7, 8.8 The wires are placed slightly away from each other in order to prevent shadowing.

Signals are recorded using 128-element transducer array with an operating frequency of 3.5-MHz. The RF data is sampled at 13.89 MHz over a 120-mm range and digitized using a 10-bit A/D converter. The simulation parameters are given in the Table 8.1.

The RF data-set is obtained as follows: the first transmitter element sends pulse to the target and after a time-offset all the receivers start to record the echo

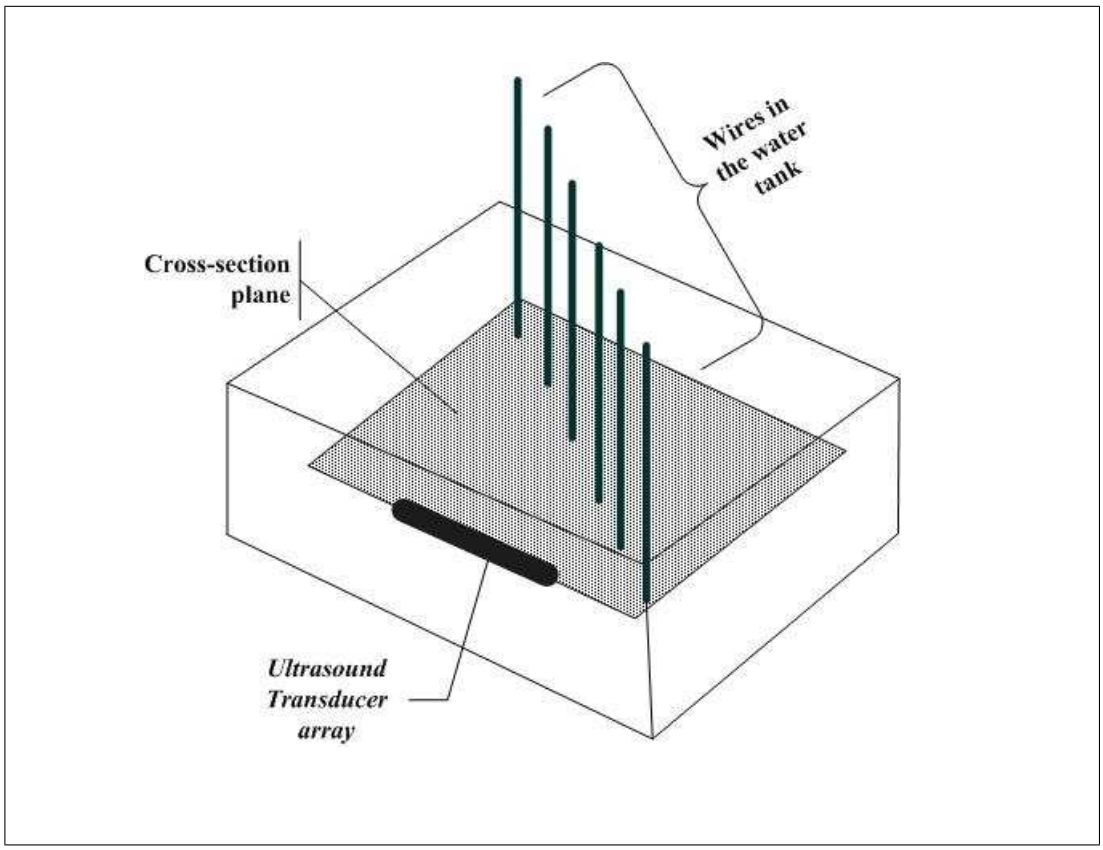

Figure 8.7 Schematic experimental setup.

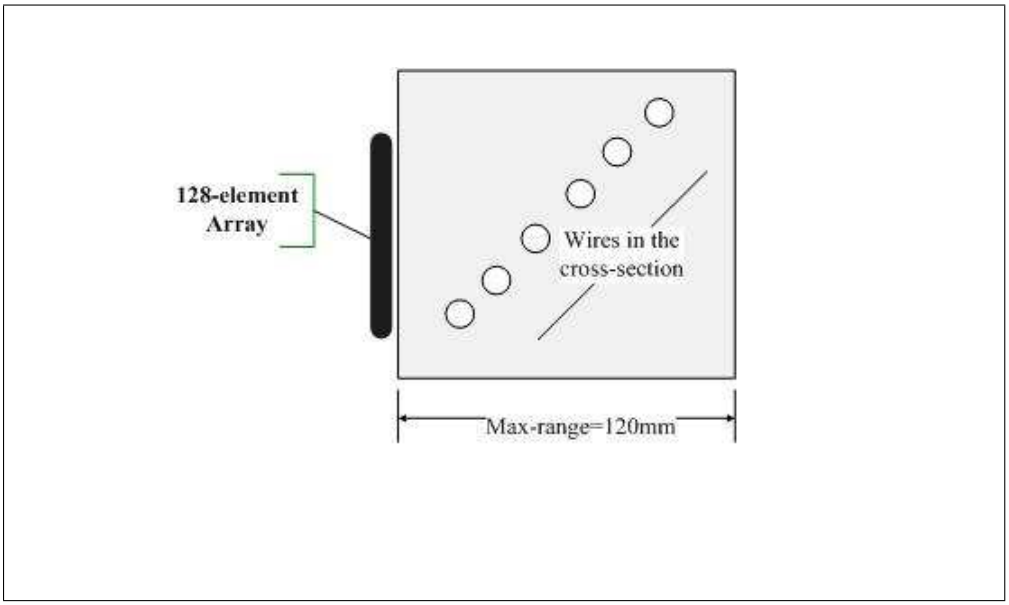

Figure 8.8 Cross-section field of 6-wire phantom.

Table 8.1
Simulation parameters.

Design Parameter	Value
Transducer operating frequency f_o	3.5 MHz
Sampling frequency f_s	13.8889 MHz
Number of channels	128
Transducer spacing	0.22 mm
Image depth	120 mm
Transmit focusing	Fixed focusing
Receive focusing	Dynamic focusing
Image sector	90-degree
Number of beam lines	200
Offset time	29.448 μsec
Speed of sound	1.48 mm/μsec

signals reflected from the targets. After the receive-mode, a second transmitter sends ultrasound pulse and waits the receivers to record. And this procedure continues as the last transmitter sends the pulse and all echoes are received. At the end a data set of a size of $[2048 \times 128 \times 128]$ is obtained. However, through transmission of waves, some portions of the transmitted waves are reflected back to the transducer element whereas some portions continue traveling. To eliminate these echoes during the transmission, a short offset time for receive mode is driven.

Using these data sets, digital beamforming algorithms can be emulated in a software environment. Two reconstruction methods are used: a traditional 10-bit beamformer and a conventional one-bit $\Sigma - \Delta$ beamformer. Fixed focus transmit beamforming was used in both methods (60 mm). After envelope detection and scan conversion, the images are displayed over a 60-dB dynamic range. The image reconstructions from RF data set are performed with MATLAB routines.

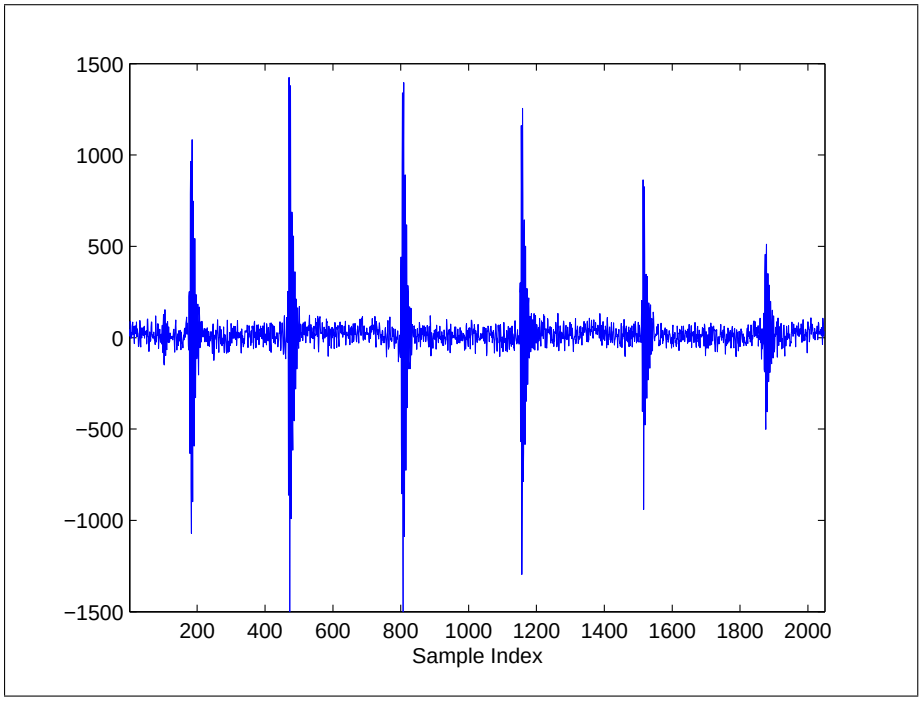

Figure 8.9 RF signal of 2048 samples from 3.5 MHz transducer insonifying wire phantom.

8.4.2 Beamforming Using Conventional Multi-bit A/D Converters

The incoming RF signals are digitized using 10-bit flash ADC's (Figure 8.9), delayed and summed to form the focus of interest as discussed before.

Because of the $1/r$ dependency of the delay term (Eq. 8.3), the delay accuracy should be 1/32 of the wavelength for accurate focus point [68]. Since the sampling rate is four times the operating frequency, the delay accuracy can not be maintained. Therefore, the sampling frequency is increased by an amount of 16; therefore the incoming RF signals (Figure 8.9) are interpolated through zero padding and different interpolation filters at each channel. The frequency-domain analyses for these steps can be seen in Figures 8.10 - 8.12.

The digitized RF-signals are upsampled to 16 times the Nyquist-rate through padding 15-zeros between each sample. The spectrum of the upsampled signal is shown below.

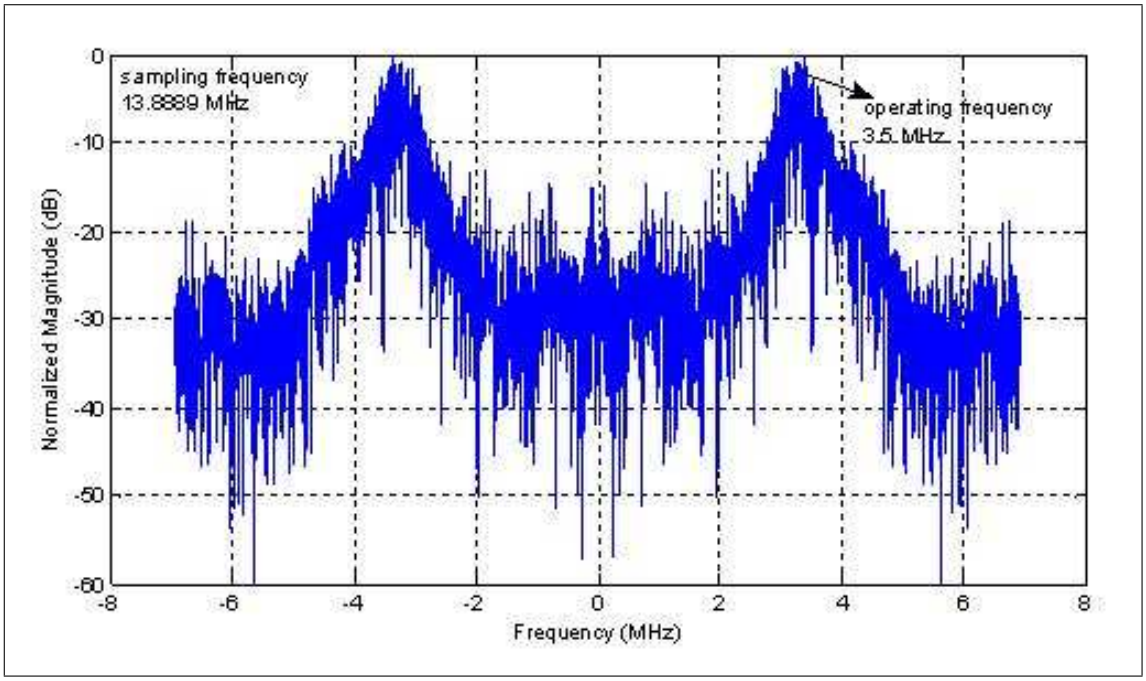

Figure 8.10 Frequency spectrum of the RF echo signal sampled at the Nyquist-rate.

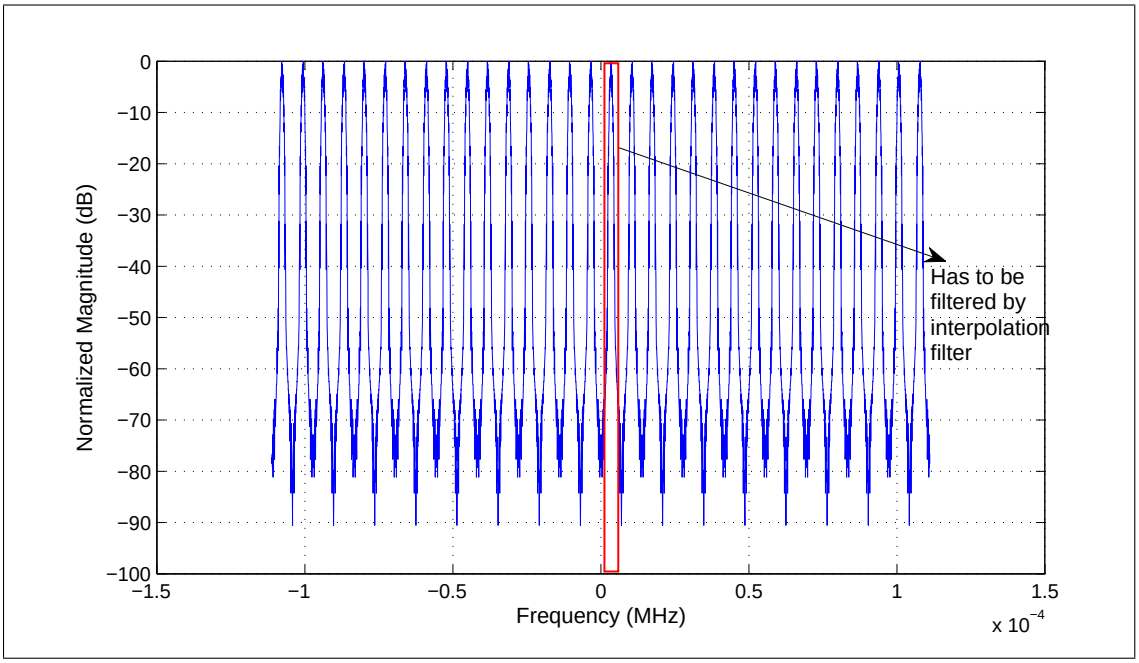

Figure 8.11 Sampling rate is increased to 16 times the Nyquist rate.

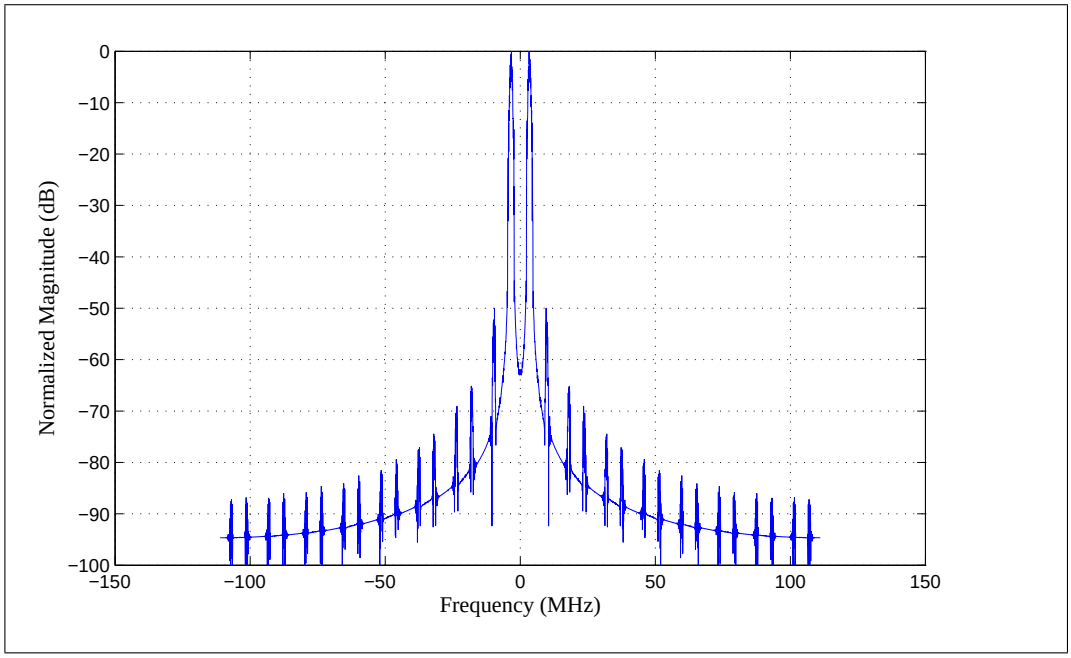

Figure 8.12 Frequency spectrum of the signal after interpolation filter.

Upsampled signals are then interpolated using sinc-interpolation filters as seen in the Figure 8.12. Almost -50 dB reduction of noise will provide an image with a better resolution.

Time- domain representation of the signal can be seen in Figure 8.14. The number of samples (Figure 8.9) is increased by 16 times so that the sample number becomes 32768 before transmit focusing (Figure 8.15). The 16 times-reduced intersampling period provides the sufficient delay accuracy for focusing.

Before the receive beamforming part, *transmit focusing* is performed; i.e. echo signals from 128-transmit elements have to be aligned by compensating the differences in propagation times by means of sample delays. Transmit focus is chosen at the half of the maximum image range, which is 60 mm [68]. Since the pulses from different transmitter elements do not arrive at the point of 60 mm at the same time; echo signals should be delayed appropriately according to the time differences related to the transmitter position. As a result; coherent interference occurs at a fixed distance from the transducer. The amount of each transmit delay are calculated using the relation given in the Eq. 8.1. The wave fronts for the 1^{st} receive element before and after

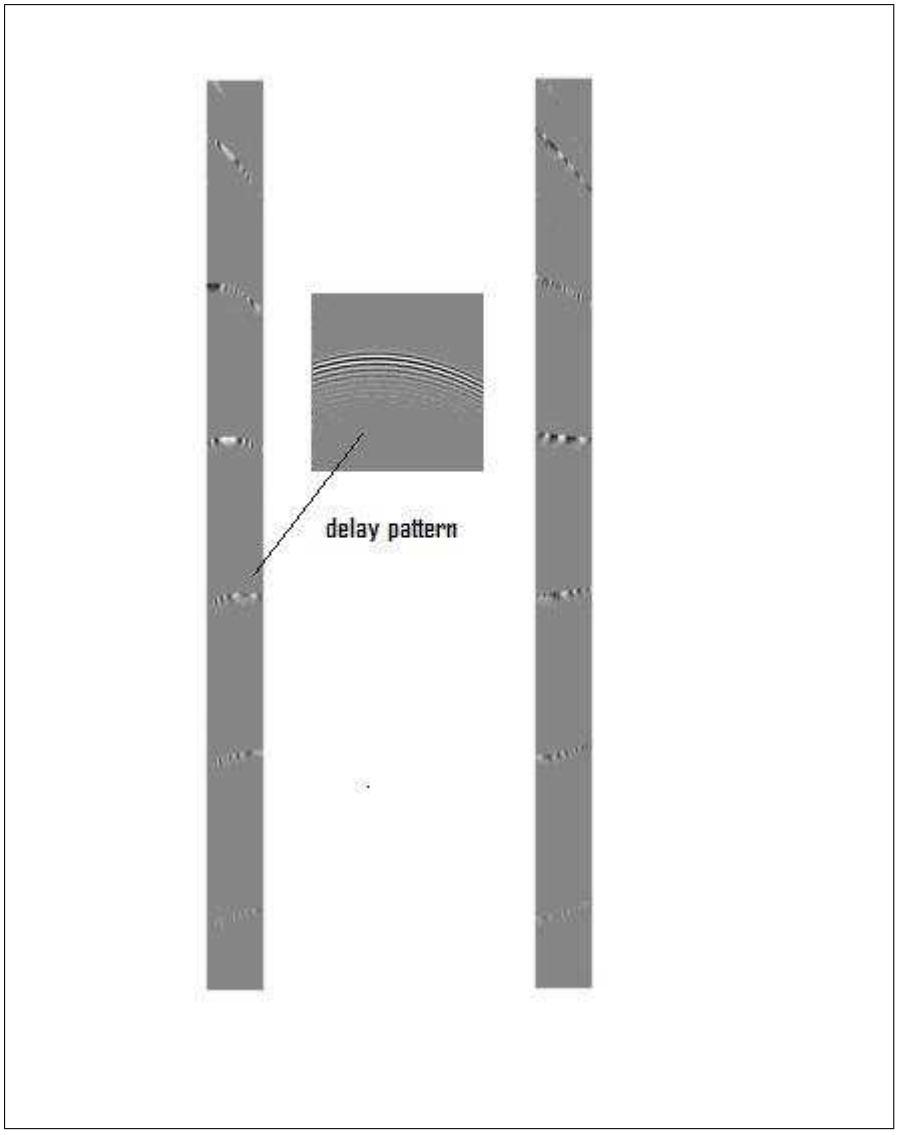

Figure 8.13 Wave-field of the 1^{st} receivers data obtained from all 128 transmit elements.

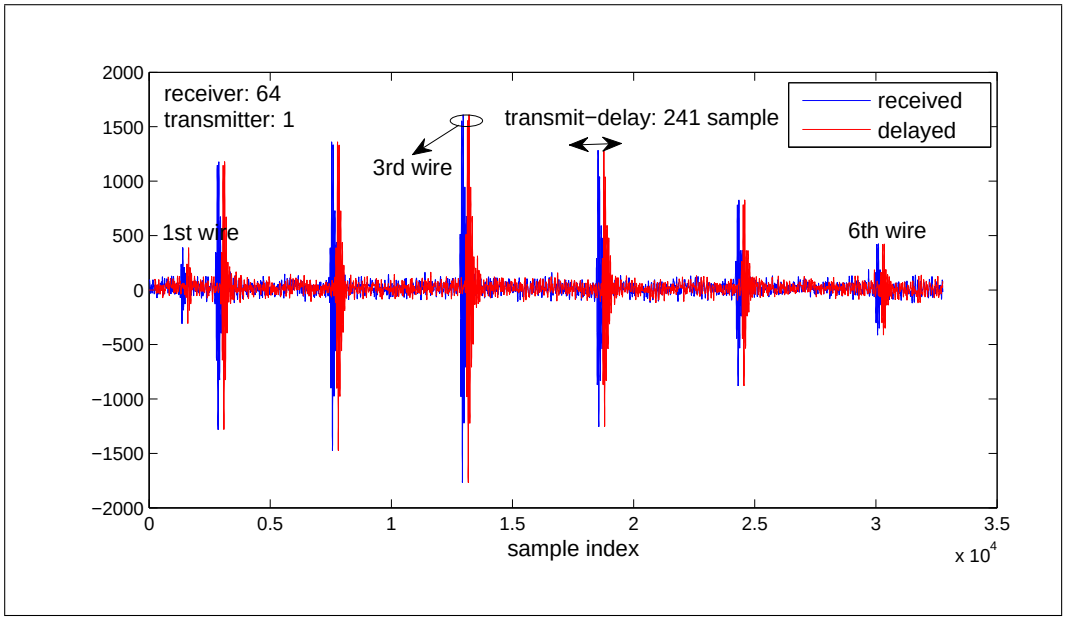

Figure 8.14 Signal received by the 64^{th} element transmitted by 1^{st} element, original signal and delayed signal.

transmit focusing are shown in the Figure 8.13: The delay patterns can be seen in the Figure 8.13(a). The effects of the transmit focusing can be seen in the Figure 8.13(b), after transmit focusing; the pattern are aligned so that their shape become more horizontal instead of arc-shape, especially for the 3^{rd} wire, which is near to the transmit focus. In other words, during transmission, signals of each element in the array are delayed so that a coherent interference occurs at the transmit focus. A signal transmitted by the 1^{st} element and received by the 64^{th} element is delayed by as much time as the time propagation difference of the first element at the focus.

After transmit focusing; aligned signals are summed so that most of the transmit delay effects are eliminated and coherent summation occur at the fixed transmit focus at 60 mm. Thus; after summation; the size of the data $[2048 \times 128 \times 128]$ becomes $[32768 \times 128]$ before receive beam-forming. The summed signals for the 1^{st}, 64^{th} and 128^{th} elements are shown in Figure 8.15. The propagation time differences for each element after transmit focusing, are compensated in the receive-focusing part.

The wavefronts of the RF signals received by the 1st and 64^{th} elements before transmit focusing and the resulting wavefronts after the coherent summation across the

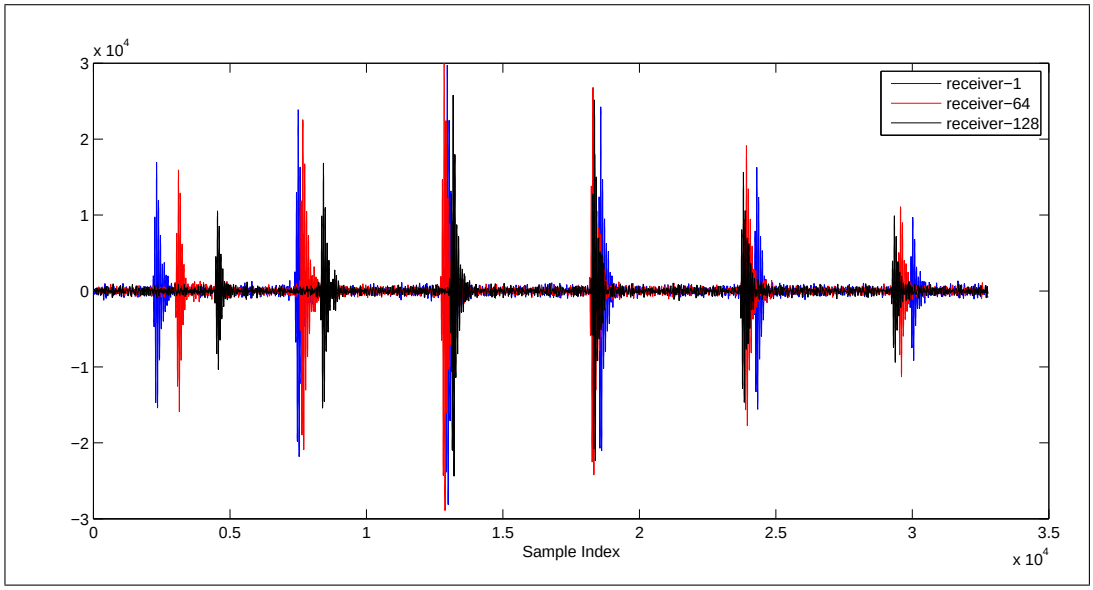

Figure 8.15 Echo signals of the 1^{st}, 64^{th} and 128^{th} receive elements after transmit-delays.

array after the transmit focusing are given in the Figure 8.16 below. The corresponding delay patterns in the wavefronts can be observed.

On the *receive-focusing*; dynamic (changing) delays to each element are applied so that coherent summation across the array produces a focus at many points along a particular angle. In other words; each sample is delayed appropriately and added to each other, to form the desired beam at a particular direction and produce a signal localized to the focal point (r_0, θ_0). As a result, an image line is produced by continuously focusing along that beam line [69].

$$v(t) = \sum_{i=1}^{1} 28 v_n(t + \tau_n^{'}). \tag{8.5}$$

Here, the receive signal at time t corresponds to depth $r = tc/2$. At each point t it is needed a new focal depth, r. A different set of delays for each depth (time sample) is applied; so that at each focus point the delay set is changed. Changing the delays on receive allows the system to change the direction of the beam and scan a sector of 90-degree. When all 200 beams are completed, the image can be constructed. Since the delayed and summed signals are at the sampling rate of 222.2224 MHz, the decimation should be performed to downsample the signals to the Nyquist sampling rate. The

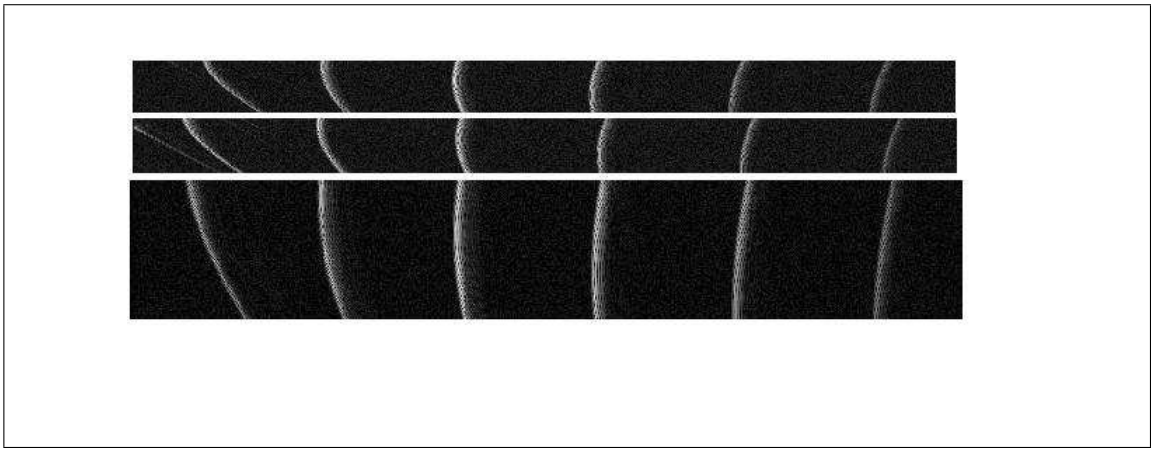

Figure 8.16 First two: 1^{st} and 64^{th} receive elements unfocused, third: total echo signals after transmit focusing.

envelope of the signal is obtained as the magnitude of the sum of its in-phase and quadrature components. The envelope is then compressed logarithmically to 60 dB. After the processes of *envelope detection* and *logarithmic compression* the image with a dynamic range of 60 dB in polar coordinates is obtained.

The final process is the *scan conversion* to present the data as an image in cartesian coordinates. This involves conversion from beam data in polar coordinates, which exists in a domain that is equally spaced in $\sin\theta$ and in r, to physical space, which is a domain that is equally spaced in x and y. The constructed image after scan conversion can be seen in the Figure 8.22(a).

8.4.3 Beamforming Using Single-Bit $\Sigma - \Delta$ A/D Converters

The complexity, size and power consumption of traditional beamformers can be dramatically reduced by using single bit $\Sigma - \Delta$ beamformers [68]. In this part of the study, digital beamforming with a low-pass second order $\Sigma - \Delta$ converters are implemented, and their advantages and disadvantages are examined. The corresponding 2^{nd} order $\Sigma - \Delta$ modulator structure given in Figure 8.18 is used to digitize the incoming RF signals. The system analysis gives that;

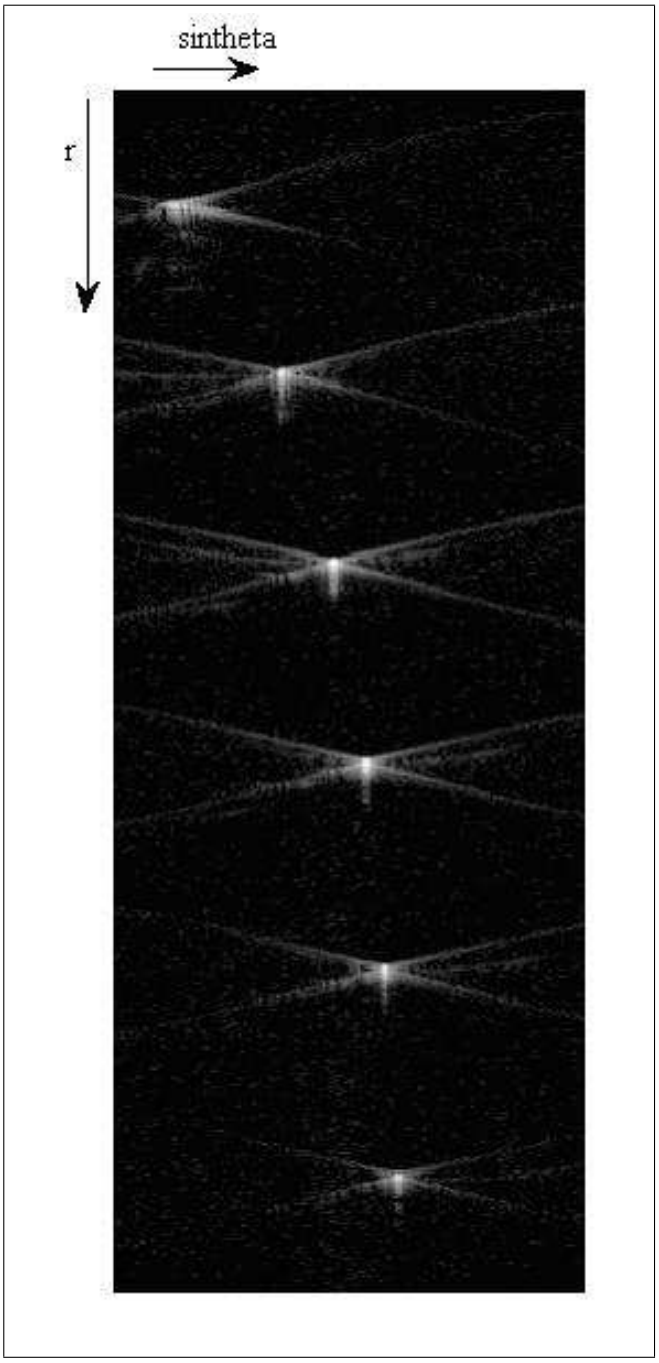

Figure 8.17 Image in polar coordinates ($r - sintheta$).

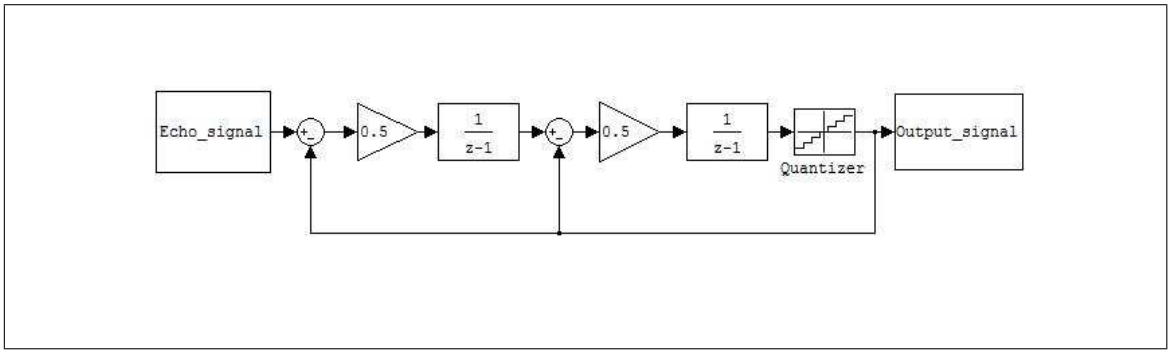

Figure 8.18 Block diagram of a 2^{nd} order low-pass $\Sigma - \Delta$ modulator.

$$Y(Z) = X(z)z^{-1} + E(z)(1 - z^{-1}). \tag{8.6}$$

$Y(z)$, $X(z)$ and $E(z)$ are output signal, input signal and quantization noise signal, respectively. Suppressed quantization noise due to the high-pass NTF is the most important factor of the success of the $\Sigma - \Delta$ modulators. The reduced noise in the signal band provides a high SNR value in the signal band compared to the traditional A/D converters. As explained previously, the quantization noise power, e^2_{rms} of a traditional multi-bit A/D converters is assumed uniformly distributed white noise: $\sigma_e^2 = \Delta^2/12$, where Δ is the quantization noise interval.The noise-shaping with the effect of the OSR, the quantization noise in the signal-band is reduced to approximately;

$$\sigma^2_{ey} = \sigma_e^2 \frac{\pi^4}{5} \underbrace{\left(\frac{2f_B}{f_s}\right)^5}_{OSR}. \tag{8.7}$$

Suppressed noise in the signal band; cause the SNR value to increase [26];

$$SNR = 10\log_{10}\left(\frac{\sigma_x^2}{\sigma_e^2}\right) - 1.29 + 50\log_{10}\underbrace{\left(\frac{f_s}{2f_B}\right)}_{OSR} \quad \text{dB}. \tag{8.8}$$

That gives an extra 15.05 or 2.5 equivalent bits for every doubling of overdsampling ratio (OSR = oversampling frequency/Nyquist sampling frequency). Therefore, to obtain a 10-bits equivalent resolution using a 1-bit second-order $\Sigma - \Delta$ modulator OSR should be 16. Thus, a oversampling frequency of 16 times the Nyquist sampling frequency (13.8889 MHz) is required. As a result the RF signals are modulated with

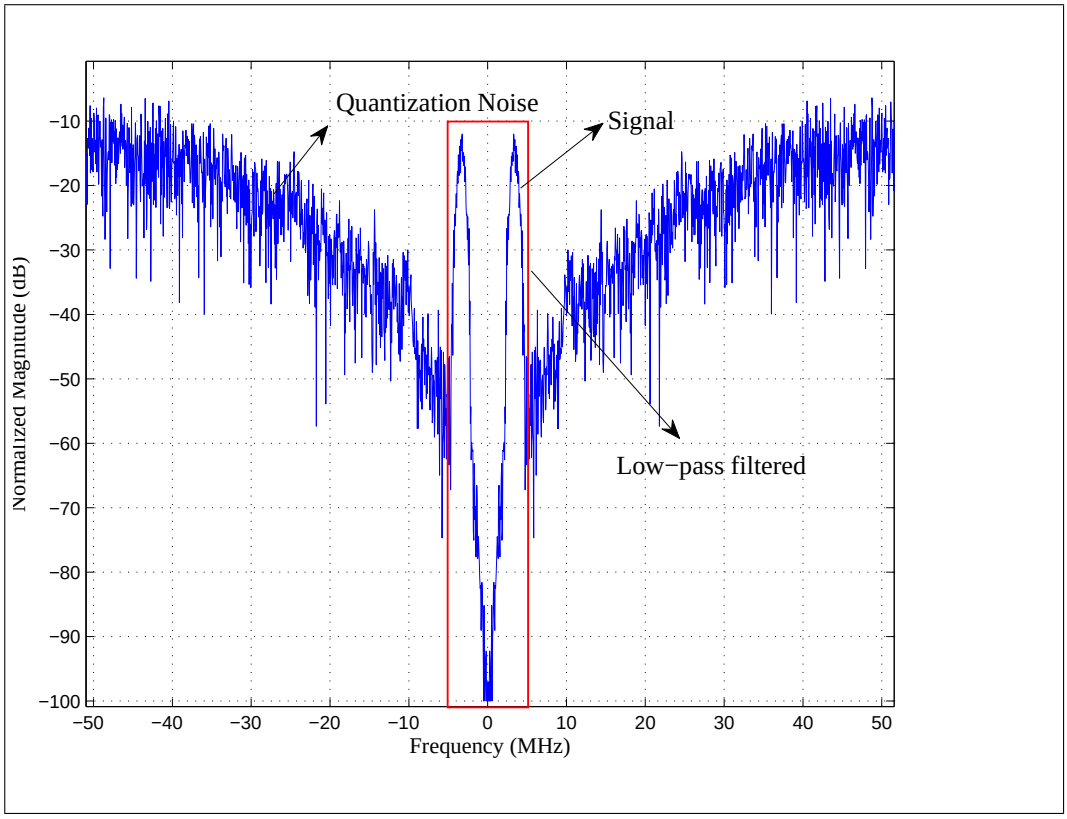

Figure 8.19 Frequency spectrum of the signal modulated with 2^{nd} order low-pass $\Sigma - \Delta$ modulator.

a sampling rate of 222.2224 MHz.

Since the modulator pushes the quantization noise to the higher frequencies and suppresses the noise in the signal band, removing the out-of-band quantization noise with a low-pass filter is equivalent to increasing the effective resolution of the digital output [26]. The 3^{rd}-order comb filter is equivalent to the moving average over the digital data; so that the 10-bits equivalent output can be obtained [69].

Before the decimation process image in polar coordinates can be constructed as shown in Figure 8.20. However the size of the data to be imaged is $[32768 \times 201]$, which makes the scan conversion process difficult and time consuming (MATLAB processes the data 28 hours for the scan conversion). In addition, there isn't any significant difference between the SNR values of the images before and after the decimation process. (without decimation process 42 dB, after decimation process 41.8 dB)

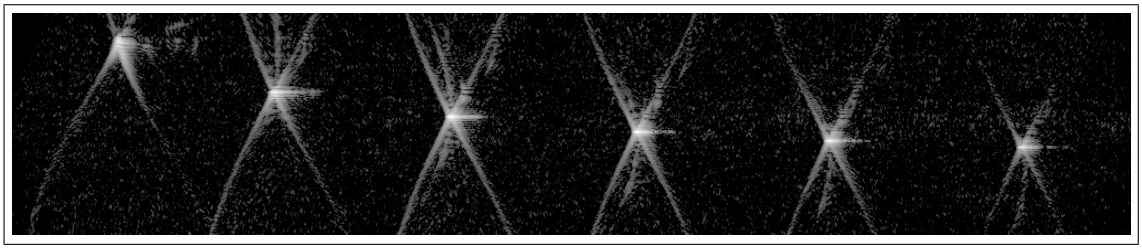

Figure 8.20 Image in polar coordinates before decimation process ($r - sintheta$).

In order to have a meaningful image, the high sampling rate should be down sampled to the Nyquist-sampling rate. However, dynamic focusing in receive mode; repeating/dropping samples degrade the synchronization between the modulator and demodulator so that the noise-shaping disturbed and some parts of the quantization noise folded to the signal band, which increases the background noise level and causes artifacts in the image (Figure 8.21). The delay calculations, the envelope detection and logarithmic compression parts are the same as done in the conventional beamformers. The constructed image compressed to 50 dB in polar coordinates is given in Figure 8.21.

After scan conversion from polar coordinates to Cartesian coordinates, the final image is constructed (Figure 8.22(b)).

8.4.4 Simulation Results and Discussion

The $\Sigma - \Delta$ beamformers offer crucial benefits in system design over traditional multi-bit A/D beamformers:

- ✓ The most important advantage of $\Sigma - \Delta$ beamformers is reducing the front-end hardware complexity and the saving of cost, size and power consumption [68, 69].
- ✓ The delay accuracy can be maintained by the inherently high sampling rate of $\Sigma - \Delta$ modulators. Therefore, the complicated interpolation process used by 10-bit ADC to secure the delay accuracy is eliminated. The speed and size of the

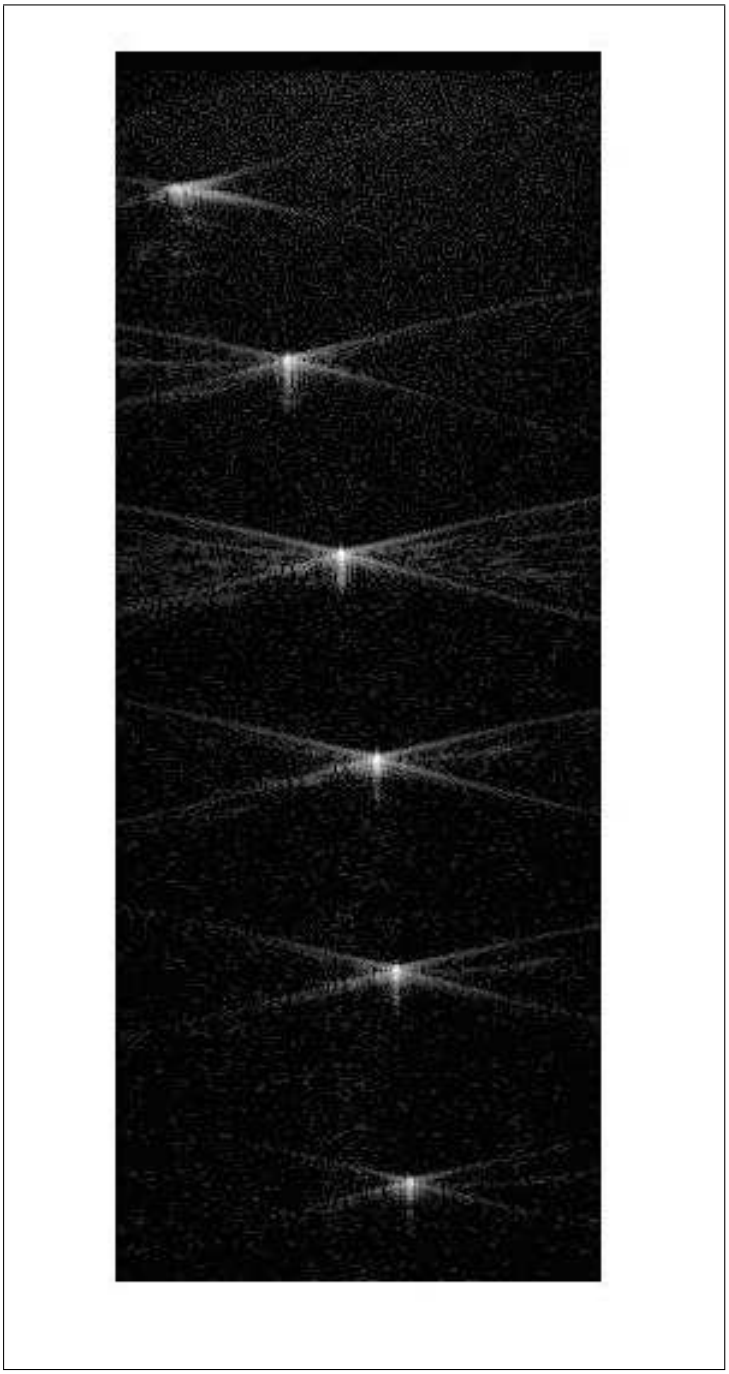

Figure 8.21 Image in polar coordinates ($r - sintheta$).

hardware is reduced due to the simplified signal processing and reduced number of bits.

- ✓ The $\Sigma-\Delta$ modulator structures have several operational amplifiers and one comparator; whereas 10-bit ADC converters have 10244 comparators. This simplifies ADC structure, reduces the size, interconnection resources and power usage. 10-bit A/D converter e.g. Analog Devices AD9048, or Philips TDA8790 consumes 30 to several hundred milliwatts, whereas 1-bit $\Sigma - \Delta$ modulator consumes 20 milliwatts with an circuit area of 0.24 mm^2 [70].

- ✓ Conventional ADC's require analogue filters and high precision analogue circuits sensitive to noise. However, delta-sigma modulators have imprecise analogue circuits operating at high speed to achieve high SNR values.

- ✓ The traditional A/D converters are packaged individually in multichip modules, so interconnection with other circuitry requires space consuming. However, the $\Sigma - \Delta$ modulators can be integrated in large numbers on a chip. They can be manufactured in low cost very large scale integration. The delays are performed via CMOS FIFO's and the beam sum is done via standard adders across the array.

Despite these benefits, $\Sigma - \Delta$ beamformers have some trade-offs such as an elevated noise floor. The comparison of images generated by multi-bit ADC and single-bit $\Sigma - \Delta$ modulators are given in the following Figure 8.22:

Since the fixed transmit focus is chosen as 60 mm, the strongest reflector is the third wire. The elevated noise floor by $\Sigma - \Delta$ beamformer is a direct result of the dynamic focusing. The repeated samples in the dynamic focusing causes the demodulator filter to interpret an extra sample difference which actually does not exist. This disturbs the synchronization and increases the of noise floor. This noise level can be compared in terms of SNR values, which is calculated before logarithmic compression. The signal power is calculated within a small kernel over the wire and the noise power calculated within a larger kernel including the artefacts and reflectors [68]. The SNR value for

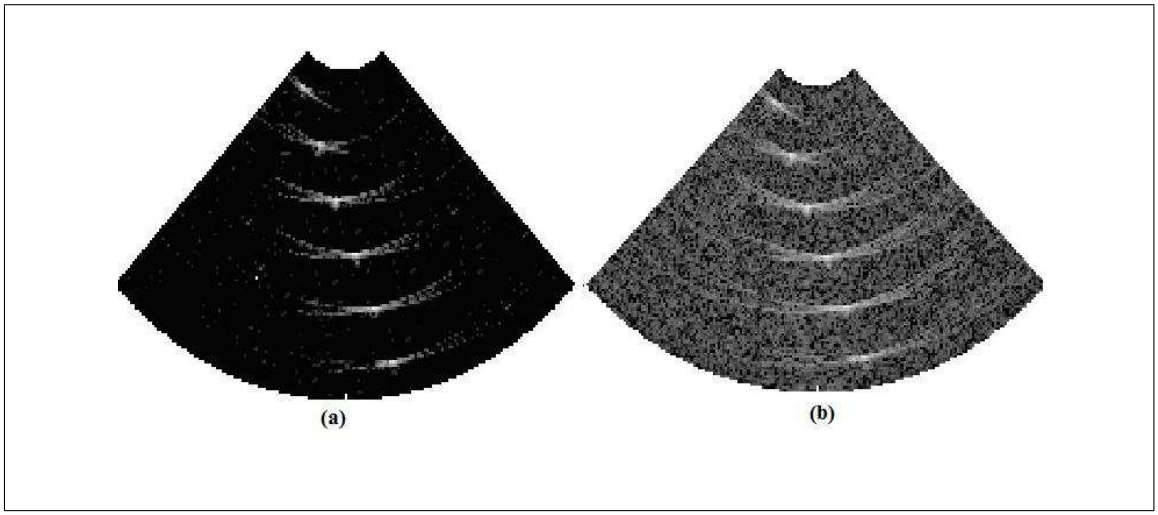

Figure 8.22 (a) 10-bit A/D beamformer (b) 1-bit $\Sigma - \Delta$ beamformer.

conventional beamformer is calculated as 60.1 dB, whereas this amount reduced to 41.8 dB. As a result an approximately 18 dB difference in SNR values is obtained. The reduced SNR value can be improved using several methods detailed in the literature. One method recodes the samples so that for each delay increment a null sample is inserted into the sample sequence [71], another method manipulates the samples by an analogue feedback gain within the $\Sigma - \Delta$ modulator. The repeated/omitted samples are manipulated by an analogue feedback magnitude within the $\Sigma - \Delta$ structure [69]. The third method uses non-uniform oversampling beamformer [68]. The typical sampling rate of traditional 10-bit A/D converters is not sufficient for delay accuracy to properly form a focus. Therefore, complicated processes such as sinc interpolation filters at each channel are required to increase the sampling rate up to 32 times the ultrasound carrier frequency. The inherently high sampling rate of $\Sigma - \Delta$ modulators secures the sufficient delay accuracy. As a result, the complicated interpolate circuitry of traditional beamformer are replaced by simple shift registers. Furthermore, most state-of-art ultrasound imaging systems have 128 to 256 channels beamformers that produce 2-D images. These arrays require anywhere 512 to $16,384$ parallel processing channels [69]. The major investigation in ultrasound imaging systems is to reduce this channel count. Therefore, simplifying the front-end hardware of the ultrasound system is the most important factor for economical scanners. In 1-bit sigma-delta converters, components with much less than the resolution of the overall converter components are

used instead of complicated and high resolution analogue components used by 10-bit A/D converters. Therefore, $\Sigma - \Delta$ modulators can be easily manufactured in switched capacitor circuits implemented in CMOS VLSI processes [70]. This means, modulators can be integrated onto the same chip as thedigital processing circuits. As a result; one can construct a beamformer-on-a-chip that takes inputs from an array of elements and outputs a digital beamformed sample stream. The multi bit resolution is achieved using single low-pass filter and decimation process acting on the outputs of this beamformer. Thus, complexity, size and power consumptions of traditional phased array front-end processing using 10-bit A/D beamformers can be dramatically reduced by using single bit $\Sigma - \Delta$ beamformers [68]. The simplicity of the $\Sigma - \Delta$ beamformers is suitable for low-power 3-D scanners with large channel count beamformers and portable and lightweight ultrasound scanners and intravascular imaging systems [70]. Despite these benefits, $\Sigma - \Delta$ beamformers produce significant image artefacts due to the disturb syschronization between the modulator and the demodulator because of the repeated samples in dynamic focusing, which can be improved by several methods detailed in the literature [68, 69, 71].

9. CONCLUSION

$\Sigma-\Delta$ modulators are based on oversampling and noise-shaping. Oversampling, i.e. using a sampling rate much larger than the Nyquist rate, causes the quantization noise to spread over the region much larger than the signal bandwidth. Noise-shaping pushes most of the noise components to out of the signal band via error-feedbacks and secures a significant attenuation of the quantization noise in the signal band. As discussed in this study, SNR values of sigma-delta modulators using the oversampling and noise-shaping techniques are much higher compared to the conventional Nyquist-rate converters. In addition to the basic principles and advantages of $\Sigma-\Delta$ converters, various design topologies for low-pass and band-pass $\Sigma-\Delta$ modulators are discussed. The design topologies were developed from the general form $Y(z) = X(z)STF(z) + E(z)NTF(z)$. The output of the modulator is the superposition of the input signal and the quantization noise shaped by the NTF. The gain of the NTF is close to zero in the signal band and close to unity outside the signal band, which causes the noise components in the signal band to attenuate significantly by leaving the input signal unchanged. For a class of LP $\Sigma-\Delta$ modulators, the NTF has zeros at dc, i.e. at $z = 1$. Thus, the NTF can be expressed in the form of $(1 - z^{-1})^N$ which behaves as a high-pass filter. This ensures large attenuation of the quantization noise at the lower frequencies [26]. The NTFs realized by the BP $\Sigma-\Delta$ modulators have zeros in the signal band around the normalized center frequency ν, thus making the NTF a band-stop filter and the loop-filter to have infinite gain in the signal band [34]. For this purpose, a low-pass-to-band-pass ($LP \rightarrow BP$) transformation is applied at the points $z = \pm e^{j2\pi\nu}$ to a suitable LP $\Sigma-\Delta$ modulator; so that from a LP $\Sigma-\Delta$ modulator of order n, a BP $\Sigma-\Delta$ modulator of order $2n$ is obtained. By moving the zeros from $z = 1$ to complex conjugates, the NTF yields $1 - (2\cos(2\pi\nu))z^{-1} + z^{-2}$ where ν refers to the normalized input frequency [14]. Since, high-order $\Sigma-\Delta$ modulators with single-loop structures suffer from stability problems, the cascaded (MASH) structure are widely used, which exploits the inherent stability of low-order $\Sigma-\Delta$ modulators. Alternatively, the single-loop $\Sigma-\Delta$ modulator topologies can be stabi-

lized by adding feedforward or feedback paths with appropriately weighted coefficients. Butterworth and Inverse Chebyshev filters can be used to compute the NTFs of higher-order $\Sigma - \Delta$ modulators. The lower and upper frequencies of the NTF are selected so as to ensure that the input signal is positioned at the centre of the signal bandwidth. According to the NTF design methodologies explained throughout the study, the proposed $\Sigma - \Delta$ modulator structures are already modeled using Simulink blocks. The MATLAB routines embedded in the GUI map the user-defined parameters into the building block specifications and display the simulation results in terms of SNR values, histograms and power spectral densities. The simulation results show that the SNR values are increasing with the increasing order of the $\Sigma - \Delta$ modulators. For a low-pass 1^{st} order single-loop $\Sigma - \Delta$ modulator for an OSR of 128, the SNR is seen to increase by 12 dB per modulator order. The simulation results prove that; as the order of the modulator increases, the system performance is improved. However, the results also show that there is a trade-off between high order structures and system stability. For higher orders, the over-loaded quantizer causes the system to become unstable. Since the single-loop structures of orders higher than two suffer from stability problems, multi-stage, structures are introduced. Although the system structure becomes more complicated, cascading of low-order modulators guarantees the system to be unconditionally stable. The SNR values of a 3^{rd} order $\Sigma - \Delta$ modulator with multi-loop (MASH) structure is approximately 10 dB higher than a 3^{rd} order modulator with single-loop structure. On the other hand, as discussed previously, the periodic components in the system like sinusoidal input signals cause tones. Therefore to make the quantization noise more random dither is added to the system. The simulation results show that, there is a trade-off between the tonality of the system and the SNR values. As the tonality in the signal-band is improved with increased dither amplitude, however the SNR values are decreased. Furthermore, Butterworth filters and Inverse Chebyshev filters are used to compute the NTFs of higher-order $\Sigma - \Delta$ modulators. The behavioral-level simulations using Simulink and MATLAB routines, proves the theoretical background and provides the performance analysis and trade-offs of the design topologies. As the major aim of the study, a software design, evaluation and measurement tool in a MATLAB environment in conjunction with Simulink is developed to speed up the design, analysis and evaluation at the system-level of various

easy-to-implement LP and BP $\Sigma-\Delta$ modulators. This tool is user-friendly as it allows designers and practitioners to perform detailed simulations very easily. The MATLAB routines embedded in the GUI map the user-defined parameters into the building block specifications and display the simulation results in terms of SNR values, histograms and power spectral densities. The MATLAB routines embedded with the GUI, call the corresponding Simulink models, assign the user-defined parameters to the model blocks, simulate the system and display the simulation results. This software tool facilitates the development and analysis of various $\Sigma-\Delta$ modulator design topologies by changing the system specifications without dealing directly with the Simulink models. As a direct biomedical implementation of the designed structures via software tool, ultrasound beamforming using a low pass 2^{nd} order $\Sigma-\Delta$ modulator is performed. The resulting image is compared with the images constructed using 10-bit A/D converters. The repeated/omitting samples during dynamic focusing degrade the image quality of $\Sigma-\Delta$ beamformers. Image correction methods can be used to improve the resolution. Although the elevated noise in the background, the simplicity, reduced cost and power are the most important benefits of $\Sigma-\Delta$ modulators for especially low-power 3-D scanners with large channel count beamformers and portable and lightweight ultrasound scanners and intravascular imaging systems.

APPENDIX A. LOOP FILTER TOPOLOGIES

The circuit topologies are based on the same universal relation between the system loop-filter $L(z)$ and the NTF have the relation such as;

$$NTF = \frac{1}{1 + L(z)}.$$

The corresponding loop-filters for different modulator structures can be designed using Butterworth and Inverse Chebyshev Filter approximations.

A.1 Weighted Feedforward Structure

The design topology consists of cascaded integrators with the transfer functions $H(z) = z^{-1}/1 - z^{-1}$, whose outputs are weighted and summed up to form the overall loop-filter transfer function, $L(z)$. The linear system analysis gives the transfer function of the loop-filter, $L(z)$ as given in Eq. 5.14. Since all the poles of $L(z)$ are at $z = 1$ a Butterworth high-pass filter can be used to obtain adequate coefficients that make the system stable.

Such filters are easily obtained using standard filter design packages using MATLAB command such as;

$$[A, B] = butter(N, R_s, f_b, 'high'),$$

which produces N^{th} order high-pass Butterworth Filter with a cut-off frequency of f_b (relative to half the sampling rate) and stop-band attenuation of R_s (in dB). The numerator polynomial A has to be scaled such that the first element $A(1)$ is unity. The NTF can be find using the coefficients obtained from the Butterworth filter response such as;

$$NTF(z) = \frac{A(z)}{B(z)}.$$

Once the NTF is obtained, the corresponding $L(z)$ can be computed from the relationship that;

$$L(z) = \frac{B(z) - A(z)}{A(z)}. \tag{A.1}$$

To solve for the desired feedforward coefficients; Butterworth $L(z)$ (Eq. A.1) and system $L(z)$ (Eq. 5.14) are equated.

A.2 Weighted Feedforward Summation with Local Feedbacks

For relatively large signals, the zeros of the NTF do not need to be at a certain frequency. Therefore, adding a small negative feedbacks around pairs of integrators cause the zeros of the loop filter shifted away from $z = 1$ (Figure 5.9). The loop transfer function can be obtained as given in Eq. 5.15. In order to solve the desired coefficients complex zeros besides the real zeros are needed. Thus, one should use inverse Chebyshev Filters instead of Butterworth Filters.

$$[A, B] = cheby2(N, R_s, f_b, 'high'),$$

which produces N^{th} order high-pass Inverse Chebyshev Filter with a cut-off frequency of f_b and stop-band attenuation of R_s. The numerator polynomial A has to be scaled to ensure that the first element $A(1)$ is unity. Similar to Butterworth Filter's NTF, the loop-filter transfer function $L(z)$ can be obtained from Eq. A.1. Again by equating the $L(z)$ obtained from system analysis given in Eq. 5.15 and Chebyshev's $L(z)$ given in Eq. A.1, the desired coefficients can be calculated.

REFERENCES

1. Inerfield, M., G. R. Lockwood, and S. Garverick, "A sigma-delta based sparse synthetic aperture beamformer for real-time 3-d ultrasound," *Transcastions on Ultrasonics Ferroelectrics and Frequency Control*, Vol. 49, Feb 2002.

2. Norman, O., "A bandpass delta-sigma modulator for ultrasound imaging at 160mhz clock rate," *IEEE Journal of Solid-State Circuits*, Vol. 31, pp. 2036–2041, Dec 1996.

3. Karaman, M., and M. Kozak, "Digital beamforming using nonuniform oversampling delta-sigma conversion," *Proc. IEEE Ultrason. Symp*, Vol. 2, pp. 1279–1282, Oct 1999.

4. Candy, J. C., and G. Temes, *Oversampling methods for A/D and D/A conversion oversampling delta-sigma data converters*, New York: IEEE Press, 1992.

5. Tommazaou, C., N. Battersby, and S. Porta, "Circuits and systems tutorials," *IEEE Proc.ISCAS*, pp. 195–260, May 1994.

6. Hauser, M. W., "Principles of oversampling a/d conversion," *Journal Audio Engineering Society*, Vol. 39, pp. 3–26, Feb 1991.

7. Bryant, J. M., "Bandpass sigma-delta adcs for direct if conversion," *Analog Devices*, 1994.

8. Jayaraman, A., P. Asbeck, K. Nary, S. Beccue, and K. Wang, "Bandpass delta sigma modulator with 800 mhz center frequency," *Gallium Arsenide Integrated Cicuit Symposium Technical Digest*, pp. 95–98, 1997.

9. Gourgue, F., and M. Bellanger, "A bandpass subsampled delta-sigma modulator for narrowband cellular mobile communications," *IEEE Proc. ISCAS*, Vol. 5, pp. 353–356, May 1994.

10. Bazarjani, S., and M. Snelgrove, "A 4th order sc bandpass sigma delta modulator designed on a digital cmos process," *38th Midwest Symposium on Circuits and systems*, Vol. 2, pp. 1345–1348, Aug 1995.

11. Chuang, S., X. Yu, T. Sculley, and R. Bamberger, "Design and implementation of a sixth-order bandpass delta-sigma a/d converter with single quantiser," *IEEE Proc. ISCAS*, pp. 381–384, Jun 1997.

12. Kim, S., S. Joeres, N. Zimmermann, M. Robens, R. Wunderlich, and S. Heinen, "Continuous-time quadrature bandpass sigma-delta modulator for gps galilelo low-if receiver," *IEEE International Workhop on Radio Frequency Integration Technology*, Dec 2007.

13. Saputra, N., M. Pertijis, K. Makinwa, and J. Hujising, "Sigma delta adc with a dynamic reference for accurate temperature and voltage sensing," *IEEE International Symposium on Circuits and Systems*, 2008.

14. Norsworthy, S. R., R. Scheier, and G. C. Temes, *Delta-Sigma Data Converters*, New York: IEEE Press, 1997.

15. Boser, B. E., and B. A. Wooley, "The design of sigma-delta modulation analog-to-digital converters," *IEEE Journal of Solid-state circuits*, Vol. 23, Dec 1988.

16. Amaya, J. M., F. Medeiro, F. V. Fernandez, R. Rio, and A. Rodriguez-Vazquez, "Matlab simulink-based high-level sysnthesis of discrete-time and continuous-time modulators," *IEEE Computer society*, 2004.

17. Kuo, T., K. Chen, and J. Chen, "Automatic coefficients design for high-order sigma-delta modulators," *Trans. on Circuits and Systems-II Analog and Digital Signal Proc.*, Vol. 46, Jan 1999.

18. Medeiro, F., B. Perez-Verdu, and A. Rodriguez-Vazquez, *Top-down design of high-performance modulators*, Netherlands: Kluwer Academic Publishers, 1999.

19. Francken, K., P. Vancorenland, and G. Gielen, "Daisy a simulation-based high-level synthesis tool for modulators," *Proc. IEEE Int. Conf. Computer-Aided Design*, pp. 188–192, 2000.

20. Jantzi, S., C. Ouslis, and A. Sedra, "Transfer function design for converters," *IEEE Proc. ISCAS*, pp. 433–436, 1994.

21. Proakis, J. G., and D. G. Manolakis, *Digital signal processing*, Pearson Prentice Hall, 1996.

22. Oppenheim, A., and R. Schafer, *Discrete time signal processing*, Prentice-Hall, 1989.

23. Park, S., *Principles of sigma-delta modulation for analog-to-digital converters*, Motorola Digital Signal Processors, 2008.

24. Bennett, W., "Spectra of quantized signals," *Bell System Technical Journal*, pp. 446–472, Jul 1948.

25. Ziemer, R. E., W. H. Tranter, and D. R. Fannin, *Signals and systems continuous and discrete*, United states of America: Prentice Hall Press, 1998.

26. Aziz, P. M., H. V. Sorensen, and J. Spiegel, "An overview of sigma-delta converters," *IEEE Signal Processing Magazine*, Vol. 13, Jan 1996.

27. Candy, J. C., and O. J. Benjamin, "The structure of quantization noise from sigma-delta modulation," *IEEE Transactions on Communications*, Vol. 29, Sep 1981.

28. Candy, J. C., "Decimation for sigma delta modulation," *IEEE Transactions on Communications*, Vol. 34, pp. 72–76, Jan 1986.

29. Candy, J. C., "A use of double integration in sigma-delta modulation," *IEEE Transactions on Communications*, Vol. 33, pp. 249–258, Mar 1985.

30. Schreier, R., and G. C. Temes, *Understanding delta-sigma data converters*, IEEE Press-Wiley-Interscience Publication, 1997. Available: http:/www.atm.com.

31. Thomas, B., and M. D. Weir, *Thomas Calculus, 11th edition*, Pearson Addison-Wesley, 2005.

32. Maloberti, F., *Data converters*, Netherland: Springer, 2007.

33. Friedman, V., "The structure of the limit cycles in sigma-delta modulation," *IEEE Transactions on Communications*, Vol. 36, pp. 972–979, Aug 1988.

34. Kozak, M., and I. Kale, *Oversampled delta-sigma modulators analysis applications and novel topologies*, Boston: Kluwer Academic Publishers, 2003.

35. Norsworthy, S. R., "Effective dithering of sigma-delta modulators," *IEEE Int. Symp. Circuit and Svstems*, Vol. 3, pp. 1304–1307, May 1992.

36. Kale, I., "Sigma-delta modulation and polyphase filtering-the key to high-fidelity data conversion and instrumentation," *IMEKO TC4 Workshop ADC Modelling*, pp. 183–192, May 1996.

37. Adams, R. W., P. F. Ferguson, A. Ganesan, S. Vincelette, and R. Libert, "Theory and practical implementation of a fifth-order sigma-delta a/d converter," *J. Audio eng. Soc*, Vol. 39, pp. 515–528, Jul 1991.

38. Ritoniemi, T., T. Karema, and H. Tenhunen, "Design of stable higher order i-bit sigma-delta modulators," *IEEE Int. Symp. Circuit and Systems*, pp. 3267–3270, May 1990.

39. Eynde, F., G. Yin, and W. Sansen, "A cmos fourth-order 14b 500k-samples/s sigma-delta adc converter," *Digest of Technical Papers International Solid State Circuits Conference*, pp. 62–63, 1991.

40. Chao, K., S. Nadeem, W. Lee, and C. Sodini, "A higher order topology for interpolative modulators for oversampling a/d converters," *IEEE Transactions on Circuits and Systems*, pp. 309–318, Mar 1990.

41. Hein, S., and A. Zakhor, "On the stability of sigma delta modulators," *IEEE Trans. Int. Symp. Circuits Sys.*, Vol. 2, pp. 2322–2348, Jul 1993.

42. Leung, B., and S. Sutarja, "Multibit sigma-delta a/d converter incorporating a novel class of dynamic element matching techniques," *IEEE Transactions on Circuits and Systems II*, Vol. 39, pp. 35–51, Jan 1992.

43. Ardalan, S. H., and J. Paulos, "Analysis of nonlinear behaviour in delta-sigma modulators," *IEEE Trans. Circuits Sys.*, Vol. 34, pp. 593–603, Jun 1987.

44. Wang, H., "On the stability of third-order sigma-delta modulation," *Proc.IEEE Int. Symp. Circuits Sys.*, Vol. 2, pp. 1377–1380, May 1993.

45. Adams, R., "Design aspects of high-order delta-sigma a/d converters," *IEEE Intemational Symposium on Circuits and Systems Tutorials*, pp. 235–259, 1994.

46. Uchimura, K., T. Hayashi, T. Kimura, and A. Iwata, "Oversampling a-to-d and d-to-a converters with multistage noise shaping modulators," *IEEE Trans. Acorrst. Speech Signal Proc.*, Vol. 36, pp. 1889–1905, May 1988.

47. Gray, R., "Quantization noise spectra," *IEEE Transactions on Information Theory*, pp. 1220–1244, Nov 1990.

48. Yin, G., F. Stubbe, and W. Sansen, "A 164 320-khz cmos a/d converter using two-stage third-order sigma-delta noise shaping," *IEEE Journal of Solid State Circuits*, pp. 640–647, Jun 1993.

49. Williams, L., and B. Wooley, "Third-order sigma-delta modulator with extended dynamic range," *IEEE Journal of Solid State Circuits*, pp. 193–202, Mar 1994.

50. Snoeji, M. F., O. Bajdechi, and J. H. Huijising, "4th-order switched-capacitor sigma-delta a/d converter using a high-ripple chebyshev loop filter," *IEEE International Symposium on Circuits and Systems*, Vol. 1, pp. 615 –618, May 2001.

51. Ferguson, P. F., A. Ganesan, and R. W. Adams, "One bit higher order sigma-delta a/d converters," *IEEE Proc. ISCAS*, Vol. 2, pp. 890–893, May 1990.

52. Moussavi, S., and B. Leung, "High-order single-stage single-bit oversampling a/d converter stabilized with local feedback loops," *IEEE Transactions on Circuits and Systems II*, pp. 19–25, Jan 1994.

53. Welland, D. R., B. P. Signore, E. J. Swanson, T. Tanaka, and K. Takasuka, "A stereo 16-bit sigma-delta a/d converter for digital audio," *J. Audio Eng. Soc.*, Vol. 37, pp. 476–486, Jun 1989.

54. Ergelen, J. V., and R. V. Plassche, *Bandpass sigma delta modulators*, Boston: Kluwer Academic Publishers, 1999.

55. Schreier, R., and M. Snelgrove, "Bandpass sigma-delta modulation," *Electronics Letters*, pp. 1560–1561, Nov 1989.

56. Troster, G., and H. Drepler, "An interpolative bandpass converter on a 1.2 umbicmos analog/digital array," *IEEE Journal of Solid State Circuits*, Vol. 4, pp. 471–477, Apr 1993.

57. Zrilic, D. G., *Circuits and systems based on delta modulation linear nonlinear and mixed mode processing*, Berlin Heidelber: Springer-Verlag, 2005.

58. Paulos, J., G. Brauns, M. Steer, and S. Ardalan, "Improved signal-to-noise ratio using tri-level delta-sigma modulation," *IEEE Conference on CAS*, pp. 463–466, 1987.

59. Longo, L., and B. Horng, "A 15b 30 khz bandpass sigma-delta modulator," *IEEE Int. Solid-State Circuits Conf. Dig. Tech. Papers*, pp. 226–227, Feb 1993.

60. Jantzi, S. A., W. M. Snelgrove, and P. F. Ferguson, "A fourth-order bandpass sigma-delta modulator," *IEEE J. Solid-state Circuits*, Vol. 28, pp. 282–291, Mar 1993.

61. Ribner, D. B., "Multistage bandpass delta sigma modulators," *IEEE Transactions on Circuits and Systems II Analog and Digital Signal Processing*, Vol. 41, pp. 402–405, Jun 1994.

62. Jantzi, S., R. Schreier, and M. Snelgrove, "Bandpass sigma-delta analog-to-digital conversion," *IEEE Transactions On Circuits and Systems*, pp. 1406–1409, Nov 1991.

63. Al-Janabi, M., *Design analysis and evalution of bandpass sigma-delta modulation.* PhD thesis, University of Westminster, London United Kingdom, 2000.

64. Stewart, R. W., and E. Pfann, "Oversampling and sigma-delta strategies for data conversion," *Communication Engineering Journal*, Feb 1998.

65. Schafer, M. E., and P. A. Lewin, "The influence of front-end hardware on digital ultrasonic imaging," *IEEE Transactions on Sonics and Ultrasonics*, Vol. 31, Jul 1984.

66. Havlice, J. F., "Medical ultrasound imaging an overview of principles and instrumentation," *Proceedings of the IEEE*, Vol. 67, pp. 620–640, Apr 1979.

67. Mooney, M., and G. Wilson, "Linear array transducer with improved image quality for vascular ultrasonic imaging," *Hewlett-Packard*, Vol. 45, pp. 43–51, Aug 1994.

68. Kozak, M., and M. Karaman, "Digital phased array beamforming using single-bit delta-sigma conversion with non-uniform oversampling," *IEEE Transactions on Ultrasonics Ferroelectrics and Frequency Control*, Vol. 48, pp. 922–931, Jul 2001.

69. Freeman, R., M. A. Morin, R. C. Anderson, C. S. Desilets, and M. ODonell, "Delta-sigma oversampled ultrasound beamformer with dynamic delays," *IEEE Transactions on Ultrasonics Ferroelectrics and Frequency Control*, Vol. 46, pp. 320–332, Mar 1999.

70. Tov, B., M. Kozak, and E. G. Friedman, "A 250 mhz delta-sigma modulator for low cost ultrasound sonar beamforming applications," *IEEE Electronics Circuits and Systems ICECS*, pp. 113–116, Dec 2004.

71. Freeman, R., M. A. Morin, R. C. Anderson, C. S. Desilets, and M. ODonell, "An ultrasound beamformer using oversampling," *Proc. IEEE Ultrason. Symp.*, pp. 1687–1690, 1997.